高温超伝導体を用いた自由電子レーザ用アンジュレータの着磁解析に関する研究

Doctoral Thesis

Numerical Analysis of Magnetization Process of High-Tc Superconductor Undulator for Free Electron Laser

Yi Deri

Muroran Institute of Technology

March 2018

Contents

Chapter 1

Introduction

The X-ray Free Electron Laser (X-FEL) is exemplary of the next generation of synchrotron light sources, providing us with a high-intensity and coherent X-ray that can be applied to many advanced technological processes such as analyzing protein structures, enhancing biological Nano-machines, imaging high-speed phenomena, practicing cellular biology, creating extreme states, and so on [1]-[3]. However, the X-FEL is currently only available in a few big laboratories such as SPring-8 and LCLS because of the system's very large size [4]-[5]. It is therefore essential to develop a compact size machine that can be more widely used in its place.

In order to develop a smaller size X-FEL, the FEL undulator must be constructed using small size and high-intensity magnets, such as the High-Tc Superconductor (HTS) magnet. However, it is very difficult to adjust the positions of individual HTS magnets after they have reached a superconducting state inside a cryostat, and the fluctuation of the amplitude of the vertical sinusoidal magnetic field component needs to be suppressed within 1% for the FEL oscillation to occur [1]. Therefore, numerical simulations of the magnetization process of the HTS play a very important role in determining suitable magnet sizes and alignments in the machine design process.

We have been developing a numerical simulation code for the magnetization process of the HTS undulator, which combines the current vector potential method (T-method) [6]-[10] with the Bean's critical state model and the power-law macro-model [11]-[14]

for the shielding current in the HTS. We can confirm the existence of a sufficient agreement between the simulation results and the distribution of magnetic field measurements for three Pure-type HTS undulator magnets [15]-[16].

As aforementioned, the X-FEL machine is a very large system that consists of more than two hundred magnets [5], and therefore a much larger scale simulation is required for the practical application of our developed code to the real X-FEL. We created a modified simulation scheme, which reduced the requisite calculation memory and the calculation time of the HTS magnetization process within the large scale simulation of the pure-type HTS undulator [17]-[18].

Chapter 2

Free-electron Laser (FEL)

In this Chapter, we will briefly introduce the history of radiation as a light source (as shown in Table 2.1.1) and some of its applications. Then, we will give an overview of free-electron lasers (FEL).

2.1 History of Synchrotron Radiation Light Sources

Synchrotron radiation (SR), as shown in Fig. 2.1.1, is the name given to the electromagnetic radiation (EMR or EM radiation) emitted from electrons moving along circular or undulating orbits and traveling with a velocity almost equal to that of light. This radiation is emitted tangentially to the direction of motion and can occur either in continuum or in quasi-monochromatic spectral forms. After the synchrotron was discovered by Frank Elder, Anatole Gurewitsch, Robert Langmuir and Herb Pollock in May, 1947 [19], it began being widely used around the world and was recognized as being

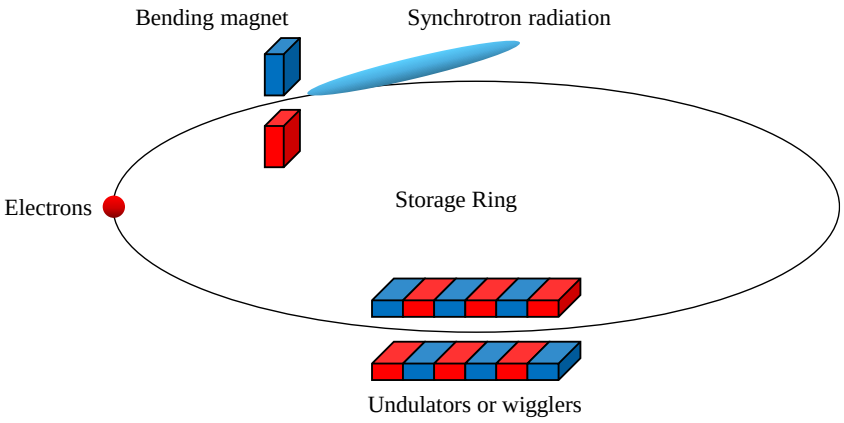

Fig. 2.1.1 Overview of synchrotron radiation.

one of the most brilliant sources of radiation between the infrared and the soft and hard x-ray regions. Synchrotron radiation offers exceptional brightness while covering a very wide photon energy and wavelength region, with particular strengths in the soft and hard X-ray regions where there are few alternative bright continuum light sources. Synchrotron radiation has been used extensively to determine the physico-chemical characteristics of many materials from atomic and molecular viewpoints and it can be readily applied to studies ranging from electronic structure analyses and simple crystal structure studies to protein crystallography, trace element mapping, high resolution microscopy and many more. It is also ideal for the investigation of the microscopic characteristics of materials that have been newly synthesized or extracted. Therefore, synchrotron radiation has become an indispensable tool for structural studies within the materials sciences and the life sciences, and today there are more than 60 synchrotron radiation sources globally that are in use or under construction [20].

The type of light that is most familiar to all human life is visible light (wavelengths from 400 to 700 nm; photon energies from 2eV to 3eV). However, invisible light that exists across the entire electromagnetic spectrum has become exceedingly important to daily use, such as light in the ultraviolet region (wavelengths about 200 to 400 nm; photon energies from 3eV to 6eV), the vacuum ultraviolet (VUV) and soft X-ray regions (wavelengths from 0.4 to 200 nm; photon energies from 6eV to 3keV), and finally the hard X-ray region (wavelengths from 0.01nm to 0.4 nm; photon energies from 3 keV to 100keV).

When electrons were discovered in 1897 by J. J. Thomson [21], the consensus was that no object was smaller than an atom, and that every atom had a structure. In the following year, it was found that charged particles, such as electrons, could generate

electromagnetic waves when moving circularly or oscillating. Finally, in 1946, the existence of these electromagnetic waves was confirmed by the existence of radiative losses in the energy of an electron on the magnetic field of an accelerator, in an experiment conducted by J. P. Blewett using a 100MeV betatron (GE: General Electric Company, in USA) [22]. In 1947, synchrotron radiation was first observed in the USA using GE's 70MeV synchrotron [23]. After its discovery, it was named synchrotron radiation (SR) or synchrotron light, with the most common Japanese nomenclature being synchrotron radiation. Around 1947, synchrotron radiation was regarded as an energy loss for accelerators in elementary particle experiments.

The following decades saw a series of trailblazing developments in the use of X-rays. In the 1950s, the theory of characteristics of light proposed by Schwinger and colleagues was demonstrated using the electron synchrotron in high-energy physics studies. Radiations in the wavelength region, from extreme ultraviolet to X-ray, were found to be remarkably stronger than the light emitted by existing light sources, so scientists seriously considered spectroscopic experiments on atoms and molecules to evaluate their use. After that, researchers working on physical properties noticed the usability of a very powerful and stable X-ray diffraction (XRD) light source, and the NBS in the USA developed the first full-scale spectroscopic experiment with vacuum-ultraviolet light in 1963. Then, synchrotron radiation experiments were conducted for the first time by parasitizing the accelerator for high-energy physics studies around 1965. However, in these early experiments, synchrotron radiation was just a "parasitic experiment" in which light was temporarily used and thrown away from the accelerator, and the initial synchrotron radiation experiments were restricted to the vacuum-ultraviolet wavelength region. Synchrotron radiation in the shorter wavelength (X-ray region) could be obtained by

increasing the electron energy of the accelerator during the electron-positron collision experiment. In addition, more stable synchrotron radiation could be supplied using the electronic "storage rings", which supplies elementary particles to high energy accelerators. The manifold experimental uses of synchrotron radiation that have been widely recognized by scientists.

Since the late 1960s, many important results were discovered in experiments using synchrotron radiation from electronic storage rings (mostly electron-positron collision beam rings in elementary particle experiments). The first storage-ring device was a 240 MeV storage ring in the University of Wisconsin System [24], after that, a GeV class storage ring called the Stanford Positron Electron Accelerating Ring (SPEAR) machine was built by Stanford Synchrotron Radiation Lightsource (SLAC). The latter's wavelength of light reaches the hard X-ray region (several dozens of KeV), within which an increasing number of researchers across fields have increasingly worked.

The first synchrotron radiation ring in the world, which is called SOR-RING, was built in Japan in 1975 [25]. From 1976 onward, the INS-ES [26] (Institute of Nuclear Study in the University of Tokyo) within INS-SOR (The Institute for Solid State Physics of the University of Tokyo) experimented with synchrotron radiation, and in 1980, KEK-PF began operating [27]. The second-generation radiation light source mainly uses radiation emitted from bending electromagnets for the exclusive use of such emitted light.

In early synchrotron radiation facilities, the synchrotron radiation generated by bending electromagnets that make up the accelerator ring was used exclusively, then, on the straight part of the storage ring, a light source was inserted as a device that deflects the beam to meander, and the generated synchrotron radiation could be used. The third-generation radiation light source is made up by a large number of insertion light sources

that can be arranged (such as undulators), and that could generate a very coherent emission. Since the 1980s, third-generation radiation light sources have been produced worldwide, and then the construction of “third generation” light sources incorporating “undulators” began from the 1990s because of the extremely high brightness that these could achieve. One of the reasons that such technology is made possible is the development of a powerful magnet (such as a neodymium magnet), which makes it possible to stably add a strong magnetic field to radiation light sources. In 1993, Advanced Light Source (ALS) in the United States focused on synchrotron radiation in the soft X-ray region [28], furthermore, large facilities that generated synchrotron radiation in the hard x-ray region were constructed in Europe, the United States and Japan. For example, European Synchrotron Radiation Facility (ESRF, in France) began operating in 1994 [29], the Advanced Photon Source (APS, in USA) began operating from 1996 [30], and the SPring-8 (in Japan) began operating in 1997 [31].

In recent years, to achieve much more powerful synchrotron radiation, the development of a new light source, the free-electron laser, used coherence in the insertion light source to oscillate the laser. Free-electron laser differ from ordinary lasers in that electrons are not attached to an atom or molecule and are free to respond to outside forces. FELs accelerate free electrons to relatively high energy levels by passing through the accelerator, and the electron beam generates monochromatic radiation by passing through an undulator. It is possible to change the wavelength by changing the characteristics of the electron beam energy, undulator, and brightness in order of magnitude stronger than synchrotron radiation. In free-electron lasers, the insertion light source is placed in the linear portion of the storage ring or behind the LINAC (Linear Accelerator), in addition, there are several methods of oscillation, such as inserting a laser from the outside or

amplifying the noise as a seed. Furthermore, the next generation of synchrotron radiation light sources is expected to be used from the wavelength region of far-infrared rays to soft X-rays with high peak power and high efficiency, and oscillation can be achieved in the wavelength range where impossible with the ordinary lasers.

The first undulator was demonstrated by H. Motz's research group at Stanford University in 1952 [32]-[33], and the ubitron (the original FEL), was invented based on early X-band experiments in 1957 [34]. The principle of FELs was proposed by Prof. J. M. J. Madey in 1970, and, in 1977, a FEL oscillator was been operated above threshold at a wavelength of 3.4 μm by his group [35]. In Japan, the first oscillation in the TERAS Electro technical Laboratory was seen in the visible light region in 1991. After that, the oscillations observed in both the UVSOR Institute for Molecular Science and NIJI-IV Electro technical Laboratory (ETL) were successfully performed from visible to ultraviolet regions in storage rings [36]. This oscillation has since been successfully performed from far-infrared to visible regions, even in ultraviolet regions by the linear accelerators at the University of Tokyo and Osaka University. After that, Studies of FEL became gradually popular, and research in this area increasingly focused on shorter wavelengths and high magnetic field intensities.

Then, the X-ray FEL, which is called the fourth-generation synchrotron radiation light source, is next in line in the evolution of synchrotron radiation sources and advances in accelerator technology. One of its advantages include the spatial coherence of X-ray FEL, which is almost 100% as compared to conventional synchrotron radiation light sources. In addition, it is possible to open up new research areas to observe dynamic phenomena in femtoseconds. Furthermore, it also enables structural analysis of proteins by one molecule. One application of X-ray FELs, for instance, is the observation of structural

changes in crystalline states by exploiting the high spatial coherence of XFEL.

In the conventional FEL, resonance-reflecting mirrors are placed at both ends of the undulator, and the light reciprocates many times in the resonator to strengthen the interaction between electrons to oscillate light. In this way, to make it oscillate in the X-ray region, it is necessary to find a mirror that is capable of reflecting light in the X-ray region.

However, there is no such a mirror with reflectance that is high enough to reflect the light in the X-ray region. Self-amplified spontaneous emission (SASE) FEL have been proposed as a solution to this. The SASE process starts with an electron bunch being injected into an undulator at a velocity close to the speed of light and a uniform density distribution within the bunch. In the undulator, electrons are wiggled and emit light that is characteristic of the undulator strength but is restricted by a certain energy bandwidth. Emitted photons travel slightly faster than electrons and interact within each undulator period. Depending on their phase in relation to each other, electrons gain or lose energy, and faster electrons catch up to slower ones. [37]

Most of the X-ray FEL facilities currently under construction are based on this SASE FEL: SACLA in Japan (RIKEN), LCLS (LINAC Coherent Light Source) in the USA (SLAC National Accelerator Laboratory) and European XFEL in Europe. SACLA has been especially successful in oscillating an X-ray FEL at a wavelength of 0.12 nm in June 2011, and the operation service started in March 2012 [4].

The brightness has increased exponentially since the advent of synchrotron radiation; especially after the advent of XFEL, which is expected to increase brightness even more (Fig. 2.1.2) [38]. The characteristic of X-ray FEL is extremely bright light (100 billion times than SPring-8), extremely short radiation time (10 trillionths of a second, 1/1000 of

SPring-8), and high coherence. For example, SACLA (RIKEN, Japan), which began operating in 2012, has a very wide wavelength range of 0.63Å to 3Å, a very high brightness that is 10^8 times that of SPring-8, a period of 60Hz, and is also coherent light, with a pulse of several hundred femtoseconds [4]. Since XFEL has these characteristics, it plays a very important role in the provision of measurements and analytical methods to obtain structural information on atomic and electronic levels.

XFEL can lead to the development of new measurement and analysis techniques in order to see structures and phenomena that could not be seen with other methods until now, and then, aims to open up new possibilities in various scientific and technological fields. It can also help develop new measurement and analysis methods through the advent of synchrotron radiation, thus playing a very important role in nanotechnology and materials science. Therefore, it is expected to be applied to a lot of fields such as atomic molecules, material properties, life sciences, and other in the future.

Table 2.1.1 History of Synchrotron light source

History of Synchrotron light source	
1st generation light source	Synchrotron Radiation (particle accelerators)
2nd generation light source	Synchrotron Radiation (dedicated machine)
3rd generation light source	Insertion Devices (wigglers or undulator, *etc*.)
4th generation light source	**High coherent X-ray (SASE FEL)**

(1) Atoms and molecules

When atoms or clusters are hit by very high-density X-ray pulses, several phenomena may occur, such as Multi-molecular ionization, generation of multiply charged ions, multiple inner shell vacancies and the Coulomb explosion. It is then possible to track the

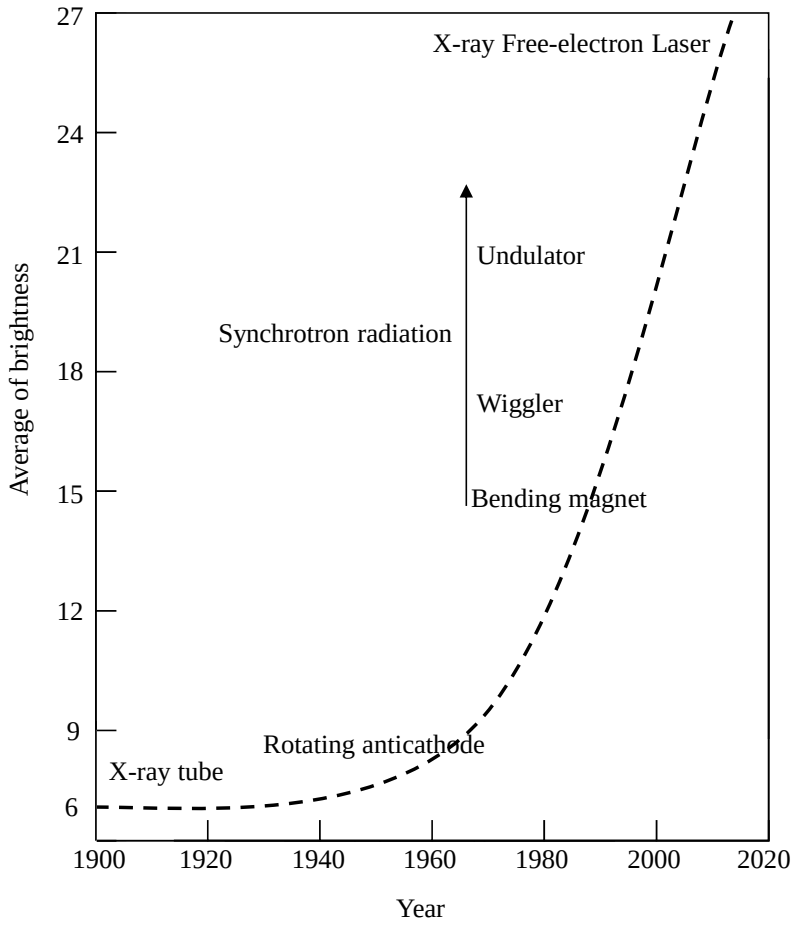

Fig. 2.1.2 History of development of synchrotron radiation brightness.

molecular structure and dynamics throughout chemical reactions with a time-resolved femtosecond by performing a pump-probe experiment with a visible laser. Femtosecond XFEL provides unique opportunities for the exploration of ultra-fast dynamics in atoms and molecules and for imaging structures and dynamics in biological systems, complex materials, and matter under extreme conditions. The response of individual atoms and molecules to intense, ultrashort X-ray pulses is essential to most FEL applications in these fields.

(2) Materials science

Since 100% coherence does not require long-period regularity in its sample, it can be

applied to the structural analysis of liquids, randomness systems, measurements of dynamic structural factors, and so on. For example, quantum materials present materials with promising functions, such as high-temperature superconductors and topological insulators, which have novel and unusual electronic properties and can revolutionize technology. XFEL permits the observation of ultrafast, photo-induced transitions of the atomic, charge, spin and orbital orders of quantum materials. Infrared FELs allow for non-linear excitations of these transitions with high spectral resolution.

(3) Life science

Even though the structural analysis of proteins has developed dramatically with the use of synchrotron radiation, two problems still arise. Firstly, it is impossible to create a single crystal even though it is small; secondly, the structure is not the same when the protein actually works in a single crystalline structure. Therefore, analysis of the structure of a single molecule has presented big challenges for many years.

After the FEL is realized, it is possible to analyze the structure using high coherence and the application of single particle structure analyses that combine phase recovery algorithms and over-sampling methods. In fact, researchers have successfully used this method to obtain the substance distribution of Escherichia coli with micro level resolution at the SPring-8 facility. In the future, it should be possible to analyze the structure at the atomic level by using the XFEL.

2.2 Overview of FEL

In order to explain the principle of the free-electron laser (FEL), we must explain how the structure of a FEL determines its functionality.

The overview of a free-electron laser is shown in Fig. 2.2.1. The free-electron laser is a kind of laser whose lasing medium consists of very-high-speed electrons moving freely through a magnetic structure (such as an undulator) [37]. As shown in Fig. 2.2.2, the free-electron laser is composed by three parts: an electron gun that generates electrons at a very high density and short pulse, an accelerator for accelerating the electrons, and an undulator that produces lasers from the electron beam [4].

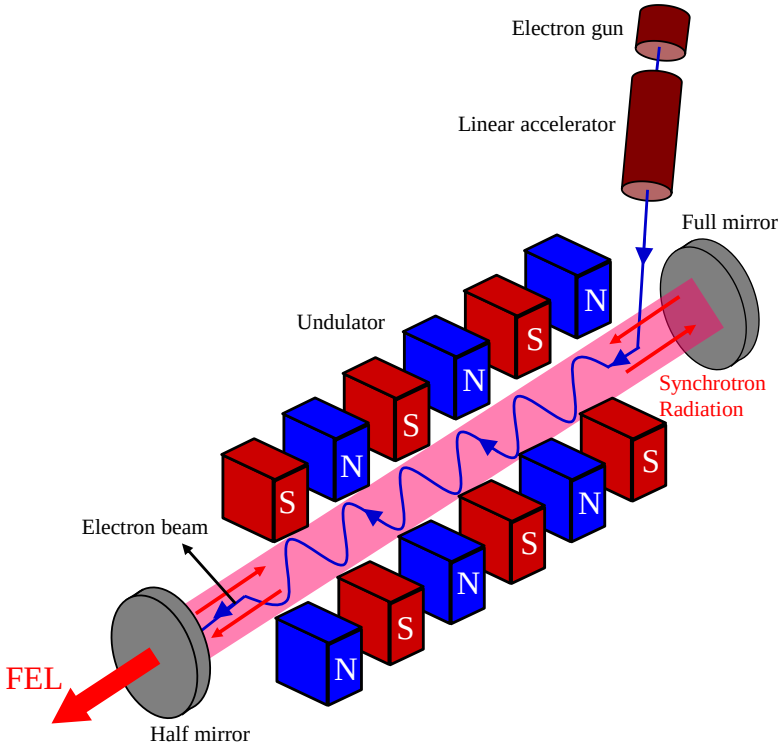

Fig. 2.2.1 Overview of free-electron laser.

(1) Electron gun

An electron gun (sometimes called electron emitter) is an electrical component in some

vacuum tubes that produces a narrow, collimated electron beam with a precise kinetic energy. Depending on their application, electron guns have varied shapes. However, beams are usually made by a cathode for electron emission, and by anodes and grids for acceleration and convergence, and a focusing electrode. In recent years, the electrode shape of the electron gun could be determined using a numerical simulation of the beam's trajectory as numerical simulation technology improves over time.

Next, we will briefly introduce the principle of the electron gun using thermionic guns, which are the most widely used. Fig. 2.2.2 shows the basic structure of a thermionic gun [39]. The electrons emitted from the cathode are accelerated to a predetermined energy using the high voltage applied to the anode, and the current is controlled by the voltage applied to the Wehnelt electrode. In addition, the crossover is formed by the lens action of the three electrodes—cathode, Wehnelt electrode and anode.

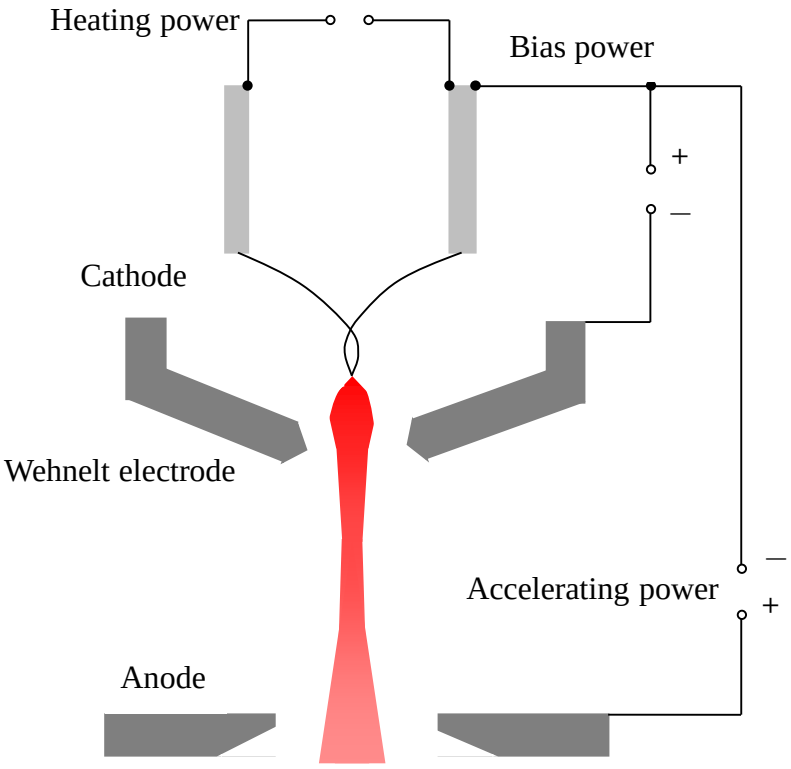

Fig. 2.2.2 Overview of a typical thermionic gun.

Aside from the thermionic gun, there are several other electron guns. For example, there exists a field emission gun in which a sharply pointed emitter is held at several kV negative potential relative to a nearby electrode, so that there is a sufficient potential gradient at the emitter surface to cause field electron emission. There is also a RF electron gun that generates and accelerates electrons simultaneously with a high electric field using microwave power. In the X-ray FEL of SACLA, the thermionic gun has been adopted because of stability and ease of maintenance.

The researchers were able to obtain a laser with high stability, high-frequency motion, high-electric-field reliability, and higher quantum efficiency, however, many of the scientists are still dedicated to developing a higher-quality and higher-performance electron gun.

(2) Accelerator

An accelerator (a particle accelerator) is a machine that uses electromagnetic fields to propel charged particles (ions or particles) to near-light speed. The structure of the simplest accelerator is shown in Fig. 2.2.3. The principle of the accelerator is that donut-shaped disks are arranged together, with additional voltage being applied between them by an external electrode. The negatively charged electrons are then attracted to the electrode and accelerated with kinetic energy. These accelerators are arranged into two basic classes: electrostatic accelerators and electromagnetic accelerators. Electrostatic accelerators use static electric fields to accelerate particles and an electromagnetic

accelerator use changing electromagnetic fields to accelerate particles [40].

In addition, there are two kinds of accelerators that rely on charged particle advancement: linear accelerators and circular accelerators.

A linear accelerator (LINAC) is a type of particle accelerator that greatly increases the kinetic energy of charged subatomic particles or ions by subjecting the charged particles to a series of oscillating electric potentials along a linear beamline.

In a circular accelerator, particles move in a circle until they reach sufficient energy. The particle track is typically bent into a circle using electromagnets. The advantage that circular accelerators have over LINAC is that the ring topology allows for continuous

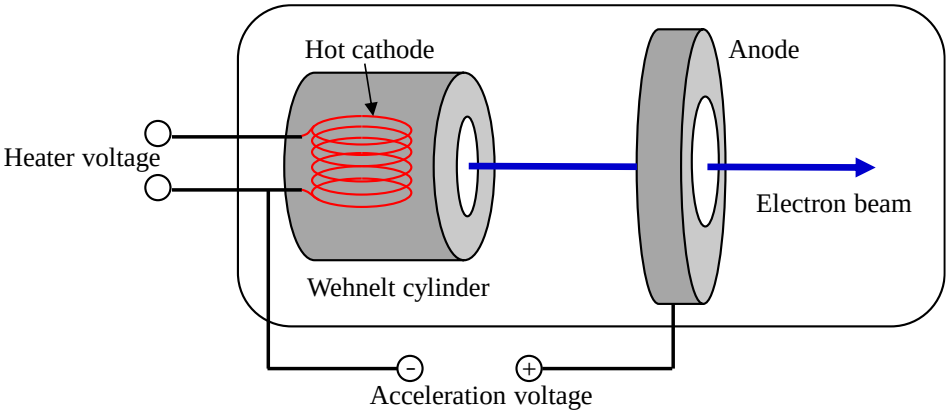

Fig. 2.2.3 Overview of a simplest accelerator.

acceleration because the particle can transit indefinitely. Another advantage is that a circular accelerator is smaller than a linear accelerator of comparable power, since LINAC would have to be extremely long to have the equivalent power of a circular accelerator. However, depending on the amount of energy, and the kind of particle being accelerated, circular accelerators suffer from a disadvantage in that the particles emit synchrotron radiation.

(3) Undulator

An undulator, which stems from high-energy physics, is an insertion device through

which an electron beam passes, and consists of a periodic structure of dipole magnets that meander while approaching light speed to generate synchrotron radiation (Fig. 2.2.4).

The wavelength of the radiation emitted from the FEL λ_R and the undulator strength parameter K can be expressed using the following equations:

$$\lambda_R[\text{Å}] = \frac{\lambda_u}{2\gamma^2}\left(1+\frac{K^2}{2}\right) = 13.056\frac{\lambda_u[\text{cm}]}{(E[\text{GeV}])^2}\left(1+\frac{K^2}{2}\right) \quad (2.2.1)$$

$$K = \frac{e\cdot B_0\cdot\lambda_u}{2\pi\cdot m_0 c} = 93.36 B_0[\text{T}]\cdot\lambda_u[\text{m}] \quad (2.2.2)$$

where γ is the Lorentz factor of the electron beam (electron energy), E is the energy of the electron beam, λ_u is the unit pitch of undulator magnet, e is the elementary charge ($e = 1.602176\times10\text{-}^{19}$), m_0 is the electron mass, c is the speed of light ($c = 299792458$m/s), and B_0 is the vertical component of the magnetic field on the electron trajectory. It is known that the FEL radiation field is incompatible with the frequency spread for $K >> 1$, however, it is coherent with the sharp spectrum for $K\approx1$. It is usually called an undulator for $K\approx1$, and a wiggler for $K >> 1$. Next generation FELs (XFELs) are classified into the latter case, for which $K\approx1$. In addition, Fig. 2.2.5 shows the trajectory of electrons and the energy distribution of synchrotron radiation relative to K. [41] It is effective to increase the energy of the electron beam (E) or reduce the spatial period of the undulator magnets (λ_u) to obtaining a short-wavelength radiation field (λ_R) from the equation (2.2.1). Accordingly, λ_u has to be smaller to obtain a higher frequency radiation field, as it is difficult to change the condition of electron energy. Since the value of K needs to be between 1 and 1.5 for a sharp spectrum and coherence, this implies that undulator magnets are required to be of smaller size (a smaller λ_u) and higher magnetic field intensity (a bigger B_0) than those of conventional FELs from the equation (2.2.2).

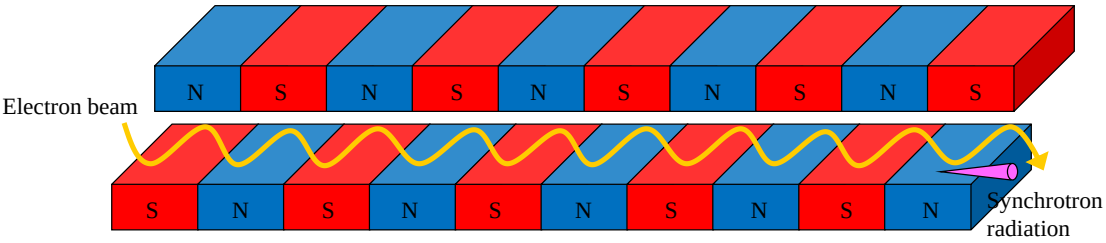

Fig. 2.2.4 Overview of an undulator.

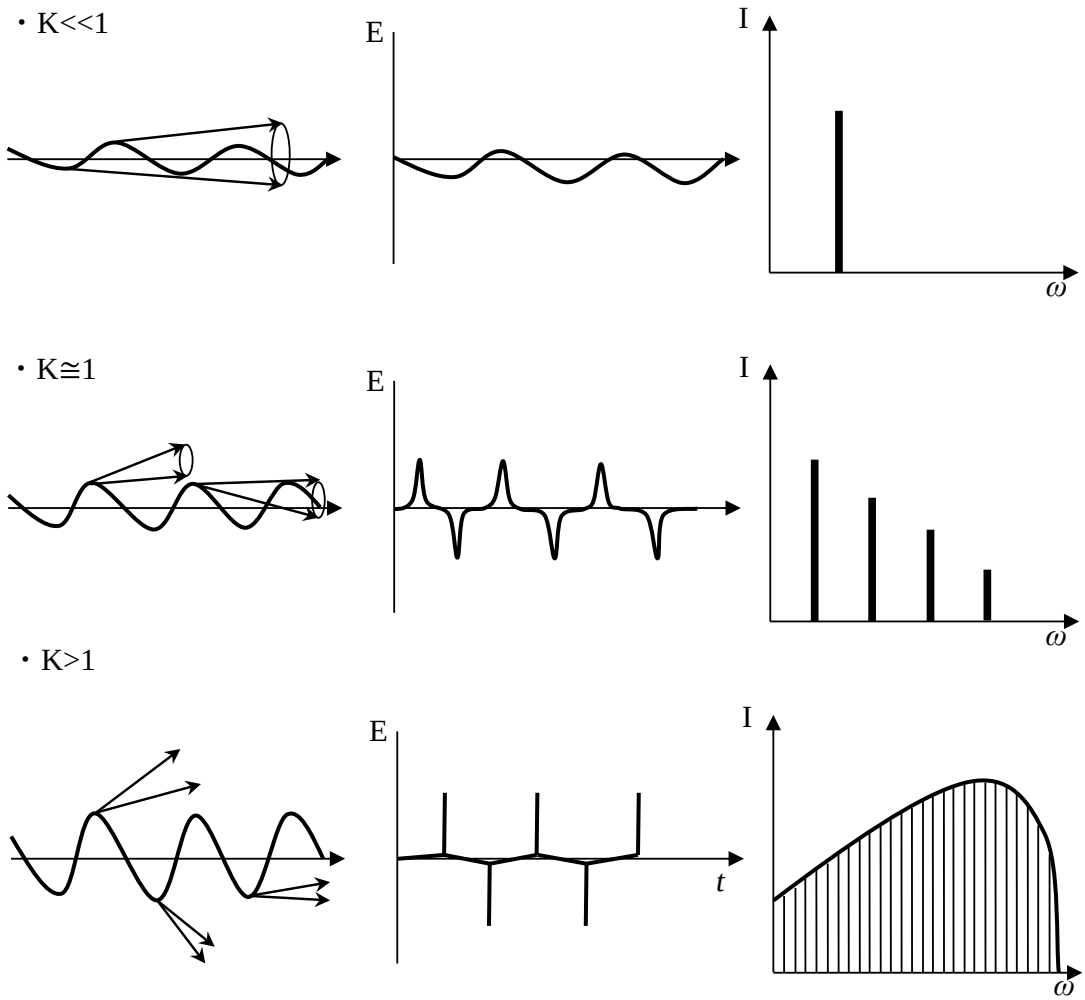

Electron trajectory | Temporal change of the electric field | Energy distribution of synchrotron radiation

Fig. 2.2.5 Energy distribution of synchrotron radiation by changing the strength of the magnetic field.

We would like to briefly explain the mechanism of generation of electromagnetic waves before explaining the principle of FEL. For single oscillating electrons, the

direction of the vectors of the interactions between the electric field and the magnetic field is always outward, as determined by electron motion. Therefore, the vibration energy spreads in concentric circles as electromagnetic waves. The vibrational motion of electrons is affected by the bremsstrahlung, and then the vibrational energy is reduced. The stimulated emission was a theoretical discovery put forth by A. Einstein in which, if an electron is accelerated by the external force, the moving particles will lose kinetic energy, the excess of which is converted into photons, thus satisfying the law of conservation of energy. The idea of a free-electron laser can also be explained by the above concept.

We will explain the stimulated emission using the interactions between the meandering electrons and the magnetic field.

It is assumed that the traveling direction of the meandering electrons is same as that of the monochromatic electromagnetic plane waves (as shown in Fig. 2.2.6) [42]. The maximum electric field intensity can be achieved so that the field of the electromagnetic wave is affected by the electric field vector of the electron A, when the speed of simple harmonic motion (electron A) is at a maximum (at point P) and its direction is opposite to the electric field E of the electromagnetic wave. However, the particles will lose some energy due to its bremsstrahlung. Then, the traveling speed of the electron A is slightly delayed compared to the electromagnetic wave, because the electron makes a meandering movement. For this reason, the simple harmonic motion of electron A lags behind the phase in the electric field of the electromagnetic wave. Although electron A gives energy to the electromagnetic waves, the energy decreases gradually as it travels. Then, the speed of simple harmonic motions becomes zero as they pass through point Q. At this moment, there are no interactions between the electric field vector and electromagnetic waves. In

other words, the electron A moves to the phase in one delayed electromagnetic wave. Then, the electromagnetic wave provides energy for the electron that is affected by the interactions between the electric field vector (the direction is opposite) and electric field of the electromagnetic wave. After a while, the periodic phase in simple harmonic motion is shifted by a half wavelength, the electric field vector of electron A reaches its maximum, and the interactions between the electromagnetic wave and the electric field also achieve their maximum. In other words, the strongest interactions can be obtained at every half wavelength, and an electron can provide enough energy for an electromagnetic wave or receive enough energy from an electromagnetic wave. Similarly, there is a state at which the electromagnetic wave that has received the amplification energy by electron A at point

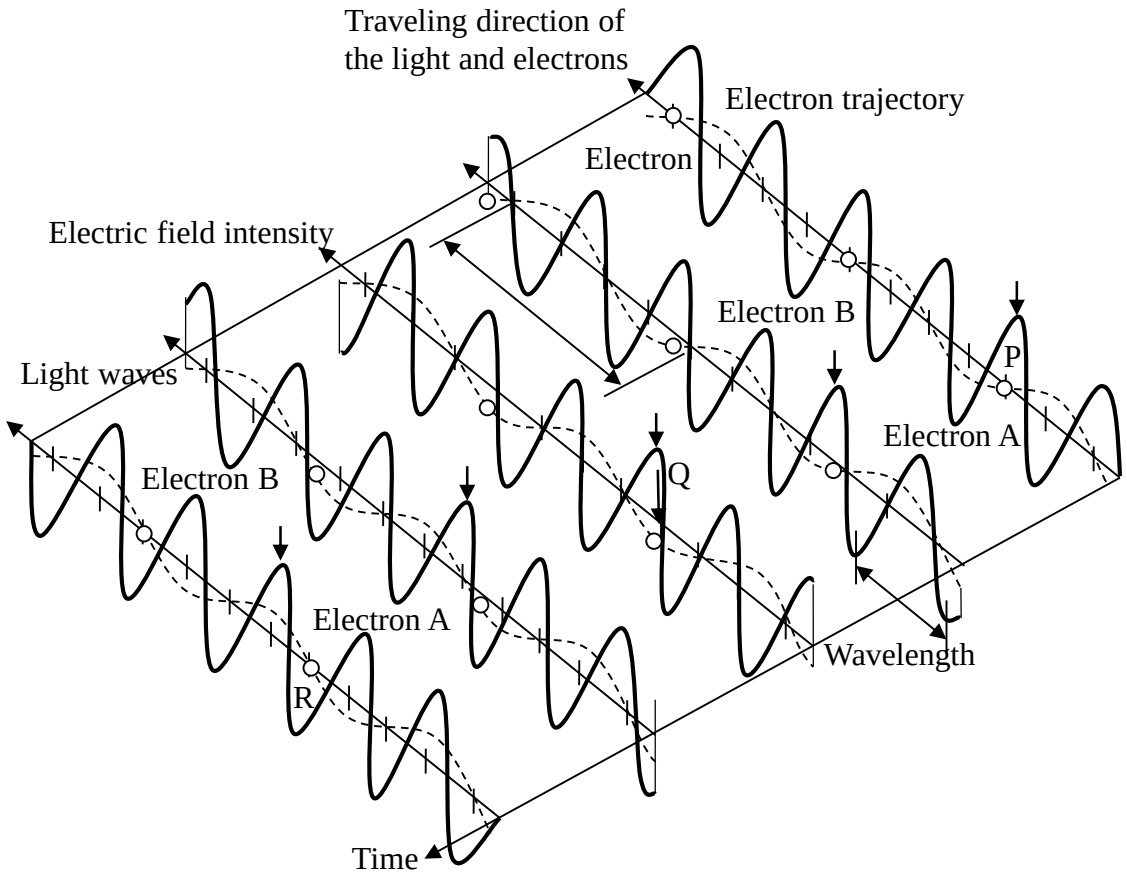

Fig. 2.2.6 Stimulated radiation of meandering electrons.

P catches the previous electron B at point R and receives energy at R. The electromagnetic wave is amplified twice by electrons.

This is the optical amplification based on the periodic motion of electrons and the Doppler effect of the electromagnetic wave in the interaction region. The condition for obtaining the strong interaction at every half period is that the half wavelength of light must be delayed at the half period of the meandering electron A. Therefore, it is determined by the external force (magnetic field intensity B_0 and the unit pitch of undulator's magnet) which causes the meandering movement of electron A, which is shown in equation (2.2.1) and equation (2.2.2). The undulator (equation (2.2.2)) is most frequently used as an external force, as the light amplified by the undulator is confined within the optical cavity to create hundreds of resonance interactions with the electron beam. Then, a high-power laser can achieve oscillation. This is the basic principle of FEL.

In a conventional free-electron laser, as shown in Fig. 2.2.7, the light reciprocates many times in the resonator to strengthen the interaction between electrons. However, the optical resonator cannot be used for X-ray FEL, since there is no mirror with high-enough reflectivity that can reflect X-rays. To solve this problem, a self-amplified spontaneous emission (SASE) is used for the free-electron laser in the X-ray region (Fig. 2.2.8). Contrarily to conventional free-electron lasers, the self-amplified spontaneous emission free-electron laser (SASE FEL) can generate a coherent light when the electrons are arranged at wavelength intervals by the interaction between the radiation from the back electrons and the previous electrons through a very long undulator. Nowadays, almost all X-ray FELs that are under construction or in the planning stages across the world, are based on the process of SASE.

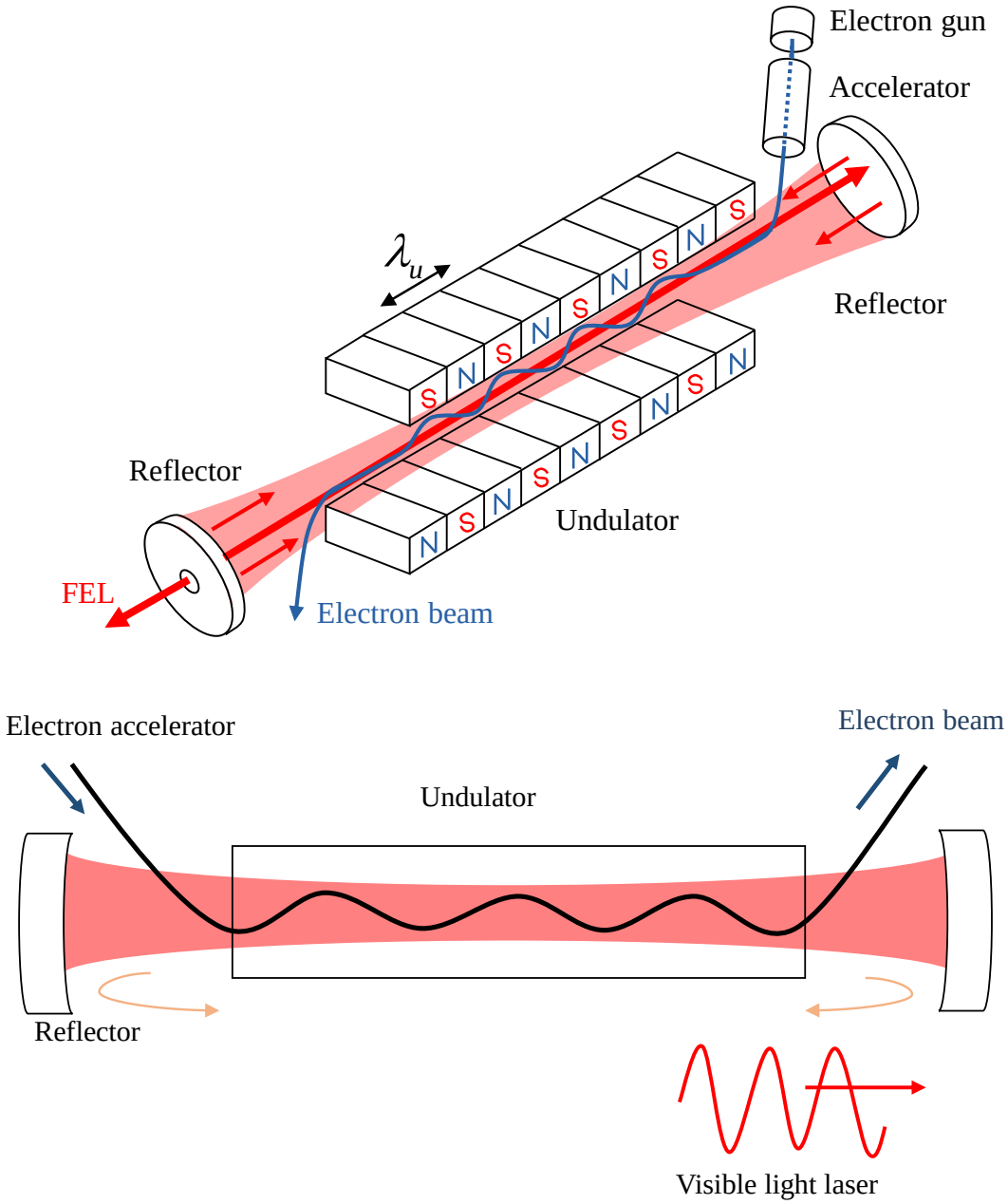

Fig. 2.2.7 Overview of a conventional free-electron laser.

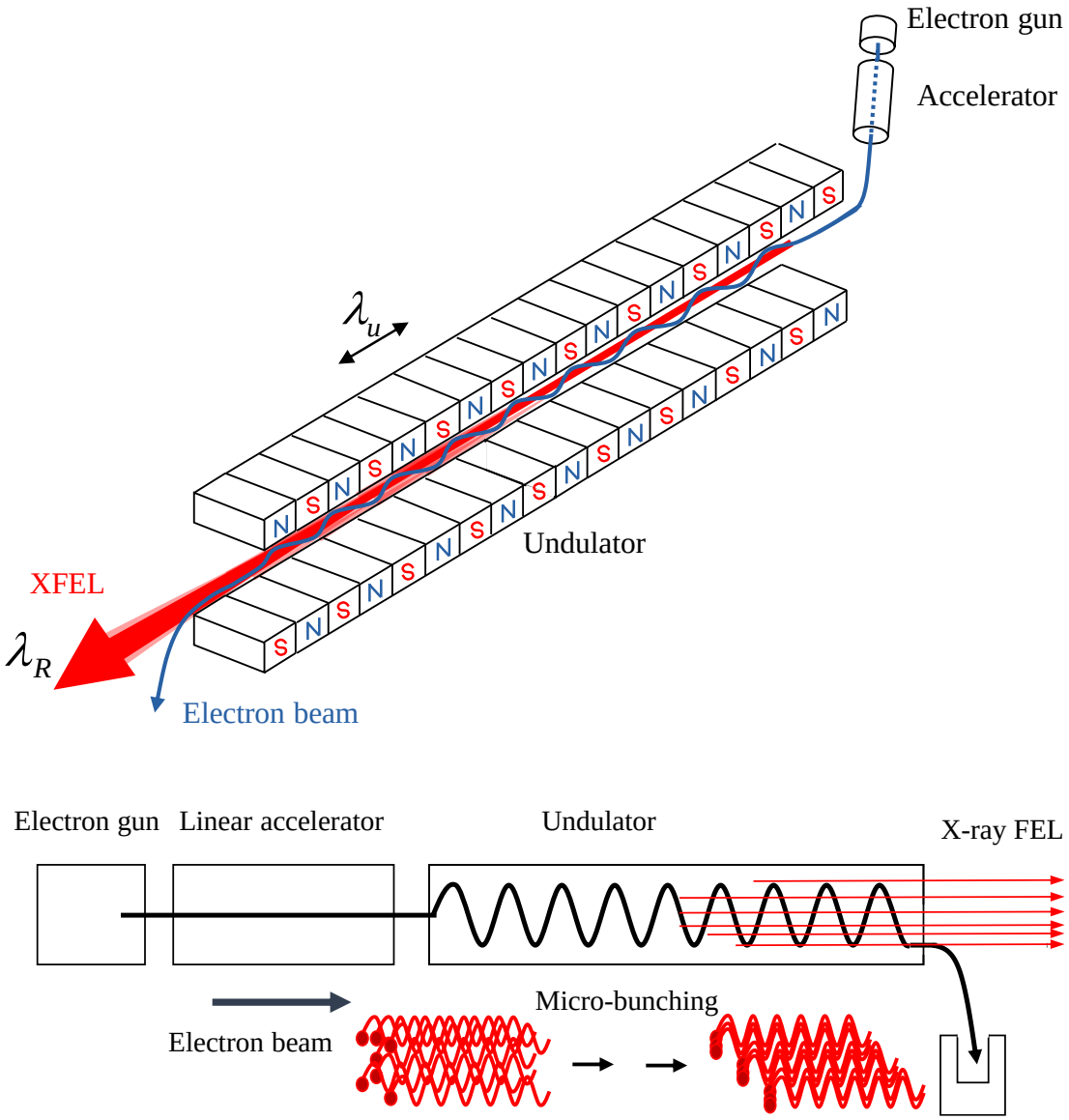

Fig. 2.2.8 Overview of a SASE free-electron laser.

Fig. 2.2.8 shows a diagram of a kind of X-FELs (SASE free-electron laser), from Chapter 2.1, that helps us understand that X-FEL can be used in many fields. However, it is currently only available in a few big laboratories such as SPring-8 in Japan, LCLS in USA, EuroFEL and SwissFEL in Europe, since it is a very large and expensive system. To downsize the X-FEL and achieve a shorter wavelength laser oscillation, it is necessary to reduce the period of the undulator λ_u or increase the electron beam energy E in equation (2.2.1). Since it is very difficult to flexibly change the energy E because it is determined by the specification of this upstream accelerator, it is essential to reduce the period of the undulator λ_u for a short wavelength FEL. On the other hand, it is also known that the parameter K should be equal to approximately 1 in equation (2.2.2) to achieve a coherent monochromatic light emission. Then, it's necessary to achieve a very high intensity magnetic field undulator (increase the B_0) for a short wavelength laser light and small size FEL. For this propose, it is recommended to use bulk high-Tc superconductivity magnets (bulk HTS magnets) to create high intensity HTS undulators.

2.3 HTS Undulators

The last part of Chapter 2.2 discussed the necessity of bulk HTS magnets for downsizing the X-FEL. In this chapter, we will introduce two examples of bulk HTS magnets: staggered array undulators (SAU) and pure-type HTS undulators.

2.3.1 Staggered Array Undulator (SAU)

(1) Structure

Fig. 2.3.1 presents the overall structure of the high critical temperature superconducting staggered array undulator (Bulk HTSC SAU) [1]. A basic version of SAU (Fig. 2.3.1(a)) consists of a “D”-shaped bulk HTS, a copper material part, and a rectangular hole that is placed in the middle so that the electron beams can pass through it (Fig. 2.3.1(b)). In our study, the SAU consisted of 21 basic units, with 11 HTSs on the top and 10 HTSs on the underside that were alternatively assembled (Fig. 2.3.1(b)). Fig. 2.3.1 (c) shows a schematic side view of the SAU prototype. Inserting the double vacuum duct allows liquid nitrogen to be introduced in intermediate layers, and the operation to be implemented on the central axis of the solenoid, which covers the outer wall of the duct with a vacuum insulation plate. To measure the magnetic field, a Hall sensor used at a low temperature was fixed on a resin plate that was attached to the tip of a straight introducer, and then the operation was implemented on the center axis of the solenoid. The temperature of bulk HTSs can be measured using a platinum resistance thermometer (PT100) that is attached to them.

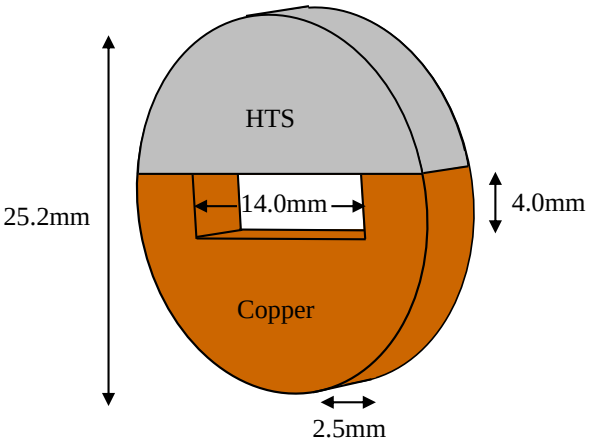

(a) Basic unit

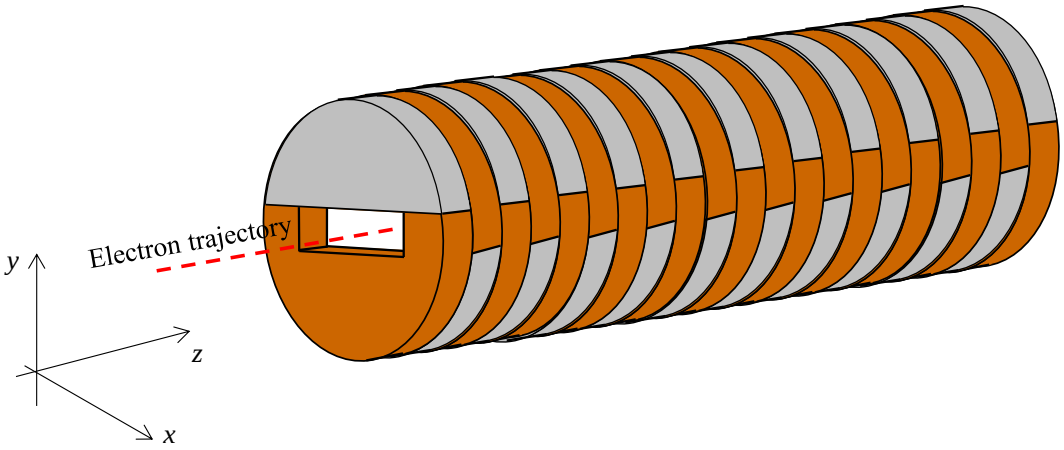

(b) Array unit

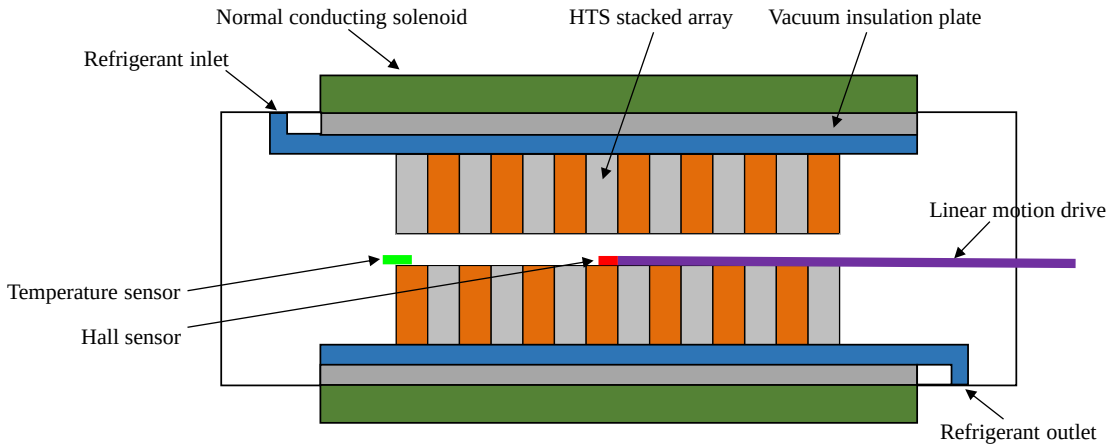

(c) Schematic side view of the prototype

Fig. 2.3.1 Overview of Bulk HTSC SAU.

(2) Principle of Operation

In Bulk HTSC SAU, since the induced currents are induced in every HTS, an alternative vertical (*y*-direction) magnetic field can be created along the electron trajectory, which creates the undulator motion of the election beam. This means that after all the HTSs are cooled to below the critical temperature in the cryostat and changed to superconducting state, the magnetic fields are changed by the solenoid coils, and then, an induced current is generated to offset the change in the magnetic field. Since the induced currents are affected by the magnetic fields produced by the other HTSs (according to the superposition principle), the change in magnetic fields corresponds to the magnetic field change caused by solenoid coils and magnetic fields created by HTSs. The induced currents appear from the outer edge of every HTS. Then, an alternative vertical (y-direction) magnetic field can be created along the electron trajectory on the central axis of the solenoid coils.

Fig. 2.3.2 shows the magnetic lines of force produced by the SAU around the electron trajectory. Although the direction of the magnetization of HTSs is completely different from that of a conventional undulator (Fig. 2.3.1), the alternative vertical (*y*-direction) magnetic field along the electron trajectory can be produced on the middle horizontal plane in the rectangular aperture of the SAU, which leads to the undulator motion of the electron beam.

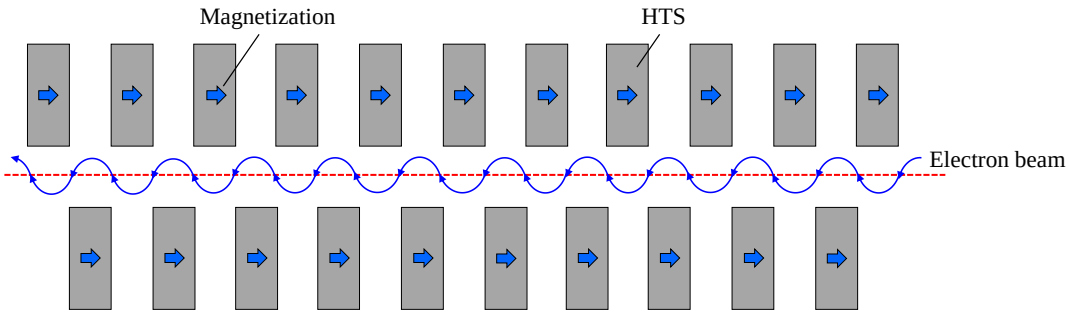

Fig. 2.3.2 Magnetic lines of force on z-axis in SAU.

Characteristic:

(a) Advantages

It is possible to generate a magnetic field by using the HTSs, which was previously impossible with the conventional HTS magnet arrangement. It is also possible to generate the periodic magnetic field, in which HTSs can be magnetized using a single solenoid and the magnetic field can be controlled without a drive mechanism.

(b) Disadvantages

There are two problems with SAU. Firstly, the strength of the magnetic field generated by the electron orbit is very small, and secondly, there is almost no experimental data that would contribute to verifying the validity of the simulation code.

2.3.2 Pure-type HTS Unudlator

Why do we use pure-type high-Tc (HTS) undulator:

It is generally necessary to achieve a uniform sinusoidal distribution of the magnetic field in the vertical direction for the operation of free-electron lasers (FELs) lasers that use HTSs. We have determined the suitable size and alignment of the HTS magnets based on the simulation of the magnetization process. In particular, a numerical simulation code that considers the interactions of magnetic fields between HTS magnets has been developed to simulate the magnetization process of the bulk HTSC SAU, and a single electron trajectory has been estimated for use in the design stage of the HTSs undulator. However, since almost no experimental data, nor other direct measurement data, exists on SAU, the validity of the developed numerical code can only be confirmed using the levitation force in the magnetic levitation experiment done on bulk HTSs.

A large number of experiments that are different from the SAU have been conducted

to directly experimentally measure the vertical magnetic field distributions of FEL undulators (which use HTS magnets). In particular, the use of pure-type HTS undulators, one of possible HTS magnet arrays for FEL undulators, was put forward by T. Tanaka in REKEN, and the vertical magnetic field distributions of these undulators in the magnetization process have also been experimentally measured. Therefore, it is necessary to use the pure-type HTS undulator in this study, to expand upon the available data.

(1) Structure

Fig. 2.3.3 gives a structural overview of the experimental pure-type HTS undulator, which is made up of three HTS magnets, each magnet having an individual size of 10mm × 15mm × 4mm (Fig. 2.3.4) [2]-[3]. In Fig. 2.3.4, the HTS magnets (composed by GdBaCuO Superconductor), are inserted in the electromagnets' gap. The temperature can be controlled using a cartridge-type heater that is installed on the copper plate. A Hall probe, which is inserted on the opposite of the HTS magnets, can measure the magnetic

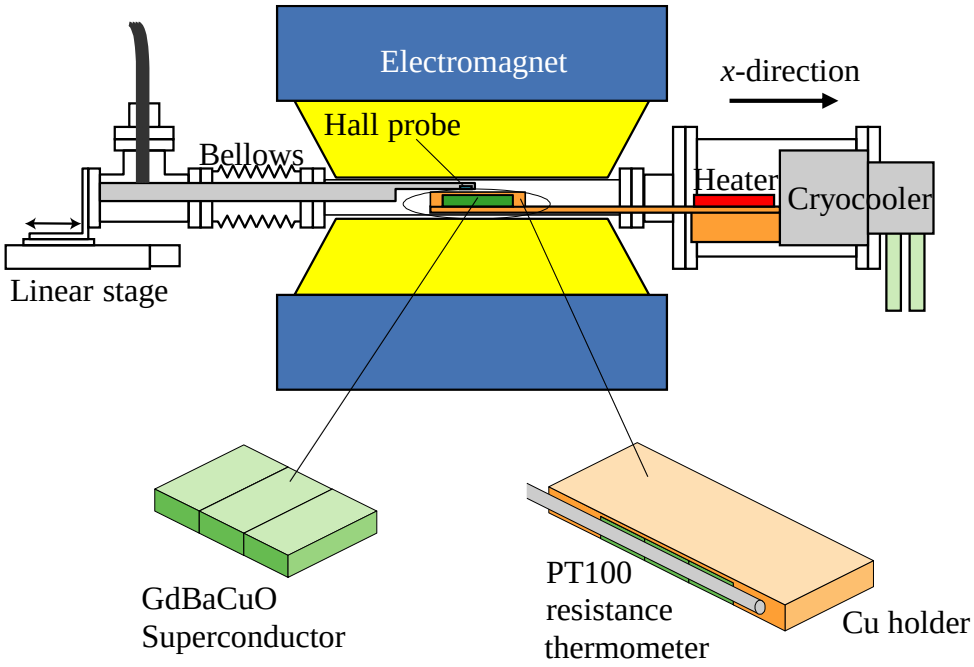

Fig. 2.3.3 Schematic illustration of the experimental device of pure-type HTS undulator.

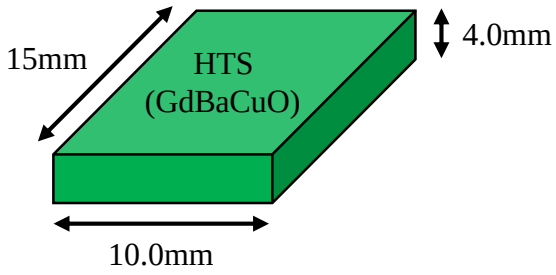

Fig. 2.3.4 Size of one HTS magnet.

field in the longitudinal direction as it is connected to a linear stage. The distance from the surface of the HTS magnets to the Hall probe is 1mm, so the gap value is 2mm. The temperature of HTS magnets can be measured by using a platinum resistance thermometer that is attached to them.

(2) Principle of Operation

Fig. 2.3.5 gives an overview of a pure-type HTS undulator composed of three HTS magnets that are separate from each other. After all the HTS magnets are cooled to below the critical temperature in the cryostat and changed to the superconducting state, the external magnetic fields are changed from B_{max} = 2.0 T to B_{min} = -0.6 T by temporal change, and then, an induced current is generated to offset the change in magnetic field at around B_0 = -0.5 T. Since the induced currents will be affected by the magnetic fields produced by other HTSs (according to the superposition principle), the change in magnetic fields corresponds to the change caused by solenoid coil and the HTS-created magnetic fields. Shielding currents appear in every HTS magnet, therefore, alternative vertical magnetic fields are created along the electron trajectory using these shielding currents and can be utilized in the FEL undulator (Fig. 2.3.6). Since these magnetic fields are very close to the magnets, they can be expected to be much stronger than the magnetic

fields in the SAU.

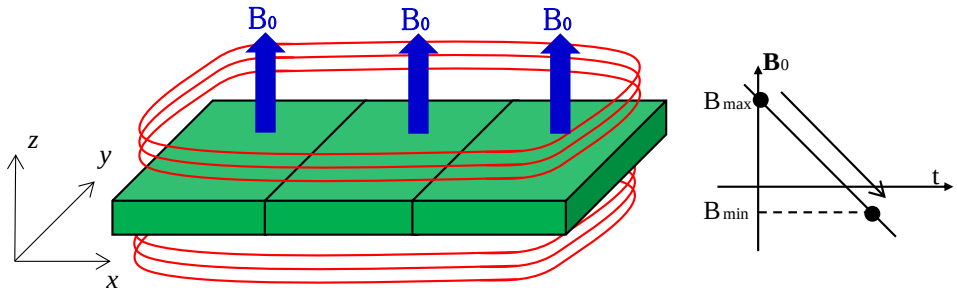

Fig. 2.3.5 Overview of Pure-type HTS undulator.

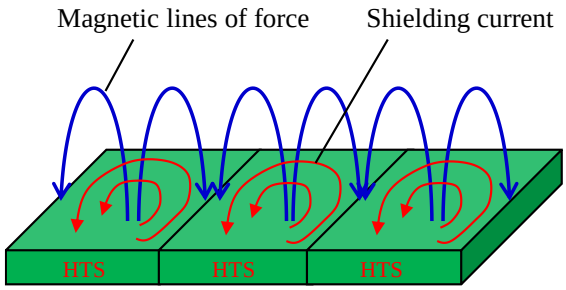

Fig. 2.3.6 Shielding currents and magnetic fields.

In this chapter, we have introduced two kinds of bulk HTS magnets: SAUs and pure-type HTS undulators, respectively. In the HTS undulator's design stage, it is known that very uniform vertical sinusoidal magnetic fields have to be created at the undulator for normal operation of the FEL. It is also impossible to re-arrange the alignment of the bulk HTS magnets after they change to a superconducting state inside a cryostat, however, the distribution of the vertical magnetic field component will not be uniform if pure-type HTS undulators or SAUs are constructed using same-sized HTS magnets. Accordingly, it is important to predict the magnetization process of pure-type HTS undulator or SAU using a numerical simulation, and then to determine the suitable size and alignment of the bulk HTS magnets to create a uniform sinusoidal distribution in the vertical component of the magnetic field at the X-FEL's design stage.

Chapter 3

Fundamental Theories

In Chapter 2, it is made known that the simulation of the magnetization process is very important in the X-FEL design stage. In this Chapter, we will briefly introduce some fundamental theories for numerical simulations, such as Maxwell's equations, eddy current fields, superconductivity, and electron motion equations.

3.1 Maxwell's Equations

Maxwell's equations are a set of 4 partial differential equations that describe the world of electromagnetics. These equations describe how electric fields and magnetic fields are generated by charges and electric currents, and how they will propagate, interact with each other, and be influenced by other objects. The following 4 equations are the classical forms of Maxwell's Equations.

Gauss's law of electric fields can be expressed as:

$$\nabla \cdot \mathbf{D} = \rho \tag{3.1.1}$$

Gauss's law of magnetism can be expressed as:

$$\nabla \cdot \mathbf{B} = 0 \tag{3.1.2}$$

Ampère's circuital law can be expressed as:

$$\nabla \times \mathbf{H} = \mathbf{J} + \frac{\partial \mathbf{D}}{\partial t} \tag{3.1.3}$$

Faraday's law of induction can be expressed as:

$$\nabla \times \mathbf{E} = -\frac{\partial \mathbf{B}}{\partial t} \tag{3.1.4}$$

Two supplementary expressions of Maxwell's equation, the electric flux and the magnetic flux, which are concerned with the areal density of the dielectric constant or and permeability, can be expressed as the following:

$$\mathbf{D} = \varepsilon\mathbf{E} \tag{3.1.5}$$

$$\mathbf{B} = \mu\mathbf{H} \tag{3.1.6}$$

and, the current density and the electric field are connected to the conductivity σ of the conductor by Ohm's law, which is expressed as the following equation:

$$\mathbf{J} = \sigma\mathbf{E} \tag{3.1.7}$$

As the foundation of classical electromagnetism, classical optics, and electric circuits, most of the electromagnetic properties that are required for microwave engineering can be deduced from Maxwell's equations.

3.2 Eddy Current Field

When the electric current flows through a coil inside a conductor, the magnetic field also changes temporally. In this way, when a varying magnetic field is applied to the conductor, a current flows into the conductor according to Faraday's law of induction. A magnetic field is applied in a direction that is perpendicular to the surface of the conductor, and if the magnetic field changes temporally, circular electric currents flow onto the surface. These electric currents create a new magnetic field apart from the afore-mentioned magnetic field according to Ampère's circuital law. Since a magnetic field is newly generated, the electric currents flow according to Faraday's law of induction again. The electric currents also create a new magnetic field. By this repetition, a circular current gathers in the conductor in the direction of the magnetic field and then, the electric currents flow like a vortex. These electric currents are called eddy currents.

Assuming that the external magnetic field applied to conductor is $\mathbf{B}_0$, and the magnetic field produced by the eddy current is $\mathbf{B}_e$, the electric field generated by the magnetic field according to Faraday's law of induction is **E**. The relationship between the electric field and the magnetic field can therefore be expressed in the following equation:

$$\nabla \times \mathbf{E} = -\frac{\partial}{\partial t}(\boldsymbol{B}_0 + \mathbf{B}_e) \tag{3.2.1}$$

Next, we will describe the magnetic field **H** that is generated by the electric current. It is known that the displacement electric current can be negligible relative to the conduction electric current when the frequency of the electric field **E** is small or the conductivity σ of the conductor is large. Therefore, using Ampère's circuital law (3.1.3) and Ohm's law (3.1.6), the relationship between the electric current and the magnetic field can be expressed by the following equation:

$$\nabla \times \mathbf{H} = \mathbf{J}_0 + \mathbf{J}_c = \mathbf{J}_0 + \sigma\mathbf{E} \tag{3.2.2}$$

where $\mathbf{J}_0$ is the current density generated by the change in the $\mathbf{B}_0$ and $\mathbf{J}_c$ ($\sigma\mathbf{E}$) values is the current density generated by the change in $\mathbf{B}_e$.

The electric field is generated by the flow of the charges, then, the charges' bias is eliminated by the rapid scattering effect caused by repulsive forces between charges. Since the redistribution of charges cancels the inside of the electric field, the electric field in the conductor will disappear immediately after it is generated, and free electrons will also disappear. It means that there are no new electric fields and new electric currents can be generated. Therefore,

$$\nabla \cdot \mathbf{E} = 0 \tag{3.2.3}$$

$$\nabla \cdot \mathbf{J}_c = 0 \tag{3.2.4}$$

can be obtained.

Although the charge conservation law for the eddy current $\mathbf{J}_c$ is defined by equation (3.2.4), using the compatibility of equation (3.2.2)

$$\nabla \cdot \mathbf{J}_0 = 0 \tag{3.2.5}$$

needs to be satisfied for the external electric current $\mathbf{J}_0$.

In addition, as was the case with equation (3.1.2), Gauss's law can be expressed using the following equation:

$$\nabla \cdot (\mathbf{B}_0 + \mathbf{B}_e) = 0 \tag{3.2.6}$$

In summary, Maxwell's equations in the eddy current field can be expressed by the following equations:

$$\nabla \times \mathbf{E} = -\frac{\partial}{\partial t}(\mathbf{B}_0 + \mathbf{B}_e) \tag{3.2.1}$$

$$\nabla \times \mathbf{H} = \mathbf{J}_0 + \sigma\mathbf{E} \tag{3.2.2}$$

$$\nabla \cdot \mathbf{E} = 0 \tag{3.2.3}$$

$$\nabla \cdot (\mathbf{B}_0 + \mathbf{B}_e) = 0 \tag{3.2.6}$$

Since eddy currents are generated to counteract changes in the external magnetic field, the eddy current will interrupt the incoming magnetic field. Therefore, it also acts as a "shielding current" for the magnetic field.

Next, we will introduce one of the methods for analyzing the eddy current. Firstly, just as was the case with the static magnetic field, the magnetic vector potential that satisfies the equation (3.1.2) can be expressed with the following equation:

$$\mathbf{B} = \nabla \times \mathbf{A} \tag{3.2.7}$$

From equation (3.2.7), it is easy to see that **B** will not change, even as a scalar function is added to **A** such as $\mathbf{A} + \text{grad}\emptyset$. Thus, **A** has an arbitrary value within the gradient of a scalar function. Eliminating the arbitrariness of A is called gauge fixing. There exist Lorenz and Coulomb gauge-fixing conditions with $\nabla \cdot \mathbf{A} = 0$ for gauge fixing.

By substituting equation (3.2.5) into Faraday's law of induction (3.1.4)

$$\nabla \times \left(\mathbf{E} - \frac{\partial \mathbf{A}}{\partial t}\right) = 0 \tag{3.2.8}$$

can be obtained. Then, the electric field E can be written as following equation:

$$\mathbf{E} = -\nabla\emptyset - \frac{\partial \mathbf{A}}{\partial t} \tag{3.2.9}$$

where $\emptyset$ is scalar potential.

Then, substituting equations (3.1.7), (3.2.7) and (3.2.8) into equation (3.2.2),

$$\nabla \times \left(\frac{1}{\mu}\nabla \times \mathbf{A}\right) = -\sigma\nabla\emptyset - \sigma\frac{\partial \mathbf{A}}{\partial t} + \mathbf{J}_0 \tag{3.2.10}$$

can be obtained. Then, the left side of the equation can be expressed as the following equation:

$$\nabla \times \left(\frac{1}{\mu}\nabla \times \mathbf{A}\right) = \frac{1}{\mu}(\nabla(\nabla \cdot \mathbf{A}) - \nabla^2\mathbf{A}) \tag{3.2.11}$$

And equation (3.2.11) can be organized as the following equation:

$$\sigma\mu\frac{\partial \mathbf{A}}{\partial t} + \sigma\mu\nabla\emptyset - \nabla^2\mathbf{A} = \mathbf{J}_0 \tag{3.2.12}$$

Since equation (3.2.12) contains **A** and $\emptyset$ as its unknown functions, the equation cannot be solved. Therefore, using the divergent equation of equation (3.2.5) produces the following equation:

$$\nabla \cdot \sigma\left(\frac{\partial \mathbf{A}}{\partial t} + \nabla\emptyset\right) = 0 \tag{3.2.13}$$

In summary, the method is usually called **A**–$\emptyset$ method, which involves solving for the unknown functions **A** and $\emptyset$ in the simultaneous equations (3.2.12) and (3.2.13).

3.3 Superconductivity

Superconductivity is the phenomenon in which a certain material will exhibit zero electrical resistance and expel magnetic fields under a critical temperature T_c (Fig. 3.3.1).

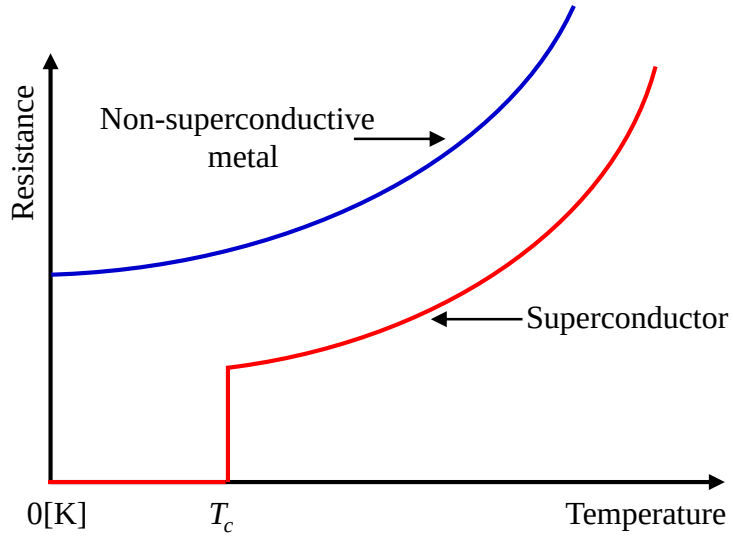

Fig. 3.3.1 Critical temperature of superconductor compared to normal metal.

3.3.1 History of Superconductivity

The history of superconductivity began in 1911, when Dutch physicist H. K. Onnes discovered that the electric resistance of mercury disappeared below 4.2 K (-268.8 °C). In 1933, the phenomenon of the expulsion of a magnetic field from a superconductor during its transition to the superconducting state was found by the German physicists W. Meissner and R. Ochsenfeld [43] and was called the Meissner effect. F. London and H. London showed that the Meissner effect was a consequence of the minimization of the electromagnetic free energy carried by superconducting currents in 1935 [44]. In the 1950s, two central theories were developed: the Ginzburg-Landau theory, named after V. L. Ginzburg and L. Landau in 1950, and the microscopic BCS theory, named by J. Bardeen, L. Cooper and J Robert Schrieffer in 1957 [45]-[46]. The BCS theory describes

superconductivity as being a transition into a boson-like state observed at the microscopic level, which is caused by a condensation of Cooper pairs, and at a superconducting transition temperature that is limited to 40 K (-233 °C). In 1962, a macroscopic quantum phenomenon called the Josephson Effect, in which currents can flow between two pieces of superconductor separated by a thin layer of insulator, was predicted by Josephson [47] and it is widely used in various applications such as in the SQUIDs superconducting devices.

Until 1986, the material with the highest-temperature T_c under the highest ambient-pressure is Nb_3Ge of 23 K. In a surprising 1986 report, J. G. Bednorz and K. A. Mueller [48] claimed to have discovered superconductivity in a lanthanum-based cuprate-perovskite material, which had a transition temperature of 35 K. Three months later, it was found that replac the lanthanum with yttrium to make YBCO could raise the critical temperature to 92 K [49]. This is very important since liquid nitrogen can be widely used as a refrigerant very at very little cost. This discovery led to an increasing global trend in favor of research on copper oxide superconductors.

In 1993, a superconductor (a ceramic material) consisting of $HgBa_2Ca_2Cu_3O_{8+\delta}$ was found with T_c = 133-138 K [50]-[51]. In 2015, the highest-temperature superconductor H_2S was found to undergo superconducting transition near 203 K (-70 °C) under extremely high pressure (around 150 MPa) [52].

3.3.2 Perfect Conductivity of Superconductors

Perfect conductivity of superconductors is a phenomenon in which the resistance of superconductors will become 0 when the temperature falls below a threshold temperature T_c. In this context, the voltage will not drop and the energy dissipation by Joule heat will

not occur. In this important phenomenon in superconductivity, as shown in Fig. 3.3.1, the resistance of a certain material will rapidly disappear at temperature T_c — the superconducting transition temperature or superconducting critical temperature — that is different than the critical temperature for non-superconductive metals.

3.3.3 Meissner Effect

The Meissner effect is a phenomenon in which the magnetic field is expelled from materials during their transition to the superconducting state [43]. Fig. 3.3.2 illustrates the expulsion of the magnetic field and the situation in which the magnetic flux of density *B* inside the superconductor becomes zero when the temperature drops below *Tc* in a weak magnetic field. The magnetization is defined by *M*, using the definition of magnetic file density $B = \mu 0 (H+M)$, the magnetization $M = -H$ is induced to offset the external magnetic field. The reason for which the magnetic field is inside the superconductor is that the diamagnetic current flows on the surface of the superconductor to offset the external magnetic field.

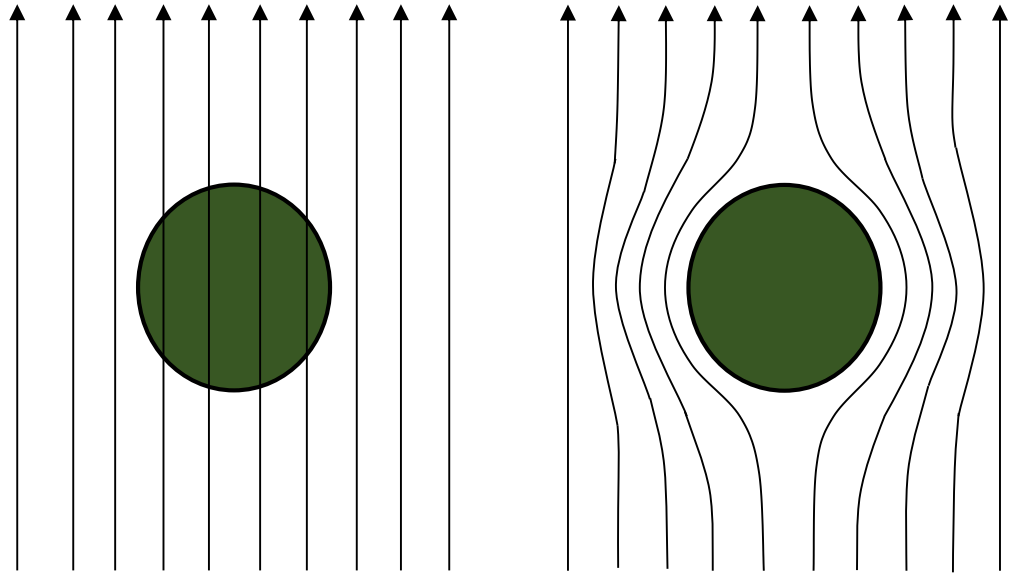

(a) Normal conducting state ($T<T_c$) (b) Superconducting state ($T>T_c$)

Fig. 3.3.2 Meissner effect.

However, the diamagnetic current is not sufficient to offset the whole external magnetic field, even in the Meissner state. One of the most important characteristics for superconductivity, the thickness of the surface layer where the magnetic field enters and the diamagnetic current flows, is called London penetration depth λ. Therefore, a magnetic field only penetrates into a superconducting film that is thinner than λ.

In addition, if the external magnetic field H is strengthened, the superconducting state will be broken and return to its normal conducting state. There are two ways to break the superconducting state:

Fig. 3.3.3 (a) shows a type-I superconductor, in which superconductivity is suddenly destroyed via a first order phase transition when the strength of the applied field rises above a critical value H_c, as is the case with pure metals such as Pb, Sn, Al.

Fig. 3.3.3 (b) shows a type-II superconductor, in which a magnetic field will penetrate the superconductor above a critical field strength H_{c1}, and then, after it is larger than H_{c2} (larger than H_c), superconductivity will be destroyed. Most alloys and compounds are type-II superconductors.

The type of superconductor is also determined by the equation $\kappa \equiv \lambda/\xi$, where λ is the London penetration depth, ξ is the coherence length and κ is the Ginzburg-Landau

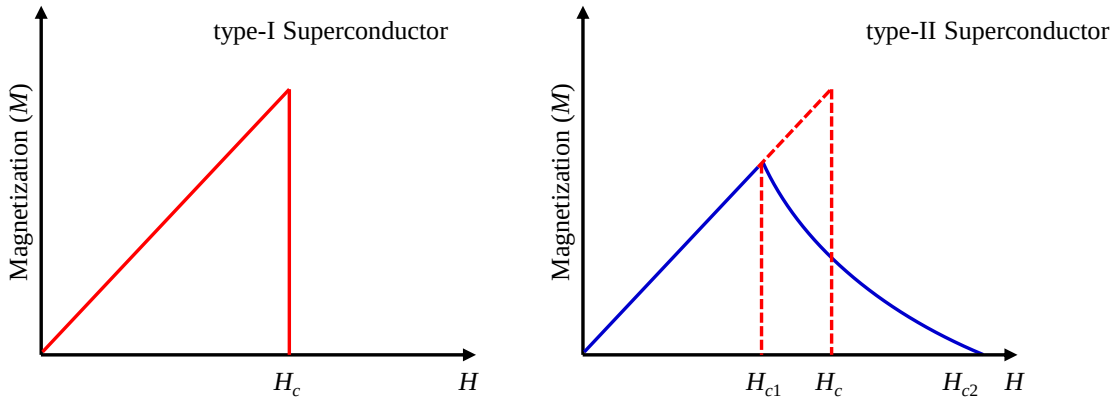

(a) type-II (b) type-II

Fig. 3.3.3 *B*-*H* curve.

parameter. Type-I superconductors exist when $\kappa < 1/\sqrt{2}$, and type-II superconductors do when $\kappa \equiv> 1/\sqrt{2}$.

3.3.4 London theory

The London theory explains the Meissner effect of type-I superconductors using the behavior of superconducting electrons [44].

Firstly, the electric current density **J** is defined by the following equation:

$$\mathbf{J} = n_s e^* \boldsymbol{v_s} \tag{3.3.1}$$

where, e is a charge of electric current, n_s is density and v_s is speed.

Then, since electrons are affected by external influences due to scattering and collision, the equation of motion can be expressed as:

$$e^*\mathbf{E} = m^* \frac{\partial \mathbf{v}_s}{\partial t} + \nu \mathbf{v}_s \tag{3.3.2}$$

where, m is mass and ν is proportional factor.

In ordinarily good conductors, the current carriers are normal conduction electrons.

Considering an elapsed time that is longer than the diffusion time of electrons, the inertia term can be ignored, and the equation of motion can be written as follows:

$$e^*\mathbf{E} = \nu \mathbf{v}_s \tag{3.3.3}$$

then, by combining equation (3.3.3) with equation (3.3.1)

$$\mathbf{J} = \frac{m^*}{n_s e^{*2}} \tag{3.3.4}$$

Next, we can assume that the current carriers are superconducting electrons. Since electrons are not affected by external influences due to scattering and collision, the equation of motion can be expressed as the following:

$$e^*\mathbf{E} = m^* \frac{\partial \mathbf{v}_s}{\partial t} \tag{3.3.5}$$

assuming that

$$\Lambda = \frac{m^* \partial \mathbf{v}_s}{\partial t} \tag{3.3.6}$$

the following equation can be obtained:

$$\mathbf{E} = \Lambda \frac{\partial \mathbf{J}}{\partial t} \tag{3.3.7}$$

The equation (3.3.7) is a constitutive law derived from perfect conductivity, which is the most fundamental property of superconductivity.

Next, we will consider another basic property of superconductivity: super diamagnetism. Firstly, by substituting equation (3.1.4) into equation (3.3.7),

$$\frac{\partial}{\partial t}(\nabla \times \Lambda \mathbf{J} + \mathbf{B}) = 0 \tag{3.3.8}$$

since,

$$\nabla \times \Lambda \mathbf{J} + \mathbf{B} = C(x, y, z) \tag{3.3.9}$$

where *C* is a time independent function. We only use Maxwell's equations and assume perfect conductivity of superconductors, so that in order to describe the Meissner effect, a theoretical leap is required. Therefore, the magnetic fields and the currents do not exist inside the superconductor in a completely diamagnetic state, **B** = 0 and **J** = 0 in the equation (3.3.9), and *C*(*x*, *y*, *z*) = 0. One hypothesis is introduced in the following equation:

$$\nabla \times \Lambda \mathbf{J} + \mathbf{B} = 0 \tag{3.3.10}$$

and now, equation (3.3.10)—otherwise known as the London equation—will be used to explain the Meissner effect.

Firstly, from the Maxwell equation,

$$\nabla \times \mathbf{B} = \mu_0 \mathbf{J} \tag{3.3.11}$$

We will include an additional rotation,

$$\nabla \times \nabla \times \mathbf{B} = \mu_0 \mathbf{J} \tag{3.3.12}$$

substitute equation (3.3.10)

$$\nabla \times \nabla \times \mathbf{B} = \nabla(\nabla \cdot \mathbf{B}) - \nabla^2 \mathbf{B} \tag{3.3.13}$$

from the vector equation:

$$\nabla^2 \mathbf{B} = \frac{1}{\lambda^2{}_L} \mathbf{B} \quad \text{However} \quad \lambda_L = \left(\frac{\Lambda}{\mu_0}\right)^{\frac{1}{2}} = \left(\frac{m^*}{\mu_0 n_s e^{*2}}\right)^{\frac{1}{2}} \tag{3.3.14}$$

where, λ_L is London penetration depth.

Then, considering a uniform magnetic field that is applied to a superconductor, and solving this equation under the condition $B = B_0$ at the boundary $x = x_0$ results in

$$\mathrm{B(x)} = B_0 e^{-\frac{x - x_0}{\lambda_L}} \tag{3.3.15}$$

The magnetic field penetrates only to a depth of about λ_L. Then, the conventional materials are of sizes 10 to 100 nm, thus explaining why the magnetic field inside the superconductor is zero.

3.3.5 Ginzburg-Landau Theory

Ginzburg-Landau theory is a phenomenological theory of thermal equilibrium enunciated in 1950 that combines thermodynamics and electromagnetics. The theory is based on Landau's previously-established theory of second-order phase transitions, and uses an order parameter representing the order of superconductivity with ψ and expresses the Ginzburg-Landau equation with vector potential *A*.

(1) Free energy

For the basic assumption (the superconductivity is also taken into account), the free energy *f* per unit volume of conductor can be expressed as:

$$f = f_n + \alpha|\psi|^2 + \frac{\beta}{2}|\psi|^4 + \frac{1}{2m^*}\left|\left(\frac{\hbar}{i} - e^*\mathbf{A}\right)\psi\right|^2 + \frac{|\mathbf{B}|^2}{2\mu_0} \quad (3.3.16)$$

where f_n is the free energy density in the normal conducting state, α and β are temperature functions when developed by using $|\psi|^2$ in the superconducting state, and m* and e* are the mass and charge of the superconducting electron.

(2) Ginzburg-Landau equations

Variations of free energy can be expressed using the following equation:

$$\alpha|\psi|^2 + \beta|\psi|\psi^4 + \frac{1}{2m^*}\left(\frac{\hbar}{i}\nabla - e^*\mathbf{A}\right)^2\psi + \frac{|\mathbf{B}|^2}{2\mu_0} = 0 \quad (3.3.17)$$

The quantum mechanical current density can be expressed as:

$$\boldsymbol{J} = \frac{\hbar e^*}{2m^* i}(\psi^*\nabla\psi - \psi\nabla\psi^*) - \frac{e^{*2}\boldsymbol{A}}{m^*}|\psi|^2 \quad (3.3.18)$$

These two equations are generally called Ginzburg-Landau differential equations.

(3) Ginzburg-Landau parameter

The coherence length ξ, which is the distance at which superconducting electrons are correlated,

$$\boldsymbol{\xi} = \sqrt{\frac{\hbar}{2m^*\alpha}} \quad (3.3.19)$$

And the London penetration depth λ, which is the penetration depth of the magnetic flux introduced,

$$\lambda = \sqrt{\frac{m}{4\mu_0 e^{*2}\psi}} \quad (3.3.20)$$

And the ratio of the two

$$\kappa = \frac{\lambda}{\xi} \quad (3.3.21)$$

is called the parameter of Ginzburg-Landau, and it determines the behavior

of the superconductor when a magnetic field is applied.

3.3.6 Quantization of Magnetic Flux

The phenomenon of flux quantization was discovered by B. S. Deaver and W. M. Fairbank [53]. Fig. 3.3.4 shows the persistent current I_s flowing through the superconducting ring, and the magnetic field generated by the circulating current in the ring. The area fraction of the magnetic field and the magnetic flux Φ penetrating the

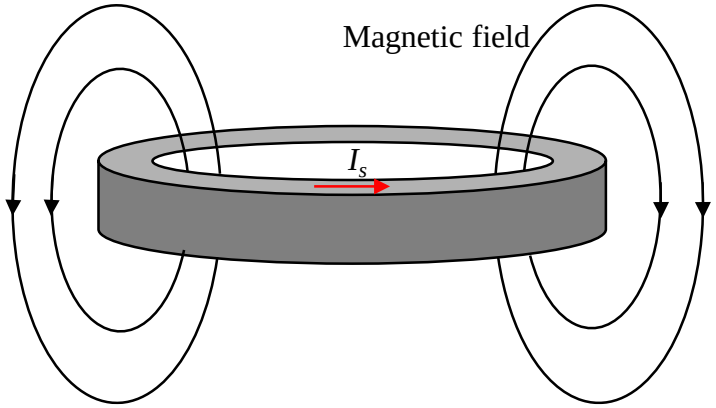

Fig. 3.3.4 Magnetic field and persistent current in a superconducting ring.

hollow portion surrounded by the superconductor have been calculated. The self-inductance of the ring is L and $\Phi = LI_s$. These show that this magnetic flux must only take discrete values represented by an integral multiple $\Phi = n\Phi_0$ of a certain small universal quantity Φ_0. This is called the quantization of magnetic flux.

Experiments conclude that the value of Φ_0 is 2.07 fWb, corresponding to $h/2e$ if the Planck constant is h and the elementary charge is e, and is called the flux quantum. Factor 2 in the denominator of flux quantum $\Phi_0 = h/2e$ suggests the important phenomenon of electron pairing in the superconducting state. In general, since magnetic fluxes repel one another, energy is lower when magnets are as far from each other as possible, rather than being clumped. However, the quantization of magnetic flux means that the magnetic flux penetrating the space surrounded by the superconductor cannot be divided into smaller

quantities than Φ_0.

For this reason, even the magnetic flux penetrates in the mixed state of the type-II superconductor, and the unit of magnetic flux needs to be set at Φ_0. When a magnetic field is applied to the mixed state of the type-II superconductor, the magnetic flux penetrates into the normal conducting region surrounded by the superconducting region. The penetrating magnetic flux is quantized to the level of $h/2e$ as described above, which is an integral multiple $n\Phi_0$ of the flux quantum, which is energetically stable.

3.3.7 Flux Pinning

In superconductivity, micro quantum phenomena have characteristics that can be observed as macroscopic phenomena, such as flux quantum.

Flux pinning, as a very important concept in superconductivity, is a phenomenon in type-II superconductors that the lines of magnetic flux will not move in spite of the Lorentz force acting on them inside a current-carrying. This phenomenon only happened in type-II superconductors, as type-I superconductors cannot be penetrated by magnetic fields.

When a current is applied from the outside of type-II superconductors, the Lorentz force acts in the direction of $\mathbf{J}\times\mathbf{B}$ in the flux quantum and the flux quantum starts to move. At this moment, the conduction electrons in the normal conduction nucleus will move, and the kinetic energy of the conduction electrons change to thermal energy by collision or scattering. And then, the superconducting state is destroyed by the temperature rise, but this will not occur in an actual superconductor. Since the impurities and lattice defects exist in actually used superconductors, and the magnetic flux quantum is captured then the potential decreases (infinite potential well). That means, even a force is applied in the

direction of **J**×**B**, the flux quantum is trapped in the infinite potential well and the movement is hindered. This is called flux pinning, the pinning center is the place where pinning is done, and the force against the Lorentz force is usually called the pinning force.

This phenomenon is a relation to critical current density in type-II superconductors. It is known that the magnetic flux passing through the superconductor receives a force from the magnetic field generated by the current, and the magnetic flux will start to move out of the pinning constraint when the current exceeds the critical value.

An overview of flux pinning is shown in Fig. 3.3.5.

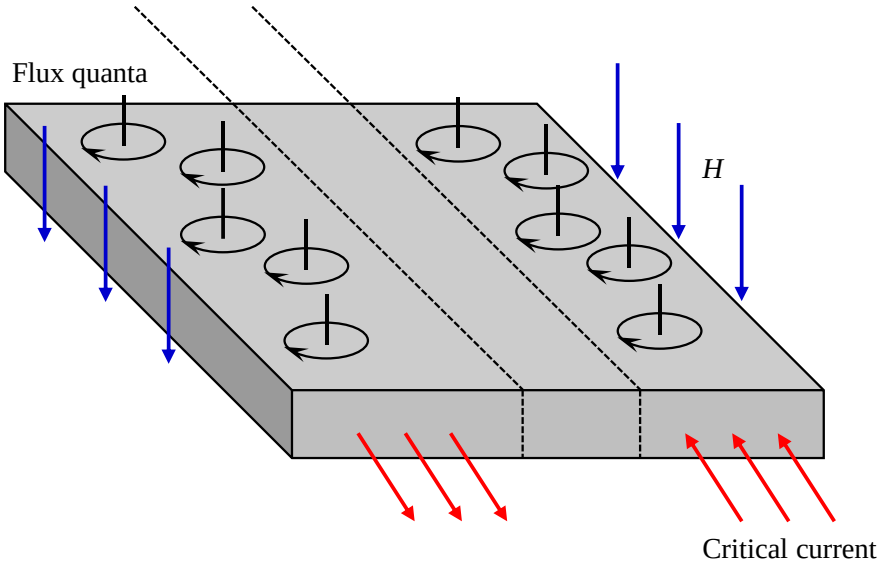

Fig. 3.3.5 Overview of flux pinning.

3.3.8 High-Tc Superconductor (HTS)

(1) History of High-temperature Superconductors

High-temperature superconductors (usually short for high-Tc superconductor or HTS), are materials that behave as superconductors at high temperatures. Generally, the definition of high temperatures is a T_c that is above 25 K. The first high-Tc superconductor was discovered by IBM researchers J. G. Bednorz and K. A. Müller in 1986 [48], resulting

in a surge in the research and development of high-Tc superconductors globally. High-Tc superconductor currently use a transition temperature higher than the temperature of liquid nitrogen, which is 77 K (-195.8 °C). It was found that the critical temperature can reach 92 K by replacing the lanthanum in the process with yttrium (YBCO) [49]. The highest-temperature superconductor in current use is H_2S, which undergoes superconducting transition near 203 K (-70 °C) under extremely high pressure (around 150 MPa) [52].

The critical temperature of the superconducting state has greatly improved after the discovery of high-Tc superconductivity. In addition, many scientists are researching room-temperature superconductivity, which may be achieved in the near future.

(2) Characteristics of high-temperature superconductivity

High-Tc superconductivity has greatly impacted research across all fields on superconductivity in recent years. The critical temperature Tc was initially 20-40K (La type), and then 90 K (Y type), 105 K (Bi type), and 120 K (Tl type) were discovered within a short period. Since the critical temperature of Y type (YBCO) superconductivity exceeds the liquid nitrogen temperature of 77K, it represents a big leap forward in superconducting applications.

As opposed to regular superconductivity, high-Tc superconductivity typically includes the following characteristics:

High critical temperature.

It is possible operate at a higher temperature, such as the liquid nitrogen temperature (77 K) instead of the liquid helium temperature (4 K).

Large superconducting energy gaps and short coherence lengths

The superconducting energy gap in high-Tc superconductivity is always several times

larger than in superconductivity, and the coherent length is significantly shorter than the superconductivity (from serval Å to serval nm).

(3) Construction

The definition of a high-Tc superconductor is that it has a critical temperature T_c above 25 K. Part of fullerene superconductor and MgB_2 that is found in Japan belongs to the copper oxide superconductors. Table 3.3.1 shows some kinds of the copper oxide superconductors, and the structural characteristics of their ionizing treatment [54].

Fig. 3.3.6 shows the structure of a typical oxide. In observing the atomic arrangement in the *c*-axis direction of these copper oxide superconductors, the structure can be considered to consist of only five kinds of layers (Fig. 3.3.7) [54]. The a layer consists of some atoms such as Bi, Hg, Tl, Pb or Ba, Sr, La, the b layer has oxygen deficiency (δ = 0~0.5: oxygen deficiency), the c layer is a metal ion such as Y, Ca, Sr, Nd, the d layer is a layer containing only oxygen ions, and the e layer is a superconducting layer composed of CuO_2. Fig. 3.3.10 shows the stacking on the *c*-axis using symbols like ceabaec, but various superconducting layers are formed according to the combination of the layers as shown in Table 3.3.1. The a and a' layers supply apical oxygen to the e layer, however the c layer is a metal layer and does not give oxygen to the e layer.

The crystalline structure of a copper oxide superconductor is composed of a surface of CuO_2 and a charge storage layer (block layer) on either side of the CuO_2 surface. In addition, the intermediate between the superconducting layer and the charge storage layer may be differentiated as a buffer layer or an intermediate layer in some cases. Although the CuO_2 surface originally acts as an antiferromagnetic insulator, the surface of CuO_2 can become metallic and develop superconductivity by doping electrons or holes as carriers to the surface of CuO_2 from the charge storage layer.

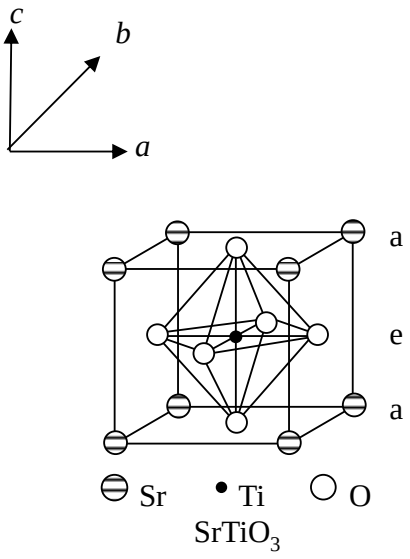

(a) Perovskite

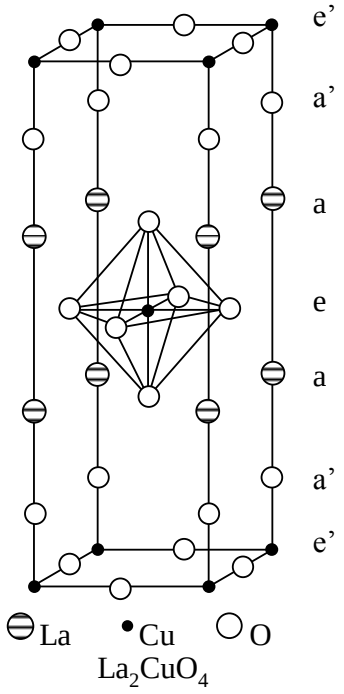

(b) Layered perovskite (T)

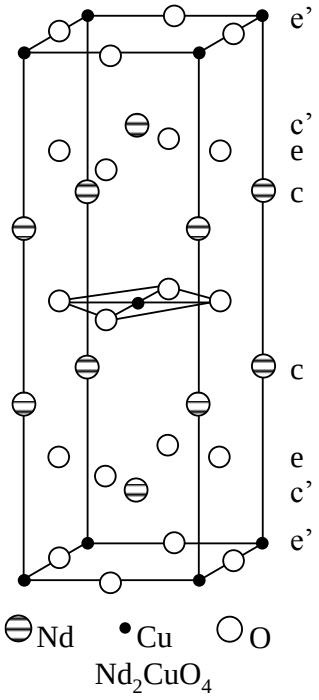

(c) Layered perovskite (T')

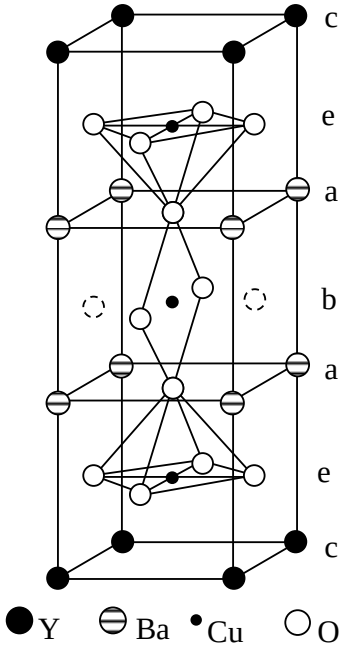

(d) Oxygen-deficient perovskite

Fig. 3.3.6 Crystal structure of a oxide superconductor.

Table 3.3.1 Classification of copper oxide superconductors and laminated structure of representative compounds

Chemical Alias	Examples	Laminated structure	T_c[K]
Infinite layer	(Sr, Nd)CuO_2	/ec/	44
214 series (T-structure)	(La, Sr)$_2CuO_4$	/aeaa'e'a'/	37
214 series (T'-structure)	(Nd, Ce)$_2CuO_4$	/cecdc'e'c'd/	22
La-212	(La, Sr)$_2CaCuO_6$	/aecea/	60
Y-123	$YBa_2CuO_3O_{6+\varepsilon}$	/aeceab/	93
Y-124	YBa_2Cu4O_8	/aeceabb/	90
Bi-2201	$Bi_2Sr_2CuO_6$	/a'ea'aa/	26
Bi-2212	$Bi_2Sr_2CaCu_2O_8$	/a'ecea'aa/	85
Bi-2223	$Bi_2Sr_2Ca_2Cu_3O_{10}$	/a'ececea'aa/	110
Hg-1201	$HgBa_2CuO_4$	/a'ea'a/	94
Hg-1223	$HgBa_2Ca_2CuO_{8.3}$	/a'ececea'a/	135
Tl-1212	(Tl, Pb)Sr_2(Ca, Y)Cu_2O_7	/a'ecea'a/	105
Tl-2223	$Tl_2Ba_2Ca_2CuO_{10}$	/a'ececea'aa/	117
Pb-1223	$PbBa_2Ca_2CuO_3O_9$	/a'ececea'a/	115

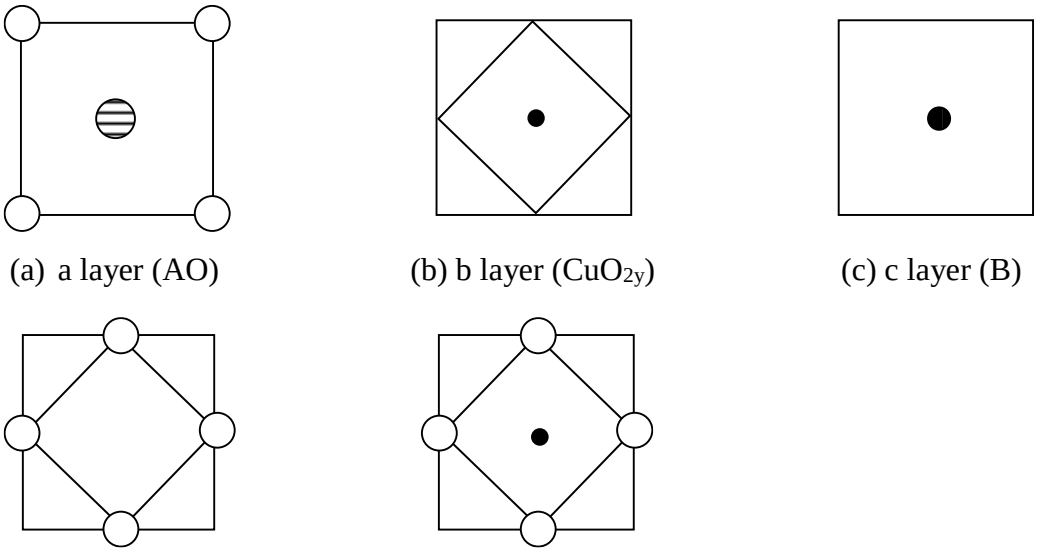

(a) a layer (AO) (b) b layer (CuO_{2y}) (c) c layer (B)

(d) d layer (O_2) (e) e layer (CuO_2)

Fig. 3.3.7 Five-type of layers in the copper oxide superconductor crystal.

3.4 Equation of Motion of Electron

An electric charge that is placed in the field not only receives the force from the field, but also affects the field and changes it. However, if the charge *e* is not large, the effect of the charge on that field and the change of field that it can cause can largely be ignored. In this case, if a charge moves in a given field, we assume that the field does not depend on coordinates or the speed of the charge.

The equation of motion of a charge in a given electromagnetic field can be expressed using the following equation (Euler-Lagrange equation):

$$\frac{d}{dt}\frac{\partial L}{\partial \mathbf{v}} = \frac{\partial L}{\partial \mathbf{r}} \tag{3.4.1}$$

L is a real-valued function with continuous first partial derivatives (Lagrangian):

$$L = mc^2\sqrt{1-\left(\frac{v}{c}\right)^2} + \frac{e}{c}\mathbf{A}\cdot\mathbf{v} - e\emptyset \tag{3.4.2}$$

where, *v* is the speed of an electron, *c* is the speed of light, *m* is the electron rest mass, **A** is a three-dimensional vector called vector potential, and $\emptyset$ is electrostatic potential.

The differential coefficient $\partial L/\partial v$ of equation (3.4.2) expresses the generalized momentum of the particle, and it can be represented by **P** in the following equation:

$$\mathbf{P} = \frac{m}{\sqrt{1-\left(\frac{v}{c}\right)^2}}c^2 + \frac{e}{c}\mathbf{A} = p + \frac{e}{c}\mathbf{A} \tag{3.4.3}$$

additionally,

$$\frac{\partial L}{\partial \boldsymbol{r}} \equiv \nabla L = \frac{e}{c}\nabla\mathbf{A}\cdot\mathbf{v} - e\nabla\emptyset \tag{3.4.4}$$

and using the vector analysis formula

$$\nabla(\mathbf{A}\cdot\mathbf{v}) = (\mathbf{A}\cdot\nabla)\mathbf{v} + (\mathbf{v}\cdot\nabla)\mathbf{A} + \mathbf{v}\times(\nabla\times\mathbf{A}) + \mathbf{A}\times(\nabla\times\mathbf{v}) \tag{3.4.5}$$

the integral for **r** is calculated by using the constant **v**

$$\frac{\partial L}{\partial \mathbf{r}} = \frac{e}{c}(\mathbf{v}\cdot\nabla)\mathbf{A} + \frac{e}{c}\mathbf{v}\times(\nabla\times\mathbf{A}) - e\nabla\emptyset \tag{3.4.6}$$

therefore, the Lagrange equation can be expressed as the following equation:

$$\frac{d}{dt}\left(\mathbf{P} + \frac{e}{c}\mathbf{A}\right) = \frac{e}{c}(\mathbf{v}\cdot\nabla)\mathbf{A} + \frac{e}{c}\mathbf{v}\times(\nabla\times\mathbf{A}) - e\nabla\emptyset \tag{3.4.7}$$

Here, the differential $(\partial\mathbf{A}/\partial t)\partial t$ consists of two parts: one is the temporal change $(\partial\mathbf{A}/\partial t)\partial t$ of the vector potential at a fixed point in space and the change caused by a displacement $\partial\mathbf{r}$ from that point, another is known in vector analysis as $(dr\cdot\nabla)\mathbf{A}$. Then, the differential coefficient $\partial\mathbf{A}/\partial t$ can be expressed using the following equation:

$$\frac{d\mathbf{A}}{dt} = \frac{\partial\mathbf{A}}{\partial t} + (\mathbf{v}\cdot\nabla)\mathbf{A} \tag{3.4.8}$$

and then, by substituting equation (3.4.8) into equation (3.4.7)

$$\frac{dp}{dt} = -\frac{e}{c}\frac{\partial\mathbf{A}}{\partial t} - e\nabla\emptyset + \frac{e}{c}\mathbf{v}\times(\nabla\times\mathbf{A}) \tag{3.4.9}$$

can be obtained. This is the equation of motion of particles in the electromagnetic field. The left side is the temporal derivative of the momentum of the particle. Therefore, the right side of equation (3.4.9) represents the force acting on the electric charge in the electromagnetic field. This power consists of two parts. The first part (the first and second terms on the right side of equation (3.4.9)) does not depend on particle velocity; the second part (the third term on the right side of equation (3.4.9)) is proportional to and orthogonal to speed.

The force per unit of charge of the first type is called the strength of the electric field and is represented by **E** in the following equation:

$$\mathbf{E} = -\frac{1}{c}\frac{d\mathbf{A}}{dt} - e\nabla\emptyset \tag{3.4.10}$$

The factor of **v**/*c* of the second type of force is related to the unit charge, which is called the strength of the magnetic field and represented by **H**, and it can be expressed by the

following equation:

$$\mathbf{H} = \nabla \times \mathbf{A} \tag{3.4.11}$$

where **E** is a polar vector and **H** is an axial vector.

In summary, the equation for the motion of an electric charge in the electromagnetic field can be expressed as the following equation:

$$\frac{d\mathbf{p}}{dt} = e\mathbf{E} + \frac{e}{c}\mathbf{v} \times \mathbf{H} \tag{3.4.12}$$

The right side of this equation is called the Lorentz force. The first term (the force of the electric field exerts on the charge) is not related to the speed of the charge and it faces the direction of **E**. The second term (the force that the magnetic field exerts on the charge) is proportional to the charge-transfer rate, and its direction is perpendicular to both speed and the magnetic field **H**.

When the speed is smaller than the speed of light, the momentum **p** is approximately equal to the expression $m\mathbf{v}$ of classical mechanics, and the equation of motion (3.4.12) can be expressed in the following equation:

$$m\frac{d\mathbf{v}}{dt} = e\mathbf{E} + \frac{e}{c}\mathbf{v} \times \mathbf{H} \tag{3.4.13}$$

Chapter 4

Formulations of Numerical Analysis

In this Chapter, we will briefly introduce the formulae used in the numerical analyses of the simulation of the magnetization process of the bulk HTS magnets. These include finite-difference methods, the current vector potential method for simulating the shielding currents and magnetic fields of bulk HTS magnets, and the Runge-Kutta method for simulating the electron trajectory.

4.1 Finite-difference Methods

4.1.1 Introduction

Finite-difference methods (FDM) are numerical methods of solving differential equations by approximating the difference equations. These methods can also be used to solve the boundary value problem and initial value problem in differential equations. Finite-difference methods are the most widely used discretization methods and have been in use for a very long time, so basic research on the stability of the calculation method and error evaluation of numerical solutions has been thoroughly conducted. Today, finite-difference methods are the dominant methods used in numerical solutions of partial differential equations, especially in fluid mechanics.

The basic outline of finite-difference methods is expressed in the following equation:

$$\frac{du}{dx} = \lim_{h \to 0} \frac{u(x+h) - u(x)}{h} \approx \frac{u(x+h) - u(x)}{h} \tag{4.1.1}$$

where the derivatives are included in the differential equation. Assuming that h is very

small and is approximated with an average rate of change, then we derive the equations of the function values $u(x)$, $u(x+h)$, and $u(x-h)$ at points x and $x\pm h$ near point x (these are usually called difference equations) and determine the approximate values by solving them.

As the finite-difference method can be differentiated using differential equations, it is simple and very easy to use. On the other hand, when differentiating these differential equations, it is difficult to solve the problems within the boundaries of arbitrary geometries in general, since the value of an unknown function is used only at lattice points. Recently, various calculation methods, such as the finite element method (FEM) and boundary element method (BEM), have been developed to eliminate this disadvantage, and the applications of finite-difference methods are being expanded further. Table 4.1.1 shows the comparisons of FDM, FEM and BEM.

Table 4.1.1 Comparison of numerical calculation methods

	FDM	FEM	BEM
Formulation	Differential approximate	Weak form	Integral equation
Discretization	Lattice points	Finite element	Boundary elements
Solution	Area type	Area type	Boundary type
Coefficient matrix	Sparse matrix	Sparse matrix	Not sparse matrix
Characteristic	·Discretization Easy ·Calculation Fast ·Scheme Stable and accuracy clear	·Arbitrary current ·Boundary conditions ·Automatic calculation	·Reduced dimensions to one dimension ·External and Internal problem are same ·Unknown is boundary differentiation

Approximation of partial differential quotient

When approximating the partial differentiation quotients $\frac{\partial u}{\partial x}, \frac{\partial u}{\partial y}, \frac{\partial^2 u}{\partial x^2}, \frac{\partial^2 u}{\partial x \partial y}, \frac{\partial^2 u}{\partial y^2}$ of functions of two variables $u(x,y)$ using forward differences, the equations can be expressed as the following equations:

$$\frac{\partial u}{\partial x} \cong \frac{\Delta_x u}{\Delta x} = \frac{u(x+\Delta x, y) - u(x,y)}{\Delta x} \tag{4.1.2}$$

$$\frac{\partial u}{\partial x} \cong \frac{\Delta_y u}{\Delta y} = \frac{u(x, y+\Delta y) - u(x,y)}{\Delta y} \tag{4.1.3}$$

$$\frac{\partial^2 u}{\partial x^2} \cong \frac{\Delta^2{}_x u}{\Delta x^2} = \frac{u(x+2\Delta x, y) - 2u(x+\Delta x, y) + u(x,y)}{\Delta x^2} \tag{4.1.4}$$

$$\frac{\partial^2 u}{\partial x \partial y} \cong \frac{\Delta_x}{\Delta x}\frac{\Delta^2{}_x u}{\Delta x^2}$$

$$= \left(\frac{u(x+\Delta x, y+\Delta y) - u(x+\Delta x, y)}{\Delta y} - \frac{u(x, y+\Delta y) - u(x,y)}{\Delta y}\right)\Big/_{\Delta x} \tag{4.1.5}$$

$$= \frac{u(x+\Delta x, y+\Delta y) - u(x+\Delta x, y) - u(x, y+\Delta y) - u(x,y)}{\Delta x \Delta y}$$

$$\frac{\partial^2 u}{\partial y^2} \cong \frac{\Delta_{y^2} u}{\Delta y^2} = \frac{u(x, y+2\Delta y) - 2u(x, y+\Delta y) + u(x,y)}{\Delta y^2} \tag{4.1.6}$$

and by using the central difference, the equations can be expressed as:

$$\frac{\partial u}{\partial x} \cong \frac{\delta_x u}{\delta x} = \frac{u(x+\Delta x, y) - u(x-\Delta x, y)}{2\Delta x} \tag{4.1.7}$$

$$\frac{\partial u}{\partial x} \cong \frac{\delta_y u}{\delta y} = \frac{u(x, y+\Delta y) - u(x, y-\Delta y)}{2\Delta y} \tag{4.1.8}$$

$$\frac{\partial^2 u}{\partial x^2} \cong \frac{\delta^2{}_x u}{\delta x^2} = \frac{u(x+\Delta x, y) - 2u(x,y) + u(x-\Delta x, y)}{\Delta x^2} \tag{4.1.9}$$

$$\frac{\partial^2 u}{\partial x \partial y} \cong \frac{\delta_x}{\delta x}\frac{\delta^2{}_x u}{\delta x^2}$$

$$= \{u(x+\Delta x, y+\Delta y) - u(x+\Delta x, y-\Delta y) \tag{4.1.10}$$

$$- u(x-\Delta x, y+\Delta y) + u(x-\Delta x, y-\Delta y)\}/\Delta x \Delta y$$

$$\frac{\partial^2 u}{\partial y^2} \cong \frac{\delta_{y^2} u}{\delta y^2} = \frac{u(x, y+\Delta y) - 2u(x,y) + u(x, y-\Delta y)}{\Delta y^2} \tag{4.1.11}$$

and then by using the backward differences, the equations can be expressed as:

$$\frac{\partial u}{\partial x} \cong \frac{u(x,y) - u(x-\Delta x, y)}{\Delta x} \tag{4.1.12}$$

$$\frac{\partial u}{\partial x} \cong \frac{u(x,y) - u(x, y-\Delta y)}{\Delta y} \tag{4.1.13}$$

Construction of difference equation

If we replace all of the partial differential quotients with the deviation quotient in the partial differential equation, an approximate difference equation can be constructed.

An approximate difference equation for partial differential equations can be expressed as:

$$\frac{\partial u}{\partial t} = \frac{\partial u}{\partial x} \tag{4.1.14}$$

The equation obtained by replacing each term with the front differential quotient can be expressed as:

$$\frac{u(t+\Delta t, x) - u(t,x)}{\Delta t} = \frac{u(t, x+\Delta x) - u(t,x)}{\Delta x} \tag{4.1.15}$$

Then, if each term in the equation is replaced by the central differential quotient, the equation can be expressed as:

$$\frac{u(t+\Delta t, x) - u(t-\Delta t, x)}{2\Delta t} = \frac{u(t, x+\Delta x) - u(t, x-\Delta x)}{2\Delta x} \tag{4.1.16}$$

Although various approximate difference equations can be created this way, the differential equations do not always result in valid approximations. For example, if $\frac{\partial u}{\partial t}$ and $\frac{\partial u}{\partial x}$ are approximated by a forward difference quotient and a backward difference quotient,

$$\frac{u(t+\Delta t, x) - u(t,x)}{\Delta t} = \frac{u(t,x) - u(t, x-\Delta x)}{\Delta x} \tag{4.1.17}$$

and, if $\frac{\partial u}{\partial t}$ and $\frac{\partial u}{\partial x}$ are approximated by a forward difference quotient and a central

difference quotient,

$$\frac{u(t+\Delta t,x)-u(t,x)}{\Delta t}=\frac{u(t,x+\Delta x)-u(t,x-\Delta x)}{\Delta x} \tag{4.1.18}$$

then, it is known that the equation (4.1.17) contradicts the nature of the original differential equation, and the equation (4.1.18) has a defect with regards to stability.

This is a functional equation drawn between the function value at one point and the value of a point near that point. This means that, to obtain a solution that can be established for all points on the area, it is necessary to set a distance to lattice points of *⊿x* in *x*-direction and *⊿y* in *y*-direction, so that the differential equations can be solved at the lattice using the simultaneous equations.

4.1.2 Finite Difference Expression of Laplace's Equation

We can explain the finite-difference methods using the Laplace's equation.The partial differential equation, also called the Laplace's equation, can be expressed as:

$$\frac{\partial^2 u}{\partial x^2}+\frac{\partial^2 u}{\delta y^2}=0 \tag{4.1.19}$$

and it has many important applications, such as in the calculation of electric fields, magnetic fields and temperature distribution. The original equation is three-dimensional, but for simplicity's sake, we will explain it as two-dimensional equation. The ancillary conditions can be any of the following: the first type of boundary condition "specify the value of *u* on the boundary", the second type of boundary condition "specify the value of the normal direction coefficient $\frac{\partial u}{\partial n}$ of *u* on the boundary", or a mixed type of boundary condition "type 1 at a part of the boundary, type 2 at the remaining part".

The equation of each term approximated by the central differential quotient can be expressed as:

$$\frac{u_{i+1,j} - 2u_{i,j} + u_{i-1,j}}{\Delta x^2} + \frac{u_{i,j+1} - 2u_{i,j} + u_{i,j-1}}{\Delta y^2} = 0 \qquad (4.1.20)$$

and if $\Delta x = \Delta y$, the following equation,

$$u_{i+1,j} + u_{i-1,j} + u_{i,j+1}u_{i,j-1} - 4u_{i,j} = 0 \qquad (4.1.21)$$

can be obtained.

To approximate the second type of boundary condition $\frac{\partial u}{\partial n} = \alpha$, temporary points outside of this area can be assumed (in Fig. 4.1.1), then, using the function value $u_{i+1,j}$,

$$\frac{u_{n+1,j} + u_{n-1,j}}{\Delta x} = \alpha \qquad (4.1.22)$$

can be obtained.

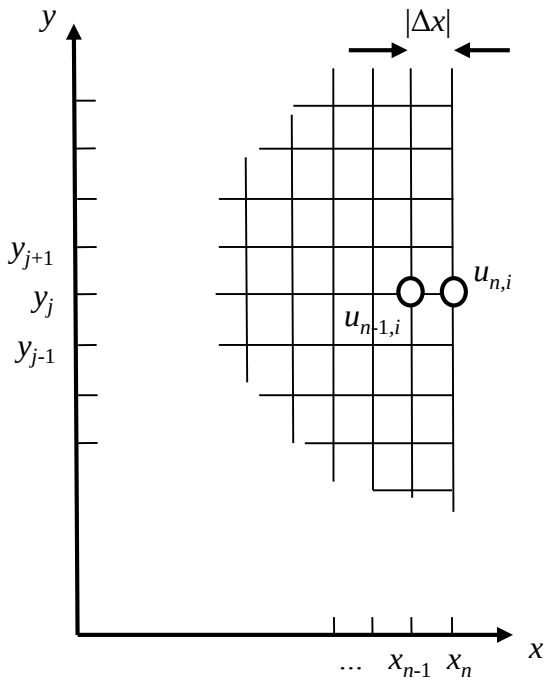

Fig 4.1.1 Boundary conditions.

and the equation corresponding to equation (4.1.20) can be expressed as:

$$u_{n+1,j} + u_{n-1,j} + u_{n,j+1} + u_{n,j-1} - 4u_{n,j} = 0 \qquad (4.1.23)$$

In combining equation (4.1.22) and (4.1.23) by deleting $u_{i+1,j}$, the equation at the boundary point can be simplified as:

$$2\alpha\Delta x + 2u_{n+1,j} + u_{n-1,j} + u_{n,j+1} - 4u_{n,j} = 0 \qquad (4.1.24)$$

When we solve these equations simultaneously, as there is a large number of variables, it is necessary to devise a method to improve computational efficiency using the special properties of the equation. Then, an iterative method (sequential substitution method) is often used to solve this problem. For example, in transforming the equation (4.1.21) into the following equation:

$$u_{i,j} = \frac{\left(u_{i+1,j} + u_{i-1,j} + u_{i,j+1} + u_{i,j-1}\right)}{4} \qquad (4.1.25)$$

and applying the sequential substitution method,

$$u_{i,j}{}^{(k+1)} =/ \frac{\left(u_{i+1,j}{}^{(k)} + u_{i-1,j}{}^{(k)} + u_{i,j+1}{}^{(k)} + u_{i,j-1}{}^{(k)}\right)}{4} \qquad (4.1.26)$$

can be obtained, where *k* means "*k*-th approximation". We can then repeat this for all *i* and *j* until the accuracy is satisfactory.

While iterative methods according to equation (4.1.25) have been proven to converge, the convergence speed is generally very slow, and increasingly so if the division is smaller. Therefore, to improve the convergence speed, one method of "modifying a little extra" is widely used. It is,

$$\begin{aligned} u_{i,j}{}^{(k+1)} = u_{i,j}{}^{(k)} & \\ + \omega \Bigg\{ & \frac{\left(u_{i+1,j}{}^{(k)} + u_{i-1,j}{}^{(k)} + u_{i,j+1}{}^{(k)} + u_{i,j-1}{}^{(k)}\right)}{4} \\ & - u_{i,j}{}^{(k)} \Bigg\} \end{aligned} \qquad (4.1.27)$$

where, ω is an acceleration factor (or a magnification of the correction amount). It can be modified by multiplying the correction amount calculated using equation (4.1.25) by ω.

Then, the approximate difference equation using Poisson's equation is created similarly to Laplace's equation. Once we add the value $f(x_i, y_j)$ of $f(x, y)$ at the lattice point as a non-homogeneous term on the right side of the equation (4.1.20), the following equation

$$\frac{u_{i+1,j} - 2u_{i,j} + u_{i-1,j}}{\Delta x^2} + \frac{u_{i,j+1} - 2u_{i,j} + u_{i,j-1}}{\Delta y^2} = f(x_i, y_i) \tag{4.1.28}$$

can be obtained. Especially, when $\Delta x = \Delta y$,

$$u_{i+1,j} + u_{i-1,j} + u_{i,j+1} + u_{i,j-1} - 4u_{i,j} = \Delta x^2 f(x_i, y_i) \tag{4.1.29}$$

can be obtained.

In addition, when the thermal conductivity or electrical conductivity varies depending on the places,

$$\frac{\partial}{\partial x}\left(a(x,y)\frac{\partial u}{\partial x}\right) + \frac{\partial}{\partial y}\left(a(x,y)\frac{\partial u}{\partial y}\right) = f(x,y) \tag{4.1.30}$$

can be obtained. In order to differentiate this, a lattice point can be provided at the discontinuous point of $a(x, y)$, as follows:

$$\begin{aligned} &\frac{\left\{a\left(x_i + \frac{\Delta x}{2}, y_j\right)\frac{u_{i+1,j} - u_{i,j}}{\Delta x} - a\left(x_i - \frac{\Delta x}{2}, y_j\right)\frac{u_{i,j} - u_{i-1,j}}{\Delta x}\right\}}{\Delta x} \\ &+ \frac{\left\{a\left(x_i, y_j + \frac{\Delta y}{2}\right)\frac{u_{i,j+1} - u_{i,j}}{\Delta x} - a\left(x_i, y_j - \frac{\Delta y}{2}\right)\frac{u_{i,j} - u_{i,j-1}}{\Delta x}\right\}}{\Delta x} = \alpha \end{aligned} \tag{4.1.31}$$

4.2 Analysis of HTS Magnetizations Process by Current Vector Potential Method (T-method)

4.2.1 Current Vector Potential Method

The current vector potential method, which is also called T-method, is a method of calculating an eddy current field. The eddy current can be expressed using the following equation:

$$\mathbf{J} = \nabla \times \mathbf{T} \tag{4.2.1}$$

for ensuring it satisfies the continuous equation by

$$\nabla \cdot \mathbf{J} = 0 \tag{4.2.2}$$

where, the **T** is called vector potential of **J**.

Compared to other eddy current analysis methods, the advantage of using the potential **T** is that the analysis region of the T-method is limited to the inside of the conductor, which can be extremely small.

We will now introduce the integro-differential equation of T-method.

Firstly, Ohm's law can be expressed as:

$$\mathbf{J} = \sigma \mathbf{E} \tag{3.1.7}$$

then, taking the rotation of equation (3.1.32), the following equation can be expressed using the current vector potential that is defined by equation (3.1.30) (Faraday's law of induction) and (4.2.1):

$$\nabla \times \frac{1}{\sigma} \nabla \times \mathbf{T} = -\frac{\partial \mathbf{B}}{\partial t} \tag{4.2.3}$$

The magnetic flux density **B** can be expressed as

$$\boldsymbol{B} = \boldsymbol{B}_0 + \boldsymbol{B}_e \tag{4.2.4}$$

where, $\mathbf{B}_0$ is the external magnetic field applied to the conductor, and $\mathbf{B}_e$ is the magnetic field produced by the eddy current.

$\mathbf{B}_e$ can be expressed as the following equation by using the Bio-Savart law and the current vector potential equation:

$$\mathbf{B}_e = \frac{\mu_0}{4\pi}\int_{V'} \nabla \times \mathbf{T} \times \nabla' \frac{1}{R} dV' \tag{4.2.5}$$

then, by using the Helmholtz decomposition, the equation can be expressed as

$$T = \frac{1}{4\pi}\left\{\int_V \nabla \times \mathbf{T} \times \boldsymbol{\nabla} \frac{1}{R} d\nabla + \int_V (\nabla \cdot \mathbf{T}) \nabla \frac{1}{R} dV - \int_S (\mathbf{n} \times \mathbf{T}) \times \nabla \frac{1}{R} dS - \int_S (\mathbf{n} \cdot \mathbf{T}) \nabla \frac{1}{R} dS\right\} \tag{4.2.6}$$

And the Coulomb gauge and the boundary conditions of currents that do not flow out of the surface of the conductor can be expressed as the following equation:

$$\nabla \cdot \mathbf{T} = 0 \quad \text{in} \quad V \tag{4.2.7}$$

$$\mathbf{n} \times \mathbf{T} = 0 \quad \text{on} \quad S \tag{4.2.8}$$

By using the equation (4.2.7) and (4.2.8), the second and third terms of (4.2.6) can be eliminated, and then, $\mathbf{B}_e$ can be expressed as the following equation:

$$\mathbf{B}_e = \frac{\mu_0}{4\pi}\int_V \nabla \times \mathbf{T} \times \nabla \frac{1}{R} dV = \mu_0 T + \frac{\mu_0}{4\pi}\int_S T \nabla \frac{1}{R} dS \tag{4.2.9}$$

Combined with equations (4.2.4) and (4.2.9), equation (4.2.3) can be expressed in the following manner:

$$\nabla \times \frac{1}{\sigma} \nabla \times \mathbf{T} + \mu_0 \frac{\partial \mathbf{T}}{\partial t} + \frac{\mu_0}{4\pi}\int_S \frac{\partial T_n}{\partial t} \nabla' \frac{1}{R} dS' + \frac{\partial \mathbf{B}_0}{\partial t} = 0 \tag{4.2.10}$$

where, T_n is a vertical component vector on the surface of the conductor. Then, using the next equation:

$$\nabla \times \nabla \times \mathbf{A} = \nabla(\nabla \cdot \mathbf{A}) - \nabla^2 \mathbf{A} \tag{4.2.11}$$

The governing equation of the T-method can be expressed as the following:

$$\frac{1}{\sigma}\nabla^2\mathbf{T} - \mu_0\frac{\partial \mathbf{T}}{\partial t} - \frac{\mu_0}{4\pi}\int_S \frac{\partial T_n}{\partial t}\nabla'\frac{1}{R}dS' = \frac{\partial \mathbf{B}_0}{\partial t} \qquad (4.2.12)$$

In equation (4.2.12), the third term on the left side is the surface integral of the analysis region. When we solve equation (4.2.12) numerically, the matrix becomes asymmetrical and partially dense due to the surface integral. However, the calculation cost of the T-method is quite large, even the analytical region is very small and the unknowns are fewer than in other analysis methods (Fig. 4.2.1).

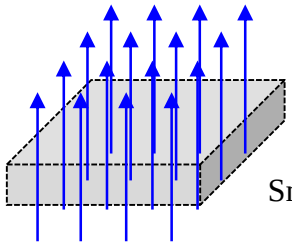

Small dense matrix

Unknown region (T-method)

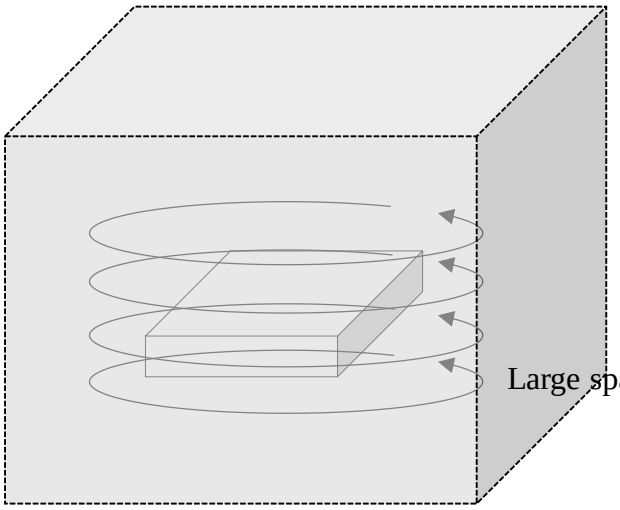

Large sparse matrix

Unknown region (A-∅ method)

Fig. 4.2.1 Comparison of the analysis region.

4.2.2 Two-dimensional Thin Plate Approximation

An induced current can be generated if a variable magnetic field is applied to the conductor. However, neither the eddy currents concentrated on the surface of the

conductor nor the magnetic field can penetrate into the inside of the conductor. This well-known phenomenon is called the skin effect. The skin depth δ in the AC problem is:

$$\delta = \sqrt{\frac{2}{\sigma\mu\omega}} \tag{4.2.13}$$

where, σ is conductivity, μ is permeability and ω is angular frequency. This skin depth represents the extent of the magnetic field's penetration, and conversely, it shows the degree of penetration of the eddy current. The magnetic field and eddy current at distance z from the surface of the conductor can be expressed using the following equation:

$$\begin{aligned} B &= B_0 exp(-z/\delta) \\ J &= J_0 exp(-z/\delta) \end{aligned} \tag{4.2.14}$$

Since the ω corresponds to the speed of the magnetic field's change, we can approximate that currents are uniformly distributed in the thickness direction of the conductor, when the change of the magnetic field is very slow or the conductor is thin enough. Then, the direction of the current is confined within a plane perpendicular to the thickness direction.

Fig. 4.2.2 shows a thin plate of conductive material. The above-mentioned conditions can be expressed through the following equations:

$$\frac{\partial J_x}{\partial z} = 0, \tag{4.2.15}$$

$$\frac{\partial J_y}{\partial z} = 0 \tag{4.2.16}$$

$$J_z = 0 \tag{4.2.17}$$

Under these conditions, the current vector potential **T** only exists in z-direction, which is perpendicular to the plate, so $T_x = T_y = 0$. In addition, it is assumed that the vertical component T_z is constant, so we can denote this vertical component as T. Then, the relationship between the eddy current density and T can be expressed as the following

equation:

$$\mathbf{J} = \nabla \times (\mathbf{n}T) = \nabla \mathrm{T} \times \mathbf{n} \tag{4.2.18}$$

and the *x*, *y*, *z*-component can be expressed as:

$$J_x = \frac{\partial T}{\partial y} \tag{4.2.19}$$

$$J_y = \frac{\partial T}{\partial x} \tag{4.2.20}$$

$$J_z = 0 \tag{4.2.21}$$

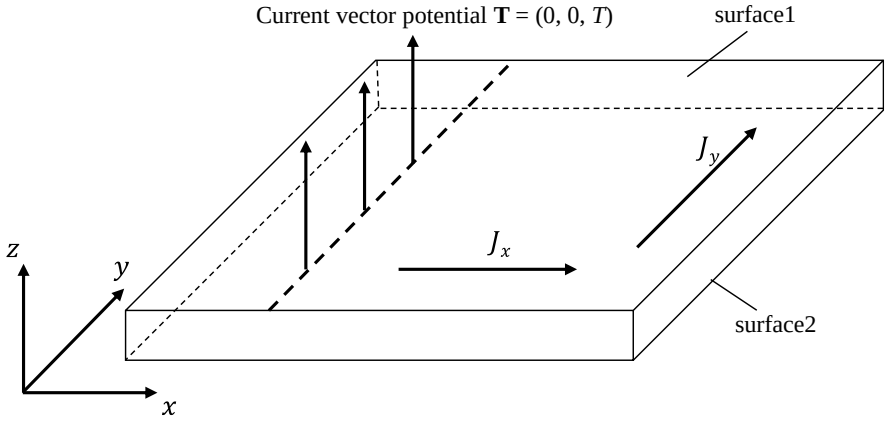

Fig. 4.2.2 Overview of current vector potential method.

The scalar function T is a flow function of a two-dimensional flow field (J_x, J_y).

We will now discuss the gauge condition and boundary condition of the current vector potential (0, 0, T). Firstly, the gauge condition can be naturally satisfied by the following equation:

$$\nabla \cdot \mathbf{T} = \nabla \cdot (\mathbf{n}\mathrm{T}) = \frac{\partial T}{\partial z} = 0 \tag{4.2.22}$$

Fig. 4.2.2 shows a thin plate of conductive material, for which the vector potential component is 0 on surfaces 1 and 2, which are parallel to the *z*-axis. As such, the boundary condition can be expressed as the following equation:

$$T = 0 \tag{4.2.23}$$

Therefore, the boundary only has a *z*-component and no *x* and *y*-component. The

governing equation can be expressed as:

$$\nabla \times \frac{1}{\sigma}\nabla \times \mathbf{T} - \mu_0 \frac{\partial \mathbf{T}}{\partial t} - \frac{\mu_0}{4\pi}\int_S \frac{\partial T_n}{\partial t}\nabla' \frac{1}{r} dS' = \frac{\partial B_{z0}}{\partial t} \tag{4.2.24}$$

Using the scalar function T, the number of variables can be reduced significantly, which simplifies numerical simulations.

In addition, even if the thickness of the conductor plate is larger than the skin depth, a thin plate approximation can be applied if the *z*-component of currents can be ignored. At this moment, the currents only flow in the *x*-*y* direction, and the *z*-component of the currents do not exist. With these considerations, we believe that the conductor plate is composed of thin plates, as shown in Fig. 4.2.3.

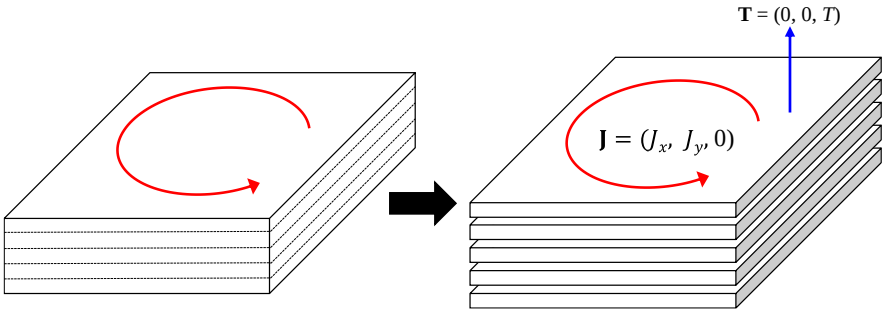

Fig. 4.2.3 Thin plate multi-layers modeling.

4.2.3 Bean's Critical State Model

Bean's critical state model, introduced by C. P. Bean [55]-[56], provides a macroscopic explanation of the irreversible magnetization behavior of type-II superconductors.

When the Lorentz force, which is applied to the magnetic flux captured at the center of flux pinning, becomes stronger than the flux pinning force, the magnetic flux jumps out from the center of flux pinning and is caught by the others, and a new magnetic flux distribution is formed. When the Lorentz force received from magnetic flux and the flux pinning force are in balance, the critical state is achieved. Then, the macro model that can

be established under this quasi-static equilibrium is called Bean's critical state model. This means that macroscopic currents can flow until the Lorentz force and the flux pinning force are in balance. Therefore, where currents are flowing, the Lorentz force and the flux pinning force are always in balance.

We will now discuss a mathematical model that is based on the Bean's critical state model. The state in which the Lorentz force and the flux pinning force are in balance can be expressed as:

$$\mathbf{J} \times \mathbf{B} - \mathbf{F}_p \frac{\mathbf{v}}{|\mathbf{v}|} = 0 \tag{4.2.25}$$

where, **v** is the speed of the magnetic flux quantum, and **v** is not the speed of the individual magnetic flux quantum, but rather the macroscopic estimate of average speed. The flux pinning force always acts in the direction hindering the movement of the magnetic flux quantum.

Let us assume that the current $\mathbf{J}$ and the magnetic field **B** are orthogonal to each other. It is easy to deduce that **v** is orthogonal to $\mathbf{J}$ and **B** from the equation (4.2.25). Therefore, the electric field induced in the superconductor by the motion of the magnetic flux quantum can be expressed as:

$$\mathbf{E} = \mathbf{B} \times \mathbf{v} \tag{4.2.26}$$

and it has the same direction as $\mathbf{J}$. From equations (4.2.25) and (4.2.26),

$$\mathbf{B} \times (\mathbf{J} \times \mathbf{B}) - \mathbf{F}_p \frac{\mathbf{E}}{|\mathbf{v}|} = 0 \tag{4.2.27}$$

can be obtained, and the first term of equation (4.2.27) can be transformed using this vector equation:

$$\mathbf{B} \times (\mathbf{J} \times \mathbf{B}) = \mathbf{J}(\mathbf{B} \cdot \mathbf{B}) - \mathbf{B}(\mathbf{B} \cdot \mathbf{J}) \tag{4.2.28}$$

and because $\boldsymbol{J} \perp \boldsymbol{B}$, then $\boldsymbol{B} \cdot \boldsymbol{J} = 0$, and the following equation:

$$\boldsymbol{J} = F_p \frac{\boldsymbol{E}}{|\boldsymbol{B}|^2 |\boldsymbol{v}|} \tag{4.2.29}$$

can be obtained. Furthermore, since **v**, **B**, **E** are orthogonal to each other, |**E**| = |**B**||**v**| can be established. By using these, equation (4.2.29) can be expressed using the following equation:

$$\mathbf{J}_{sc} = J_c(|\mathbf{B}|) \frac{\mathbf{E}}{|\mathbf{E}|} \qquad \text{if } |\mathbf{E}| \neq 0 \tag{4.2.30}$$

However,

$$J_c = \frac{F_p}{|\mathbf{B}|} \tag{4.2.31}$$

is the critical current density. Equation (4.2.31) is a definition of a very rational critical current density in which the Lorentz force F_p and the flux pinning force $J_c|\mathbf{B}|$ are in balance.

Let us consider the constitutive equation with |**E**| = 0. This can be established when **B** = 0 or **v** = 0. Under the condition that **B** = 0, since there are no shielding currents, the macroscopic currents also do not exist. On the other hand, under the condition **v** = 0, the magnetic flux quantum can be constant, and although the shielding currents are not 0, they do not change over time. Therefore, the following equation:

$$\frac{\partial \mathbf{J}_{sc}}{\partial t} = 0 \qquad \text{if } |\mathbf{E}| = 0 \tag{4.2.32}$$

can be obtained. The equations (4.2.30) and (4.2.32) constitute the mathematical model corresponding to the Bean's critical state model. When the constitutive law can be defined by $\sigma = |\mathbf{J}|/|\mathbf{E}|$ according to Ohm's law, σ also can be expressed as the following equation:

$$\sigma = \frac{J_c(|\mathbf{B}|)}{|\mathbf{E}|} \qquad \text{if } |\mathbf{E}| \neq 0 \tag{4.2.33}$$

$$\sigma = \infty \qquad \text{if } |\mathbf{E}| = 0 \tag{4.2.34}$$

It is known that the critical current density J_c depends on the magnetic field, and various proposal have been made to express the magnetic field dependence of J_c. In this study, we use Bean's critical model, where J_c is constant, as the flux pinning force is proportional to the magnetic field and J_c is not dependent on the magnetic field. Then, the equation can be expressed as follows:

$$J_c = \text{const.} \tag{4.2.35}$$

Since this model is simple, it is often used for superconductivity based on Bean's critical state model.

Artificial conductivity method

As equation (4.2.24) is obtained using Ohm's law (3.1.7), the constitutive equation cannot be established by using equation (4.2.30) and (4.2.32). We will therefore introduce a method for calculating the shielding current that satisfies equations (4.2.30) and (4.2.32), and Maxwell's equations.

Firstly, we will assume that the superconductor is a very good conductor and set the value of conductivity σ to a very large value (in our research, $\sigma = 10^{13}$[1/Ωm]). Then, we will find the T by solving the governing equation (4.2.24). The equations can be solved using T and $\mathbf{J} = \nabla \mathrm{T} \times \mathbf{n}$. The equations can be expressed as follows:

$$\sigma_{\text{new}} = \sigma_{\text{old}} \frac{J_c}{|\mathbf{J}|} \quad (|\mathbf{J}| > J_c) \tag{4.2.36}$$

$$\sigma_{\text{new}} = \sigma_{\text{old}} \quad (|\mathbf{J}| \leq J_c) \tag{4.2.37}$$

where, σ_{new} and σ_{old} are conductivity, $|\mathbf{J}|$ is shielding current density and J_c is the critical current density. This means if the value of shielding current density is larger than the critical current density, we must replace the old conductivity σ_{old} with a small value

(σ_{new}). If the value of shielding current density is equal to or smaller than the critical current density, then the value of conductivity σ_{old} does not change until the value of shielding current density is equal to or smaller than the critical current density in the entire region. By using this method, the governing equation can be solved again, and the value of shielding current density can be found. The above instructions must be followed until the shielding current density converges (Fig. 4.2.5).

Although there is only one condition in which the shielding current density is smaller than critical current density, it is approximate to the Bean's critical state model in which the initial conductivity is very large. In Bean's critical state model, the region is divided between where shielding currents (equal to J_c) are flowing and shielding currents are not flowing. Then, in numerical calculations, the conductivity will not change in the region where the shielding current density is smaller than J_c, so it is necessary to set a very large value for conductivity. In a situation including a perfect conductor with $\sigma \to \infty$, the electric field cannot enter the perfect conductor. In other words, in a region with a very large conductivity, the electric field is very small, and the shielding current density that is generated according to Ohm's law also is also very small. In Bean's critical state model, this corresponds to the region where shielding currents are not flowing at all. In addition, conductivity will gradually decrease in the region where the shielding current density is larger than J_c, and is asymptotic to J_c. Although the shielding currents flow at the regions' boundaries, they still satisfy Bean's critical state model because space is discretized in numerical calculations.

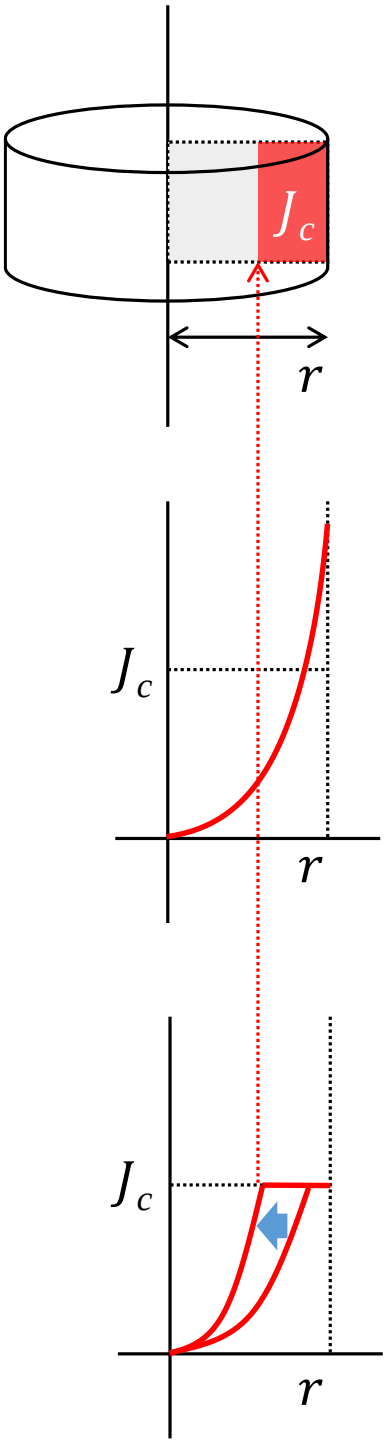

Fig. 4.2.4 Shielding current distribution restricted in finite value J_c.

4.2.4 Power-law Macro-model

The power-law, which is found in natural and social phenomena, is a functional relationship between two quantities, wherein a relative change in one quantity causes in a proportional relative change in the other quantity, irrespective of the initial size of those quantities, so that one quantity varies as the power of another. For example, if there are two quantities *x* and *y*, the power-law can be expressed as the following equation:

$$y = bx^a \tag{4.2.38}$$

Since the J_c in the HTS magnets has a very strong anisotropy, we believe that the HTS magnets were composed of *M*-sheets of thin layers (Chapter 4.2.2). In the *n*-th layer, the relationship between the electric field E_n and the shielding current density $\mathbf{J}_n$ can be expressed through J-E constitutive relationships, which are expressed through the following equations:

$$\mathbf{E}_n = E\left(|\mathbf{J}_n|\right)\left(\frac{\mathbf{J}_n}{|\mathbf{J}_n|}\right) \tag{4.2.39}$$

$$E(J) = E_C\left(\frac{J}{J_c}\right)^N \tag{4.2.40}$$

where, E_C is the critical electric field, and N is a nonlinear strength (constant). The combination of equations (4.2.39) and (4.2.40), or the power-law macro-model, can be expressed as [11]-[14]:

$$\mathbf{E} = E_C\left(\frac{J}{J_c}\right)^N \frac{\mathbf{J}_c}{|\mathbf{J}_c|} \tag{4.2.41}$$

Since these equations reflect the relationship between the electric field and the shielding current density, and this method is widely used in high-Tc superconductivity calculations, the behavior of the shielding current density in HTS magnets can be described more properly by using the power-law macro-model than by using the simple model (Bean's critical state model).

4.3 Runge-Kutta Method

The Runge–Kutta method is a set of implicit and explicit iterative methods used for temporal discretization in numerical simulations. These are calculated using the approximate solutions of ordinary differential equations developed the German mathematicians C. Runge and M. W. Kutta. The method is usually called “RK4” or “the Runge-Kutta method”

For example, an initial problem is expressed as follows:

$$y' = f(x, y), \qquad y(x_0) = y_0 \tag{4.3.1}$$

Then, RK4’s differential equations (the Runge-Kutta method) can be expressed as follows:

$$y_{n+1} = y_n + \frac{h_n}{6}(k_1 + 2k_2 + 2k_3 + k_4) \qquad (n = 0,1,2\cdots) \tag{4.3.2}$$

where,

$$k_1 = f(x_n, y_n) \tag{4.3.3}$$

$$k_2 = f\left(x_n + \frac{h_n}{2}, y_n + \frac{1}{2}k_1 h_n\right) \tag{4.3.4}$$

$$k_3 = f\left(x_n + \frac{h_n}{2}, y_n + \frac{1}{2}k_2 h_n\right) \tag{4.3.5}$$

$$k_4 = f(x_n + h_n, y_n + k_3 h_n) \tag{4.3.6}$$

where, the geometric meaning of each k_i(i = 1, 2, 3, 4), is the slope of the tangent line of the solution curve l_i(i = 1, 2, 3, 4) of the differential equation $\frac{dy}{dx} = f(x, y)$, which passes through each point of P_i(i = 1, 2, 3, 4) in Fig. 4.3.1.

In our numerical simulation code, we used the Runge-Kutta method to estimate the electron trajectory using the magnetic field distribution of HTS magnets.

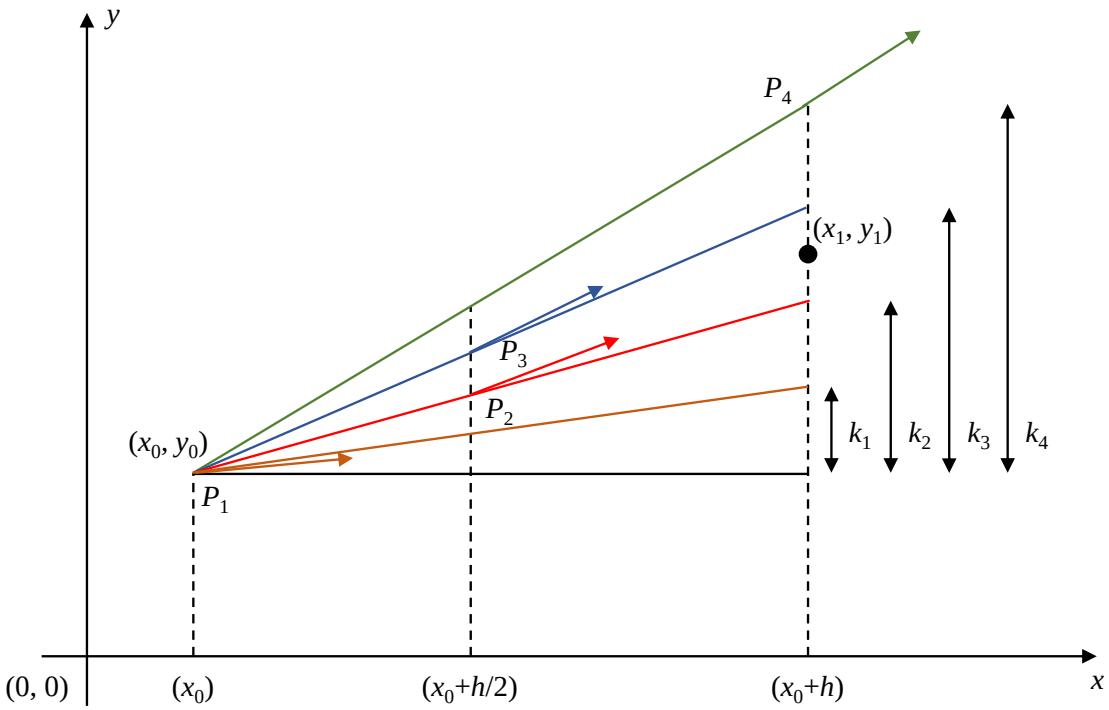

Fig. 4.3.1 Runge-Kutta method.

Chapter 5

Simulation of the Magnetization Process of HTS Undulators

In this Chapter, we will introduce the simulation of HTS undulators' magnetization process based upon Chapter 3's Fundamental theories and Chapter 4's Formulations.

5.1 Numerical Scheme of Magnetization Process

In Chapter 4.2, we discussed the analysis of HTSs by using the T-method. In general, since the shielding currents flow exclusively in the horizontal plane of the bulk HTSs, assuming the presence of the HTSs two-dimensional thin plate approximation, the equation (4.2.13) is solved as a two-dimensional problem. In this case, assume that the currents only exist in *x*-*y* direction, and only one unknown (T) in *z*-direction needs to be calculated. In addition, HTS magnets' magnetization process can be determined by the Bean's critical state model (Chapter 4.2.3) [6]-[9]. The power-law macro-model is another appropriate research tool (Chapter 4.2.4) [11]-[14]. Ultimately, this indicates that the shielding currents invade the interior from the surface by temporal change. The only unknown in T-method is J_{SC}, which serves as part of the simulation until a steady state is established in the time domain. Fig. 5.1.1 shows a flow chart regarding the analysis of pure-type HTS undulator magnetization processes. In particular, the innermost iteration is T-method calculation of shielding current for single HTS and adjustment of the conductivity distribution based on the macro-model (Bean's critical state model: equation

(4.2.36) and (4.2.37) power-law macro-model: equation (4.2.41)) in actual calculation, which is carried out for all superconductors at each time step. Then, interactions between the superconductors—influences of magnetic fields produced by other superconductors—are also taken into account as external magnetic fields. When converged distribution of conductivity distribution is obtained in this iteration, the program proceeds to the next time step. After all time step calculations are finished, the electron motion under the obtained undulator magnetic field is also simulated by using the Runge-Kutta method (in Chapter 4.3).

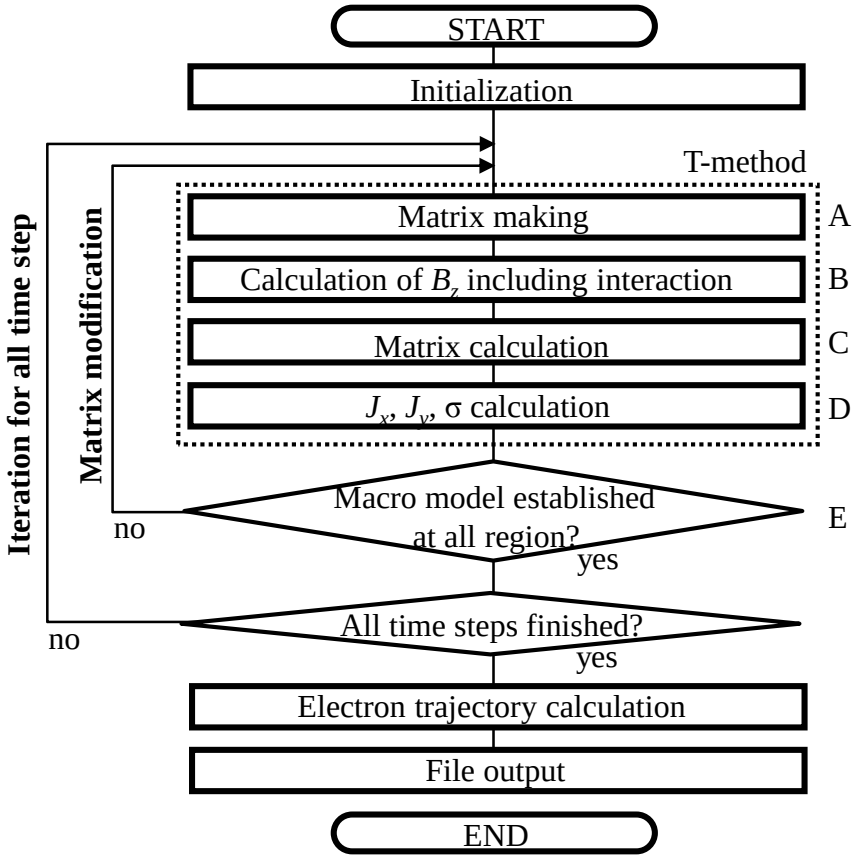

Fig. 5.1.1 Calculation flowchart of magnetization process based on T-method.

The following is a brief introduction of the pure-type HTS undulator's magnetization process:

The initial value of applied magnetic field reduced from B_{max} = 2.0 T to B_{min} = -0.6 T

during 13.0 s, which means that the external magnetic fields impose $\partial B_z/\partial_t$ = -0.2 [T/sec] in the inhomogeneous term of equation (4.2.12). Fig. 5.1.2 shows a simple example of the pure-type HTS undulator's magnetization process when the external magnetic field is gradually reduced by the temporal change (shown in Fig. 2.3.5). This means that the shielding currents are generated by reducing the external magnetic field.

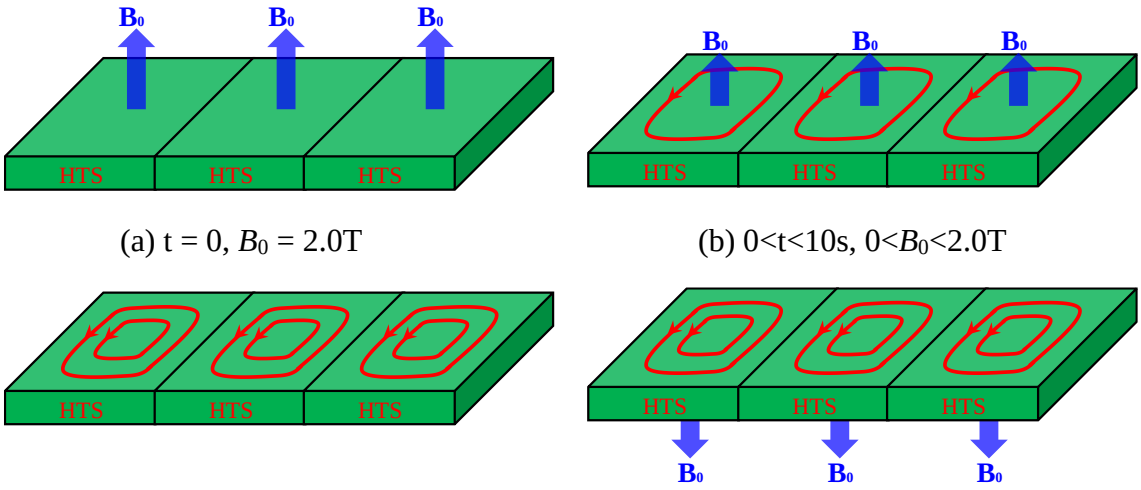

(a) t = 0, B_0 = 2.0T (b) 0<t<10s, 0<B_0<2.0T

(c) t = 10s, B_0 = 0 (d) t=13s, B_0 = -0.6T

Fig. 5.1.2 Magnetization process of the pure-type HTS undulator.

At the final stage of the magnetization process, the distributions of potential T's *z*-component are shown in Fig. 5.1.3. Similarly, the shielding current distributions are shown in 5.1.4, and a vertical distribution of the magnetic field beyond the HTS magnets—which is calculated by the induced shielding currents—is shown in Fig. 5.1.5.

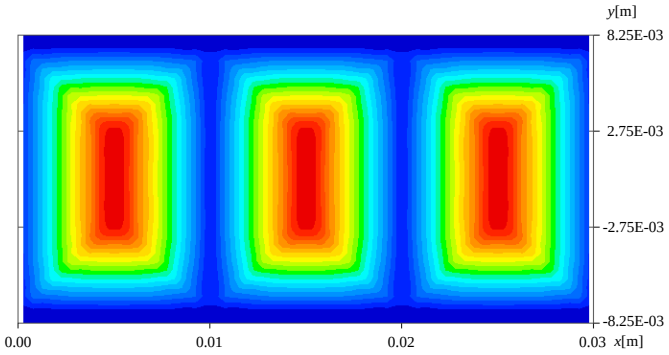

Fig. 5.1.3 Distribution of current potential of pure-type HTS undulator.

From Fig. 5.1.4, we can observe that the shielding currents penetrate deep into each HTS. Fig. 5.1.6 shows the sinusoidal distribution of the magnetic field's vertical component at 1mm above the HTSs. Here, we can observe that an alternative vertical magnetic field is generated along the longitudinal direction.

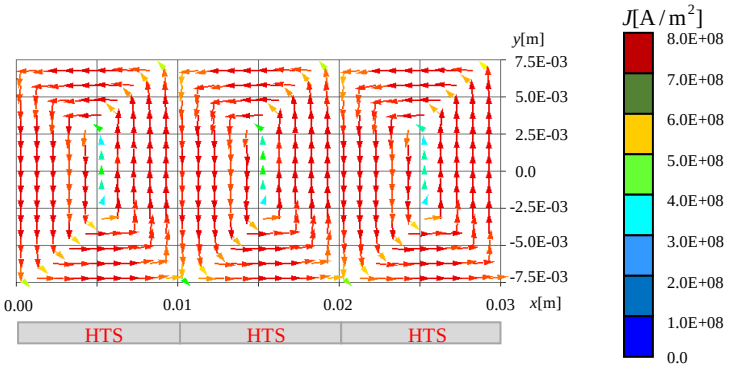

Fig. 5.1.4 Shielding current distributions on HTS.

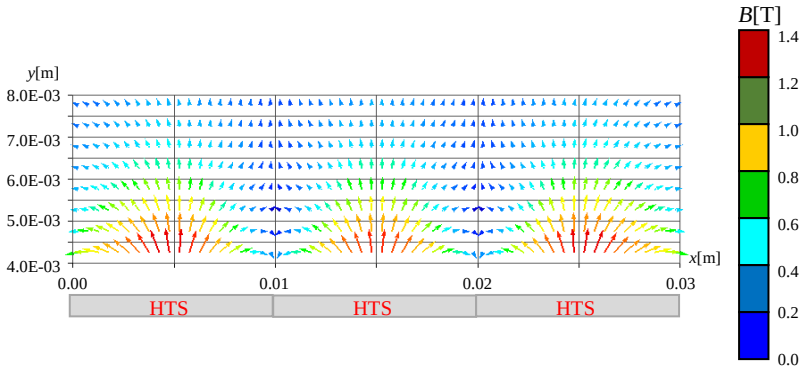

Fig. 5.1.5 Magnetic field distributions in vertical direction beyond the HTS.

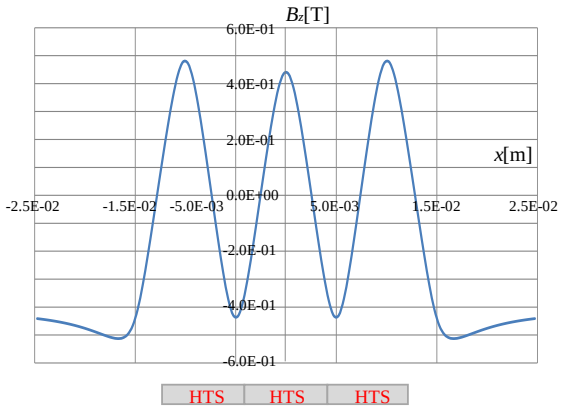

Fig. 5.1.6 Distribution of vertical component magnetic field beyond the HTS.

5.2 Comparison between Simulation Result and Experimental Measurement

Figs. 5.2.1 (a), (b), and (c) show the plots of the vertical magnetic field components along the *x*-direction at 1mm above the HTS magnets at the moments of B_0 = 1.8, 1.6, 1.4, 1.0, 0.6, 0.2, -0.4, -0.6 T by using the Bean's critical state model. The value of the critical current in the experiment is $J_c = 1.0\times10^9$ [A/m^2] (Fig. 5.2.1 (a)) [2]. From Fig. 5.2.1, we can confirm that the developed numerical code (by using the Bean's critical state model) is able to sufficiently simulate the pure-type HTS undulator's magnetization process under the condition of using a typical value of $J_c = 7.0\times10^8$ [A/m^2] (Fig. 5.2.1 (c)) [15]. This developed numerical code cannot simulate the magnetization process of the pure-type HTS undulator sufficiently by using the same critical current $J_c = 1.0\times10^9$ [A/m^2] as shown in Fig. 5.2.1 [b]. This means that the numerical code cannot simulate the magnetization process sufficiently by using the simple model, such as Bean's critical state model.

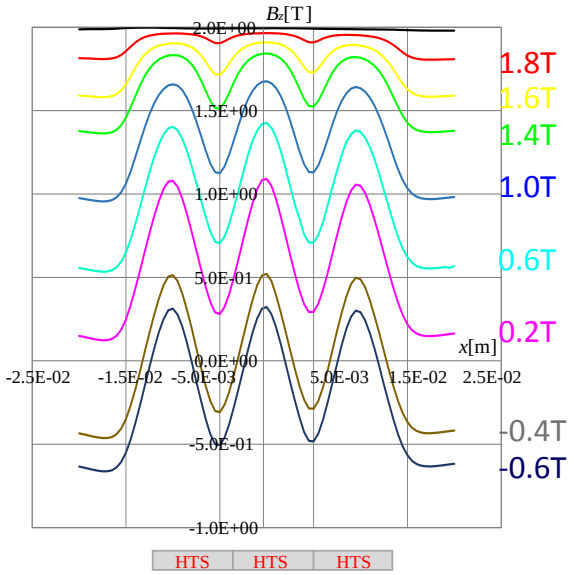

(a) Experimental measurement ($J_c = 1.0\times10^9$ [A/m^2])

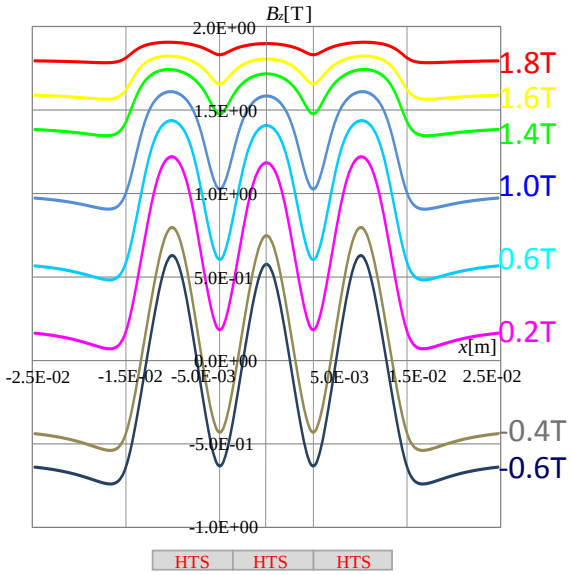

(b) Bean's critical state model (J_c = 1.0×10^9 [A/m^2])

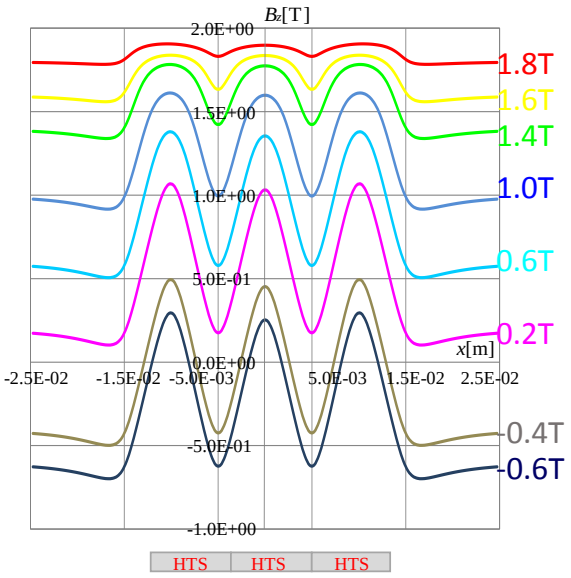

(c) Bean's critical state model (J_c = 7.0×10^8 [A/m^2])

Fig. 5.2.1 Magnetic field distribution beyond the HTSs in magnetization process.

To simulate the magnetization process of the pure-type HTS undulator, using the same critical current value as the experiment, the power-law macro-model is proposed in Chapter 4.2.4, since the electric field is closely related to the shielding current density. However, since the equation (4.2.41) is nonlinear, it cannot be used directly for calculating the equation (4.2.12). It is necessary to set an appropriate initial value of T,

and use the Newton's method to find the T that satisfies both (4.2.41) and (4.2.12) for each time step (E in Fig. 5.2.5).

Fig. 5.2.2 shows the plots of the vertical magnetic field component along the *x*-direction at 1 mm above the HTS magnets. The plots appear at the moments of B_0 = 1.8, 1.6, 1.4, 1.0, 0.6, 0.2, -0.4, -0.6 T by using the power-law macro-model under the condition of N = 20 and E_C = 1.0e^{-1} [V/m]. By comparing this to the experimental measurement (Fig. 5.2.1 [a]), we can confirm that the developed numerical code (by using the power-law macro-model) can simulate the magnetization process of the pure-type HTS undulator sufficiently by using the same critical current value as the experiment of J_c = 1.0×10^9 [A/m^2] [16].

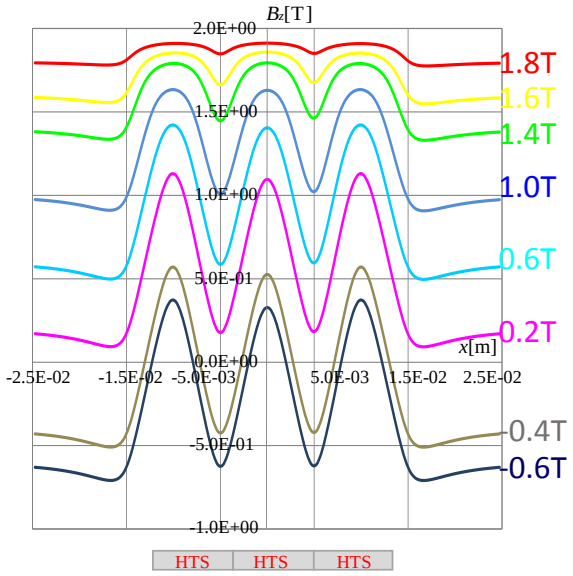

Fig. 5.2.2 Magnetic field distribution beyond the HTSs in magnetization process by using the power law conductivity model (J_c = 1.0×10^9 [A/m^2]).

However, the simulation time by using the power-law macro-model is about ten times shorter than using the Bean's critical state model (Table 5.2.1). Furthermore, since there are more than 200 HTS magnets in one FEL undulator machine [5], the calculation time by using the power-law macro-model is approximately two years, in the case of 280 HTS

magnets. Therefore, it is essential to shorten the calculation time.

Table. 5.2.1 Comparison of calculation time (Core i7 PC)

HTS number / Macro model	3 magnets	20 magnets	280 magnets
Bean’s critical state model	20min	8h	70 days
Power-law Macro-model	3h20min	70h	About 2 years

5.3 Acceleration for Large-scale Simulation

For reducing the calculation time, we use the following four methods (by using the Core i7 PC):

(1) Reduce the Calculation of Interactions between the HTS Magnets [17]

The developed numerical code, which considered the interactions of other HTS magnets, as introduced in Chapter 5.1, is shown in Fig. 5.3.1. It was found that approximately 50% of the calculation time is occupied by the calculation of the externally applied magnetic field. These external magnetic fields are generated by the shielding currents in the other HTS magnets ($B_z(\mathbf{r})$: B in Fig. 5.1.1 and the right term in equation (4.2.12)). Therefore, it is necessary to reduce the calculation time of interactions between the HTS magnets.

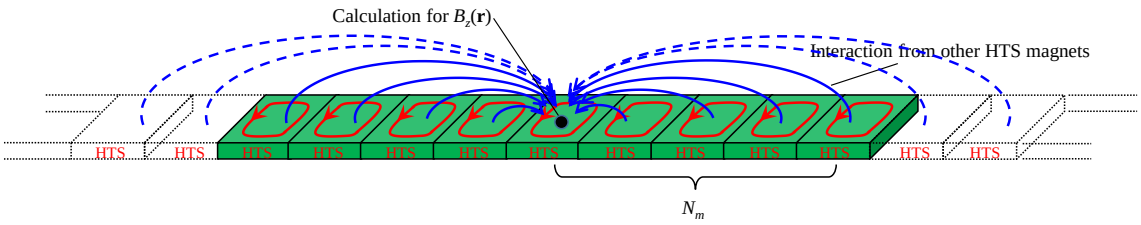

Fig. 5.3.1 Interactions from the N_m HTS magnets to be considered.

Figs. 5.3.2 (a), (b), and (c), show the distributions of the magnetic field B_z's vertical component, observed in the middle HTS magnet produced by the other 1, 3, 100 HTS

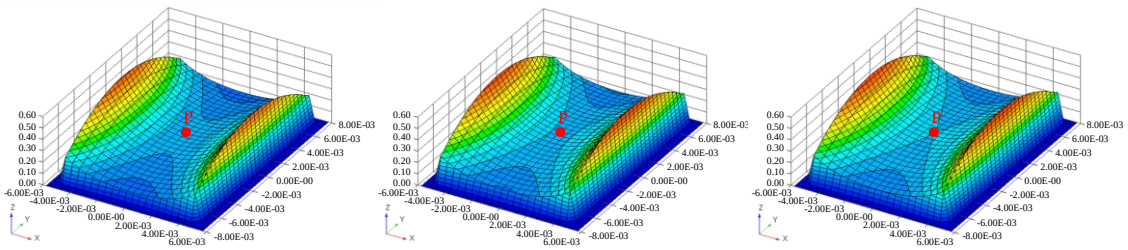

(a) N_m = 1 (b) N_m = 3 (c) N_m = 100

Fig. 5.3.2 Magnetic field distribution in HTS.

magnets. Additionally, Fig. 5.3.3 shows the value of B_z at the center point (point P) of the HTS magnet in Fig. 5.3.2. Therefore, taking the interactions from only the nearest 5 HTS magnets into account is sufficient.

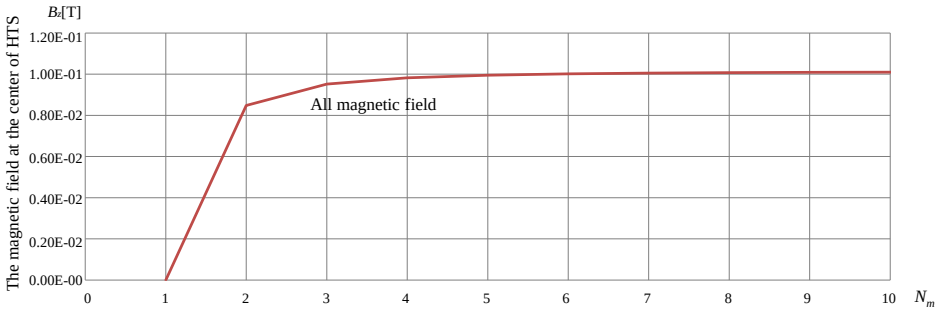

Fig. 5.3.3 Dependence of B_z on the number (N_m) of considered HTS magnets.

Fig. 5.3.4 shows the magnetic field distribution beyond 1mm from 10 HTS magnets along the x-direction in Fig. 5.2.3 at the final stage of the magnetization process when N_m = 0, 1, 2, 3, 4, 5, and 10 (all HTSs). From Fig. 5.3.3, the distributions are almost overlapped when N_m = 1, 2, 3, 4 and 5. Then, the relative error ε_m, which means the relative error compared with the full consideration of the other HTS magnets, is shown in Table 5.3.1. In general, it is necessary to achieve a uniform sinusoidal distribution of the vertical magnetic field component (suppressed within 1%) along a longitudinal direction (y-direction) of the FEL undulator for maintaining an operational laser.

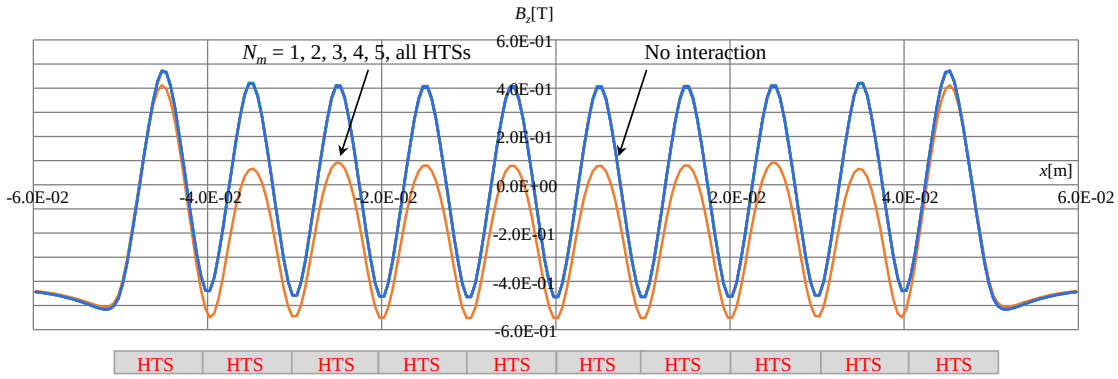

Fig. 5.3.4 Distribution of vertical magnetic component beyond 10 HTSs.

Accordingly, N_m = 3 is sufficient when considering the interactions between HTSs in

the final magnetic field distribution after the final distribution. However, the calculation time for the magnetization process is still approximately 50 hours (Bean's critical state model) for 100 HTSs (Fig. 5.3.5), even when the calculation of the interactions between HTS magnets is reduced to N_m = 3.

Table. 5.3.1 Relative error

N_m	ε_m (%)
1	1.48
2	0.33
3	0.12
4	0.07
5	0.05

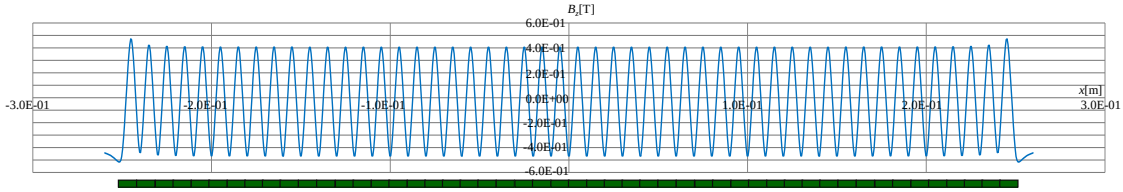

Fig. 5.3.5 Distribution of vertical magnetic field component (100 HTS magnets).

It is necessary to find other methods that further reduce the calculation time of the developed numerical code.

(2) Reduce the Calculation Time by Using Multipole Expansion [17]

Multipole expansion is a term that generally refers to a mathematical series—one representing a function that depends upon angles (usually the two angles of a sphere). Since terms are often truncated in equations, only a few are necessary, at first, to be retained for a good approximation to the original function. In general, the expanded functions are very complex. Multipole expansions, for example, are generally used in the calculation of electromagnetic and gravitational fields.

Accordingly, we will introduce the calculation of high-Tc superconductivity by using

multipole expansion.

The vector potential of the Biot-Savart law can be expressed by the following equation:

$$\mathbf{A}(\mathbf{r}) = \frac{\mu}{4\pi}\int_V \frac{\mathbf{J}(\mathbf{r}')}{|\mathbf{r}-\mathbf{r}'|}dv' \tag{5.3.1}$$

Multipole expansion equation of basic solution can be expressed as presented below:

$$\frac{1}{|\mathbf{r}-\mathbf{r}'|} = \sum_{l=0}^{\infty}\sum_{m=-l}^{l}\frac{(l-m)!}{(l+m)!}\frac{r'^l}{r^{l+1}}P_l^m(\cos\theta')P_l^m(\cos\theta)e^{im(\emptyset-\emptyset')} \tag{5.3.2}$$

With respect to the substitution of equation (5.3.2) for (5.3.1), the multipole expansion of the vector potential can be expressed as the following:

$$\begin{aligned}&\mathbf{A}(\mathbf{r})\\ &= \frac{\mu}{4\pi}\sum_{l=0}^{\infty}\sum_{m=0}^{l}\frac{(l-m)!}{(l+m)!}\\ &\times\left(\int_V \mathbf{J}(r',\theta',\emptyset')\frac{r'^l}{r^{l+1}}P_l^m(\cos\theta')P_l^m(\cos\theta)e^{im\emptyset}e^{im\emptyset'}dv'\right)\\ &= \frac{\mu}{4\pi}\sum_{l=0}^{\infty}\sum_{m=0}^{l}\frac{(l-m)!}{(l+m)!}\mathbf{M}_{l,m}\frac{1}{r^{l+1}}P_l^m(\cos\theta)e^{im\emptyset}\end{aligned} \tag{5.3.3}$$

and,

$$\mathbf{M}_{l,m} \equiv \frac{\mu}{4\pi}\int_V \mathbf{J}(r',\theta',\emptyset')r'^l P_l^m(\cos\theta')e^{im\emptyset'}dv' \tag{5.3.4}$$

where, $P_l^m(\cos\theta)$ is associated with the Legendre polynomial, $\mathbf{r} = (r',\theta',\emptyset')$ is the spherical coordinates for the field source of the shielding current, and $\mathbf{J}(\mathbf{r}')$, $\mathbf{r} = (r,\theta,\emptyset)$ is the observation point (Fig. 5.3.6).

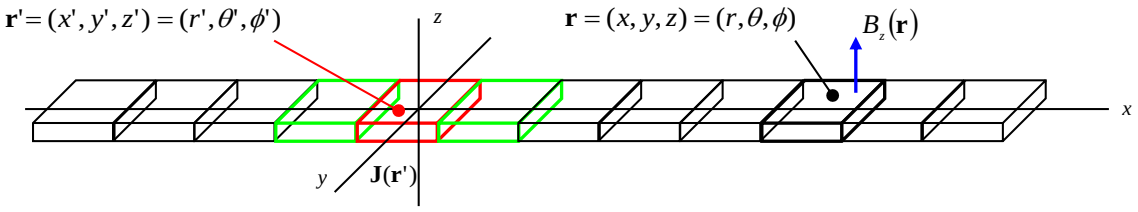

Fig. 5.3.6 Source and observation points in multipole expansion.

Then, the vertical component of the magnetic field B_z can be expressed as follows:

$$\begin{aligned}\mathbf{B}_z(\mathbf{r}) &= \left(\nabla \times \mathbf{A}(\mathbf{r})\right)_z \\ &= \left(\sin\theta\cos\emptyset\frac{\partial}{\partial r} + \frac{\cos\theta\cos\emptyset}{r}\frac{\partial}{\partial\theta} - \frac{\sin\emptyset}{r\sin\theta}\frac{\partial}{\partial\emptyset}\right)A_y \\ &- \left(\sin\theta\sin\emptyset\frac{\partial}{\partial r} + \frac{\cos\theta\sin\emptyset}{r}\frac{\partial}{\partial\theta} - \frac{\cos\emptyset}{r\sin\theta}\frac{\partial}{\partial\emptyset}\right)A_x \\ &= 2\mathrm{Re}\sum_{l=0}^{\infty}\sum_{m=0}^{l}\frac{(l-m)!}{(l+m)!}\frac{e^{im\emptyset}}{r^{l+2}}\Big\{(l \\ &+ 1)\sin\theta P_l^m(\cos\theta)\left(\sin\emptyset M_{xl,m} - \cos\emptyset M_{yl,m}\right) \\ &+ \cos\theta\left(P_l^{m+1}(\cos\theta) - m\frac{\cos\theta}{\sin\theta}P_l^m(\cos\theta)\right)\left(\sin\emptyset M_{xl,m}\right. \\ &\left. - \cos\emptyset M_{yl,m}\right) - im\frac{P_l^m(\cos\theta)}{\sin\theta}\left(\cos\emptyset M_{xl,m} + \sin\emptyset M_{yl,m}\right)\Big\}\end{aligned} \tag{5.3.5}$$

The magnetic field produced by the shielding current closest to the HTS magnet needs to be calculated by Biot-Savart law (equation [5.3.1]) since the accuracy of multipole expansion is not enough under the condition of $r \approx r'$. In addition, it is necessary to calculate the field source's integral volume (equation (5.3.4)), but only one time. Then, $\mathbf{M}_{l,m}$ can be re-used for all observation point $B_z(\mathbf{r})$ under the condition of $r >> r'$.

If we discretize the HTS magnet in $I \times J \times K$ grids, equation (5.3.1) can be calculated by the following:

$$\mathbf{A}_{\mathrm{B}}(\mathbf{r}) = \sum_{i=1}^{I}\sum_{j=1}^{J}\sum_{k=1}^{K}\frac{\mathbf{J}_{i,j,k}}{\left|\mathbf{r} - \mathbf{r}_{i,j,k}\right|}\Delta x\Delta y\Delta z \tag{5.3.6}$$

Then, if the multipole expansion can be truncated at $l = L$, the equation (5.3.3) nearly equals the equation below:

$$\mathbf{A}_{\mathrm{M}}(\mathbf{r}) = \sum_{l=1}^{\infty}\sum_{m=-l}^{l}\frac{(l-m)!}{(l+m)!}\mathbf{M}_{l,m}\frac{1}{r^{l+1}}P_l^m(\cos\theta)e^{im\emptyset} \tag{5.3.7}$$

For typical values of I = 25, J = 35, K = 10, and L = 5, (5.3.6) includes 8,750 summations, and (5.3.7) includes only twenty-five summations. Since the summations are sufficiently reduced, it is evident that the calculation time will be reduced by using the multipole expansion.

For example, Table 5.3.2 shows a comparison of calculation time, based upon Bean's critical state model. The magnetization simulation for a 100 HTS magnets model, by using the multipole expansion, is sufficiently reduced to 10 hours when N_m =3 (50 h by using Biot-Savart law). Accordingly, the multipole expansion can effectively reduce the calculation time, as expected.

Table. 5.3.2 Comparison of calculation time for 20 HTS magnets model

Number of considered HTS magnets, N_m	2	4	6
Biot-Savart law	6h	8h	9h40min
Multipole expansion	2h56min	3h3min	3h7min

For application of this method, we have calculated a large-size model (280 HTS magnets) based on Bean's critical state model. The calculation is approximately 51 hours.

(3) Reduce the Iteration Numbers [18]

As we have mention, the calculation time by using power-law macro-model is about 10 times more than Bean's critical state model. Therefore, it is necessary to reduce the calculation time of the power-law conductivity model.

Fig. 5.3.7 shows the number of iteration at each time step of Bean's critical state model (Total = 137) and the power-law conductivity model (Total = 928).

As a means to speed up the calculation, it is necessary to reduce the power-law conductivity model's number of iteration. We have assumed two kinds of methods to reduce the calculation time.

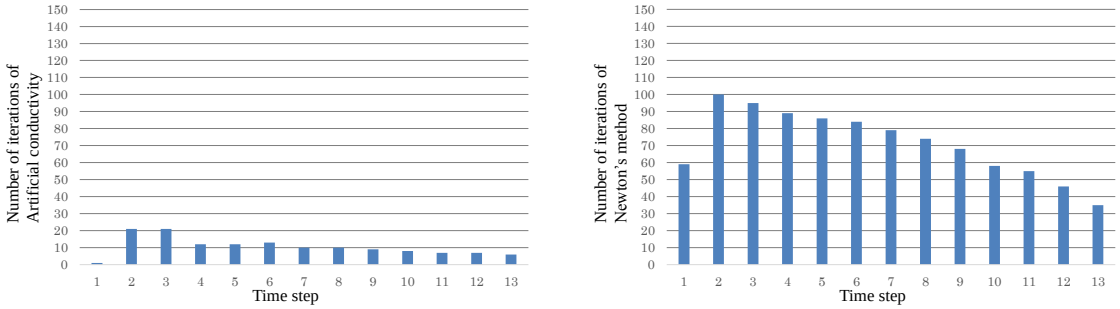

(a) Bean's critical state model (b) Power-law conductivity model

Fig. 5.3.7 Number of iteration in macro-model calculation at each time step.

Acceleration Factor

We have introduced an acceleration factor α in Newton's method of accelerating the calculation. This means adjusting the convergence speed with $\mathbf{T}_{new} = \mathbf{T}_{old}$-$\alpha\,\sigma\mathbf{T}$ instead of $\mathbf{T}_{new} = \mathbf{T}_{old}$-$\sigma\mathbf{T}$ (E in Fig. 5.2.5). However, all of the iterations are diverging when $\alpha>1$, and the convergence speed, is slower when $\alpha<1$. Fig. 5.3.8 shows an example of the number of repetitions for each time step when $\alpha = 0.9$ (Total = 982).

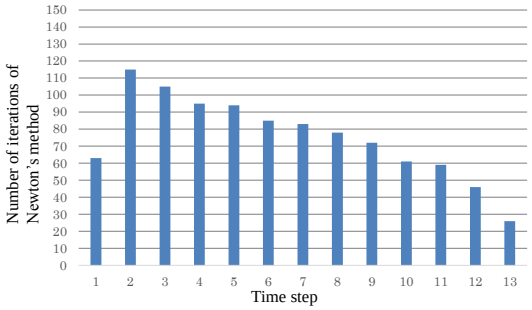

Fig. 5.3.8 Number of iteration at each time step of power-law conductivity model. ($\alpha = 0.9$)

Change Time Step for Reducing the Calculation Time

The current time step is 13 for comparing the simulation result to the experimental measurement. It is expected to reduce the number of iteration by changing the number of time step L. Figs. 5.3.9 (a), (b), and (c) show the number of iteration on Newton's method when the time step L = 10, 26, and 65. When L increases, although the number of iteration decreases in each time step as the changing of the external magnetic field in one time step

decreases, the total number of iterations increases since the total number of time steps increases. When L decreases, it was found that the calculation time will reduce by about 10% when L = 10 as its shortest calculation time.

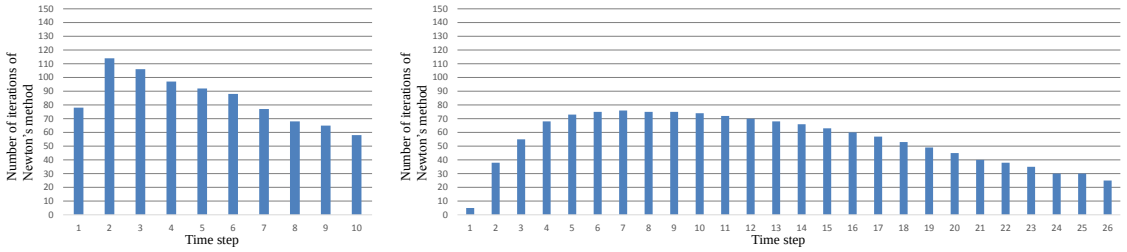

(a) L = 10 (b) L = 26

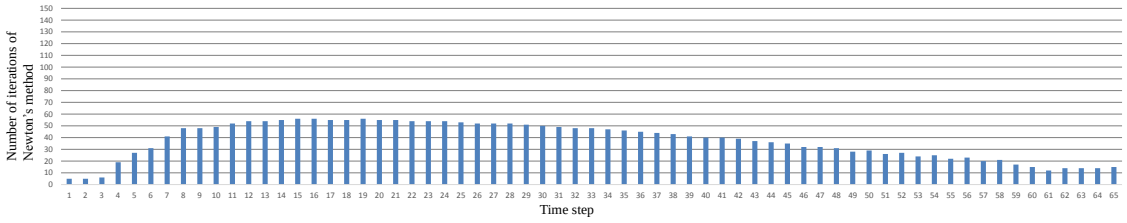

(c) L = 65

Fig. 5.3.9 Number of iteration at each time step of power-law conductivity model.

(4) Change Parameters of Power-law Macro-model in Same Accuracy Range

As a result of our discoveries regarding the agreement between magnetization simulations based upon the power law conductivity model, we have set the parameters as N = 20 and E_C = 1.0e^{-1} [V/m]. Figs. 5.3.10 (a), (b), (c), and (d) show the relative error of the maximum value of 1.0 T, the minimum value of 1.0 T, the maximum value of -0.6 T, and minimum value of -0.6 T by changing the parameter N and E_C. Then, under the same accuracy range as the original value, the shortest calculation time is under the condition of N = 11 and E_C = 1.0e^{-2} [V/m], and the calculation is 1h30min. Essentially, the calculation time has been reduced by approximately 50%.

In summary, we have reduced the calculation time of the power-law macro-model by 50%, an incredibly difficult accomplishment. Furthermore, it is necessary to reduce the

calculation time significantly more, since the calculation time of the power-law macro-model is still five times longer than that of Bean's critical state model.

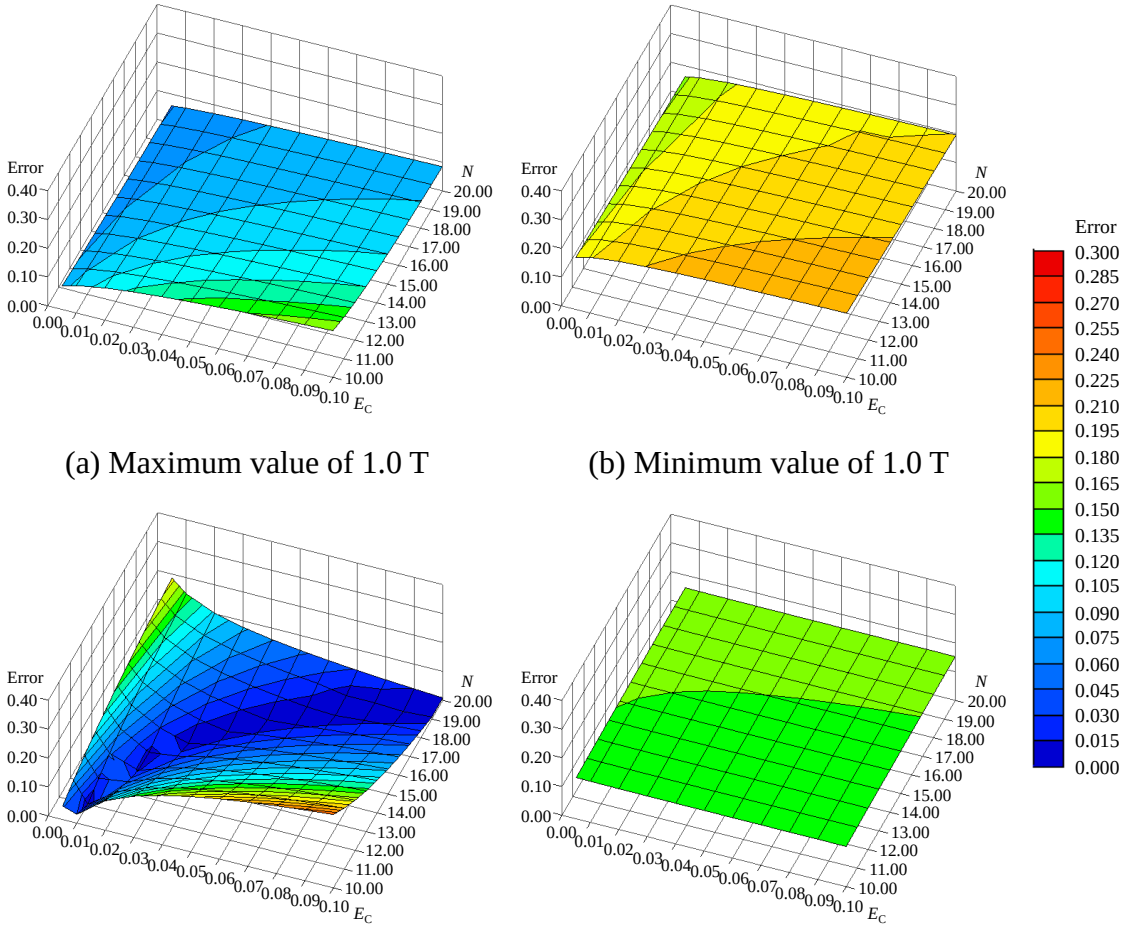

(a) Maximum value of 1.0 T (b) Minimum value of 1.0 T

(c) Maximum value of -0.6 T (d) Minimum value of -0.6 T

Fig. 5.3.10 Relative error by changing parameter N and E_C.

Chapter 6

Applications of the Developed Numerical Code

This Chapter will introduce the applications of the developed numerical code. These applications include the following: the optimization of HTS magnets for uniform magnetic fields, the estimation of electron trajectories, and the calculation of large-scale simulations and SAU.

6.1 Optimization of HTS Magnets for Uniform Magnetic Fields

In general, to maintain an operational laser, it is necessary to achieve a uniform sinusoidal distribution of the vertical magnetic field component (suppressed within 1%) along a longitudinal direction (*x*-direction) of the FEL undulator. However, the sinusoidal distribution of the vertical magnetic field component varies by approximately 16% (Fig. 5.3.4), especially at either end. To eliminate these variations, we have changed the thickness of the 10 HTS magnets in consideration of the developed numerical code (Fig. 6.1.1), as the vertical strength will become weak if the thickness becomes thinner (as the shielding currents reduced). A uniform sinusoidal distribution of the vertical magnetic field component (suppressed within 1%) along a longitudinal direction (*x*-direction) is shown in Fig. 6.1.2.

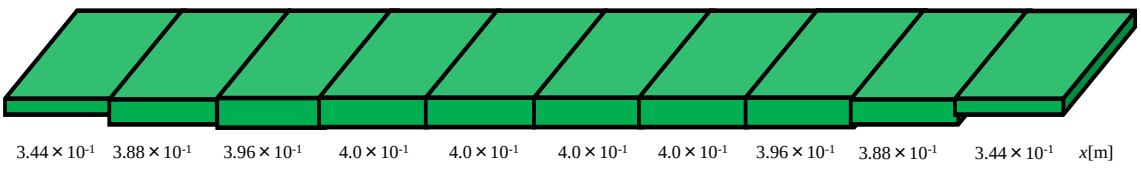

Fig. 6.1.1 Thickness adjustment for eliminating variations.

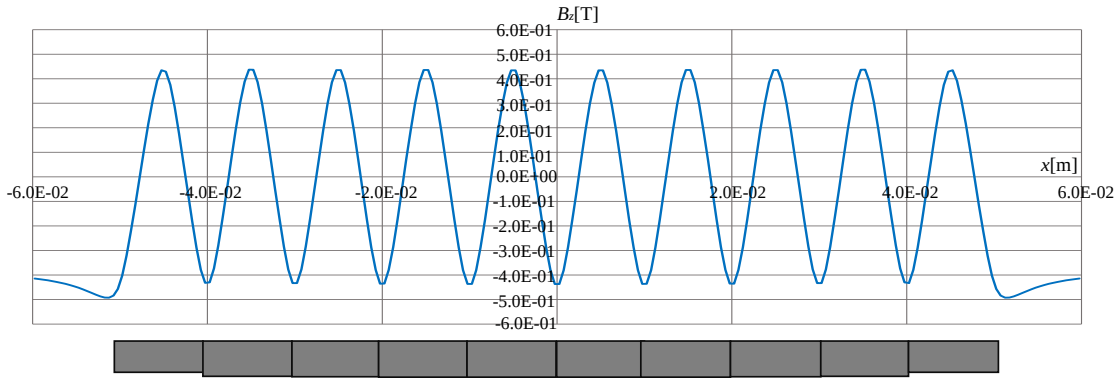

Fig. 6.1.2 Uniform sinusoidal distribution of the vertical magnetic field component by changing thickness of HTS magnets.

6.2 Calculation of an Estimated Electron Trajectory

As we have established, our numerical simulation code not only simulates magnetic fields, but also estimates electron trajectories. Fig. 6.2.1 shows the estimated single electron orbit with 2 GeV energy for laser radiation. This is calculated by the Runge-Kutta method, based on the magnetic field distribution of Fig. 6.1.2. Although the magnetic field is uniform, the electron maintains a curving movement.

The Figures of 6.2.2 indicate the simulation of the magnetic field distribution (Fig. 6.2.2 [a]) and the electron trajectory (Fig. 6.2.2 [b] and [c]) in which an offset vertical magnetic field of -0.41T is additionally applied to that of Fig. 6.1.2. Conclusively, the further modification of the magnetic field of Fig. 6.2.2 (a) gives the reasonable electron trajectory.

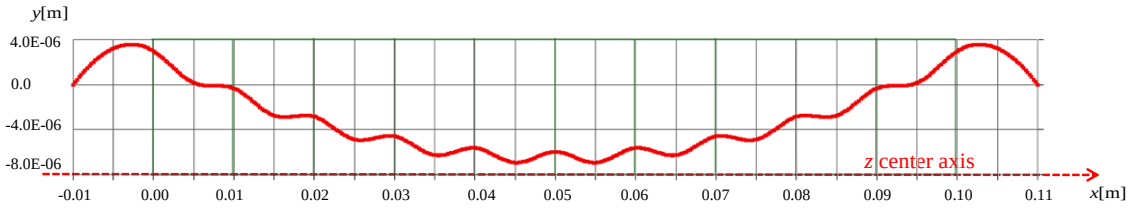

Fig. 6.2.1 Estimated single electron trajectory with 2GeVenergy.

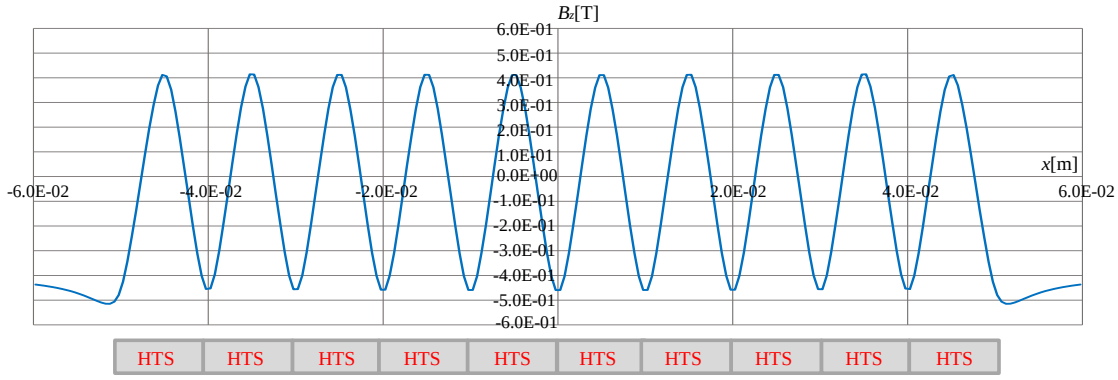

(a) Modified magnetic field component distribution for single electron trajectory

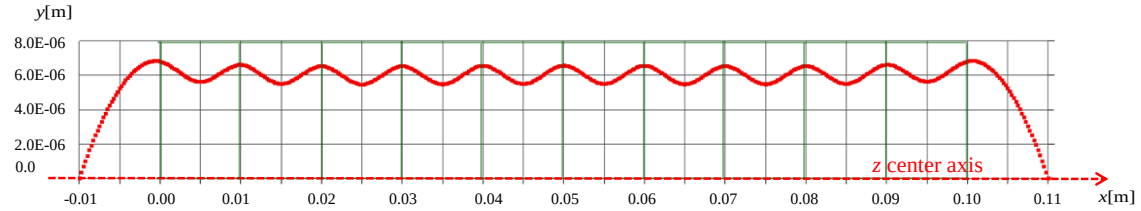

(b) Estimated stable electron trajectory with 2 GeV energy (Top view)

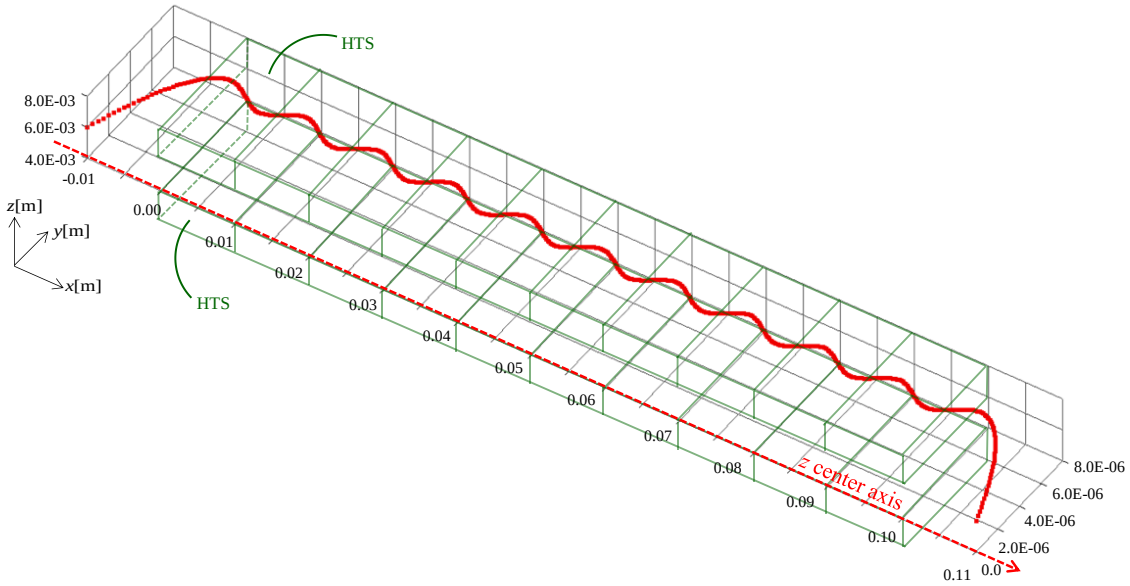

(c) Estimated stable electron trajectory with 2 GeV energy (3D view)

Fig. 6.2.2 Numerical results of HTS magnetization process for stable electron trajectory.

6.3 Calculation of Large-scale Simulation

Additionally, we have applied this method to the creation of large-scale simulations, capturing the effects of 20 HTS magnets, 100 HTS magnets, and 280 HTS magnets, as shown in Fig. 6.3.1 (a), (b) and (c).

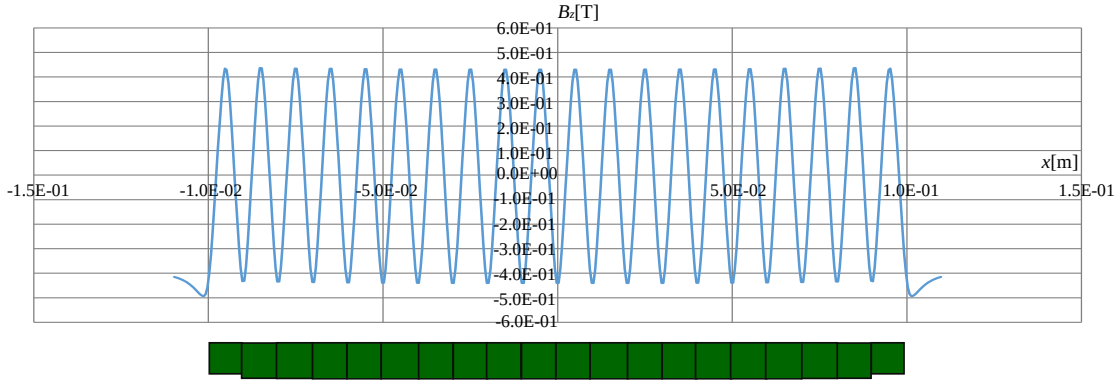

(a) 20 HTS magnets model

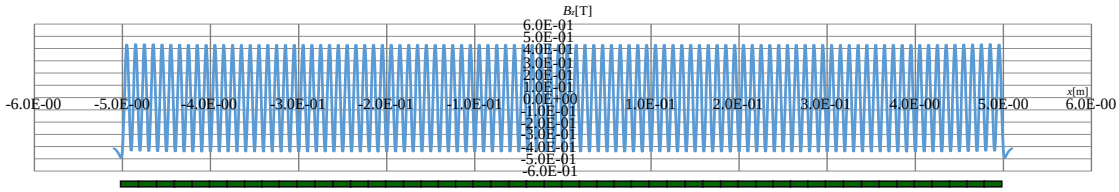

(b) 100 HTS magnets model

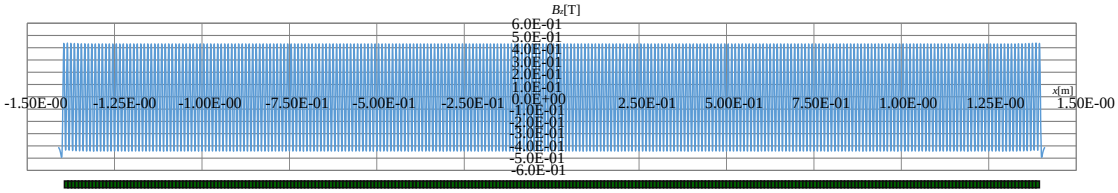

(c) 280 HTS magnets model

Fig. 6.3.1 Uniform sinusoidal distribution of the vertical magnetic field component.

By observing Fig. 6.3.1, it is apparent that the 20 HTS magnets model is a stable means for calculating the pure-type HTS undulator's magnetization process.

6.4 Calculation of SAU

Firstly, Fig. 6.4.1 demonstrates a single unit HTS's numerical model in the *x*-*y* cross section (2.5 mm thickness).

Fig. 6.4.2 shows the distributions of potential T's *z*-component when the initial value of the applied magnetic field is 1 [T], and the magnetic field is reduced at 0.1 [T/sec].

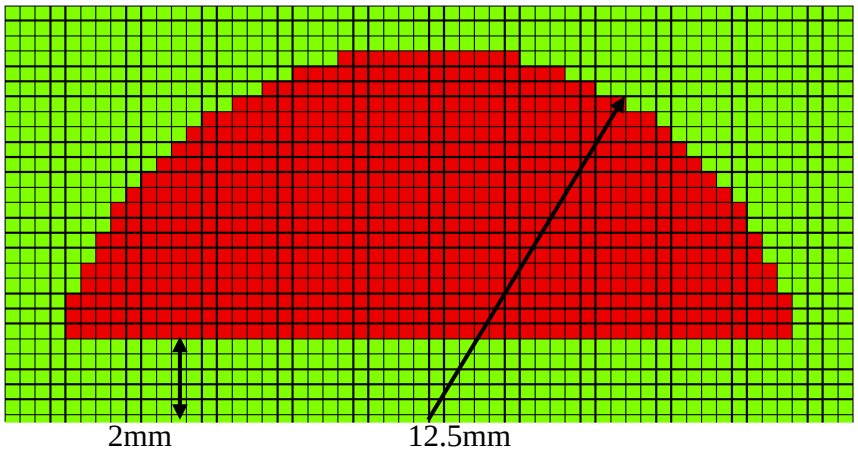

Fig. 6.4.1 Numerical model of a single HTS magnet.

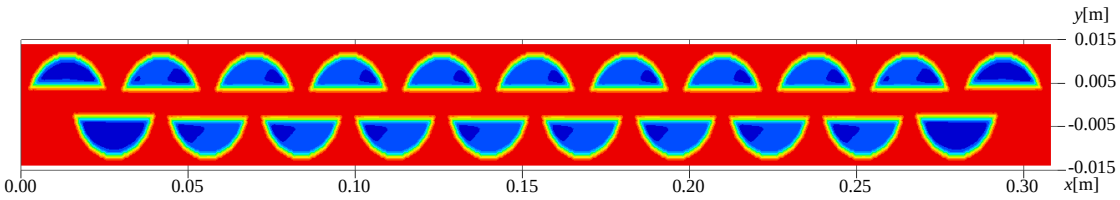

Fig. 6.4.2 Distribution of current potential of SAU.

Fig. 6.4.3 (a) shows the shielding current distributions of the entire SAU, and Fig. 6.4.3 (b) displays an enlarged view of the current distribution flowing in one HTS. In Fig. 6.4.3, there is almost no fluctuation in the *z*-direction. Furthermore, in the shielding current distributions, currents flow almost two-dimensionally to shield the magnetic fields along the edge of the HTSs. Additionally, although the currents seem to flow in the center of the HTSs, they are easily ignored, as they are two digits smaller than the currents along

the edges of the HTSs.

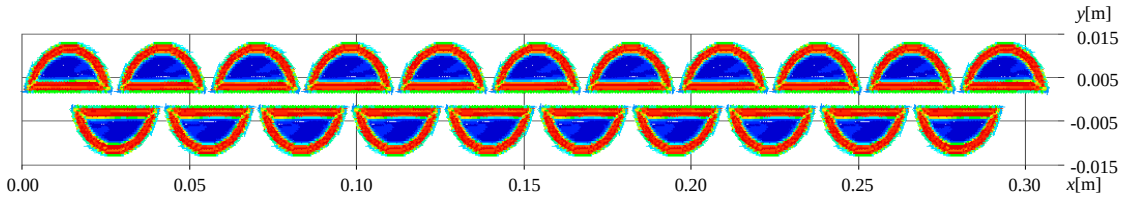

(a) Entire region

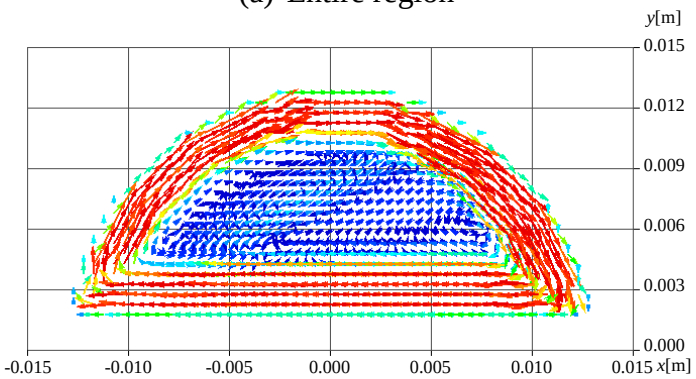

(b) One unit

Fig. 6.4.3 Distribution of shielding current of SAU.

Fig. 6.4.4 shows the magnetic field distribution of the vertical component on the central axis of SAU by considering the interactions between the HTS magnets.

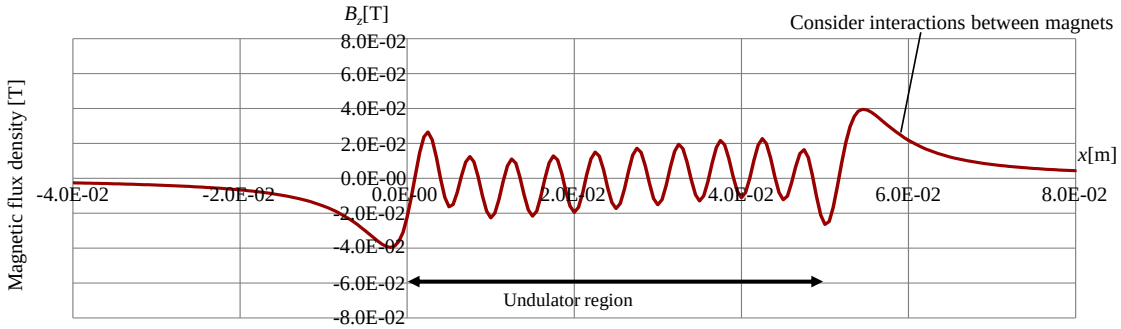

Fig. 6.4.4 Magnetic field distribution in vertical cross-section.

Fig. 6.4.5 shows the comparison of the magnetic field distribution of the central axis's vertical component, considering both the interactions and lack of interactions between the HTS magnets. It was found that the interactions between the HTS magnets cannot be ignored, as they influence the vertical magnetic field of both side edge parts.

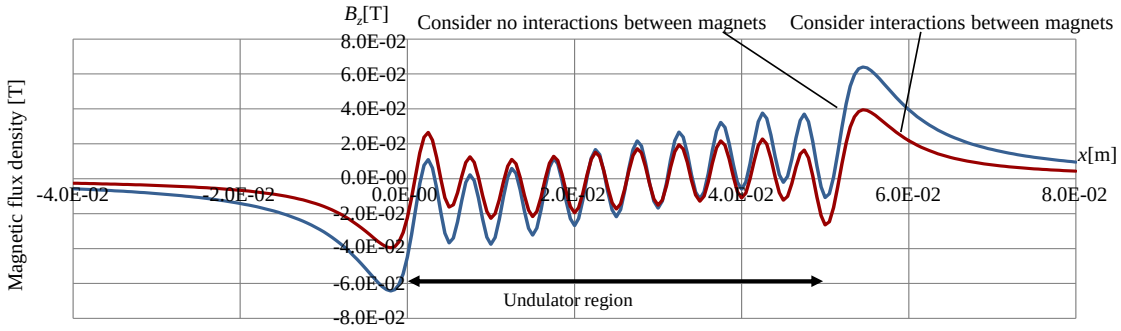

Fig. 6.4.5 Magnetic field distribution in vertical cross-section.

0Fig. 6.4.6 (a) shows the distribution of the vertical component of magnetic field along the electron trajectory for the size of the semi-half circle HTS magnets are all same. It will disturb sinusoidal distribution of the vertical magnetic field component on the electron trajectory. As an application example of the numerical code, we have modified the size and alignment of the HTS magnets by adjusting the vertical aperture size, as

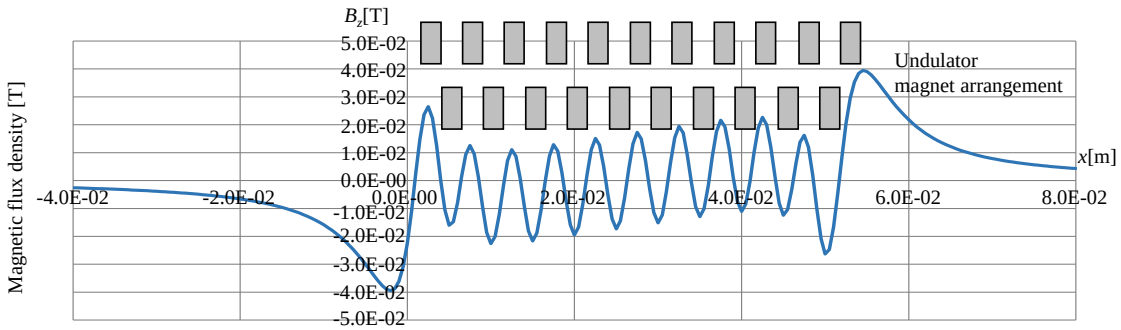

(a) A uniform magnet arrangement

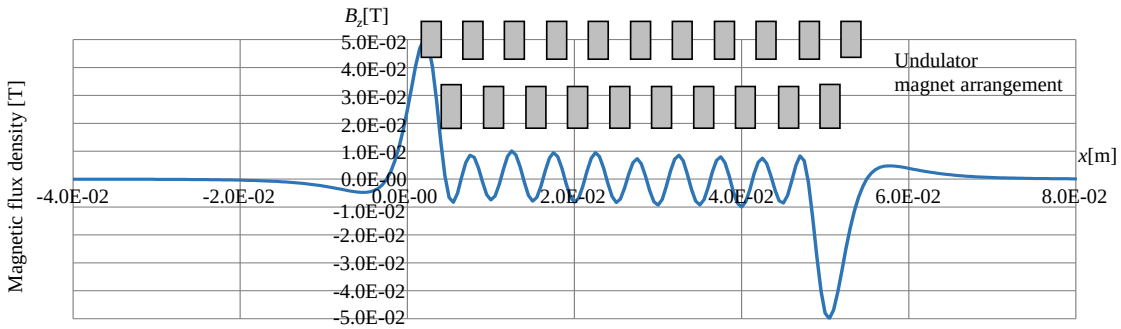

(b) Adjusted HTS magnet arrangement

Fig. 6.4.6 Magnetic field distribution in the vertical direction along the electron trajectory

shown in Fig. 6.4.6 (b) [10]. It is evident that the variation of the sinusoidal distribution improves greatly in Fig. 6.4.6 (b), in exception to both side edge parts.

Figs. (a), (b), and (c) of 6.4.8 show *x*, *y*, and *z*-component distributions of the magnetic field on the *x*-*z* middle plane (Fig. 6.4.7), on which the electron beam travels.

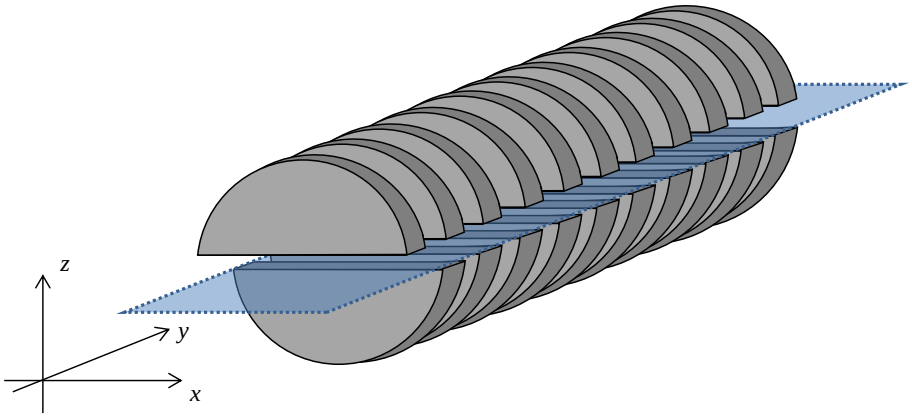

Fig. 6.4.7 Central horizontal *x*-*z* plane of SAU.

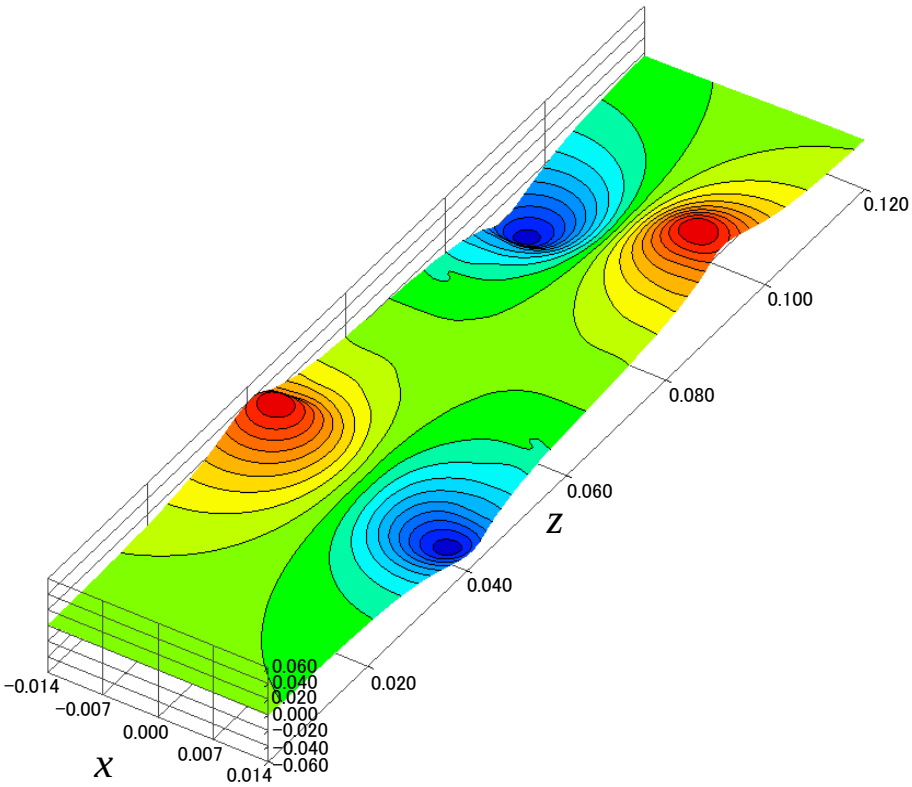

(a) *x*-component

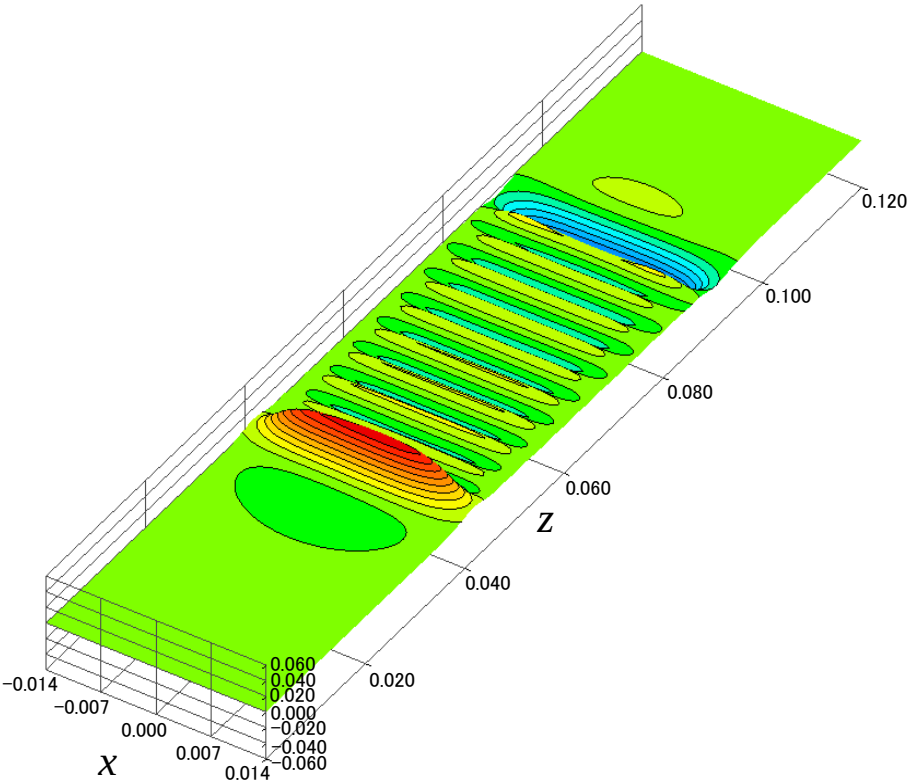

(b) *y*-component

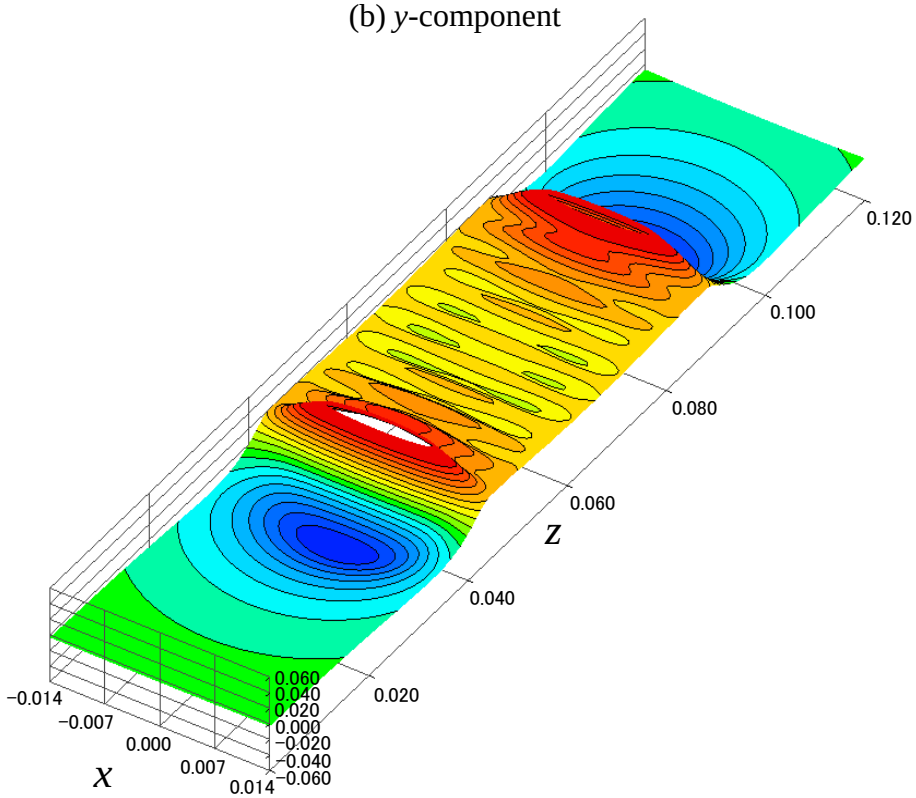

(c) *z*-component

Fig. 6.4.8 Distributions of the magnetic field on x-z middle plane.

The middle vertical cross-section of Fig. 6.4.8 (b) corresponds, exactly, with Fig. 6.4.6 (b). Finally, Fig. 6.4.9 shows a predicted electron trajectory (with 100 MeV energy) in the magnetic field (Fig. 6.4.8) of the SAU.

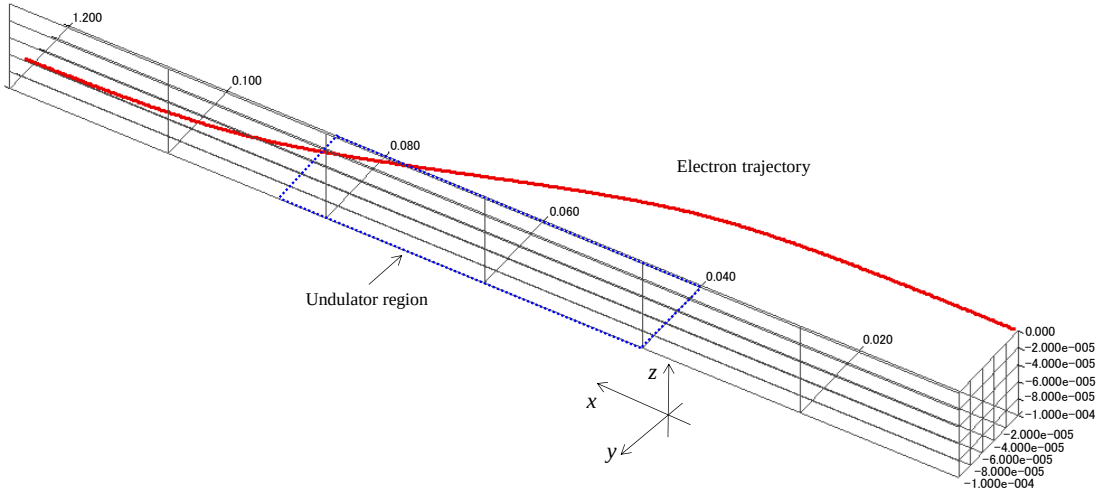

Fig. 6.4.9 Estimated single electron trajectory in SAU.

We also compared the strength of the magnetic fields of SAU and pure-type HTS undulators.

Fig. 6.4.10 shows the distribution of the vertical magnetic field component for both SAU (a) and pure-type HTS undulators (b). The strength of the magnetic field of the pure-type HTS undulator (based on Bean's critical state model) is approximately forty times more powerful than that of the SAU, as we expected.

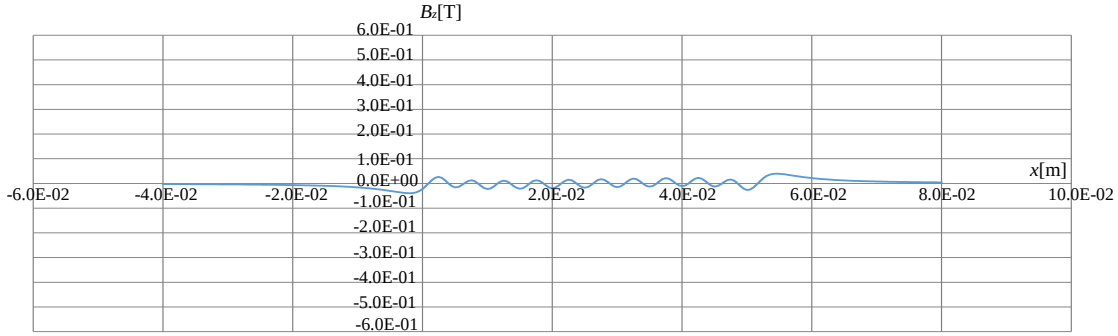

(a) SAU

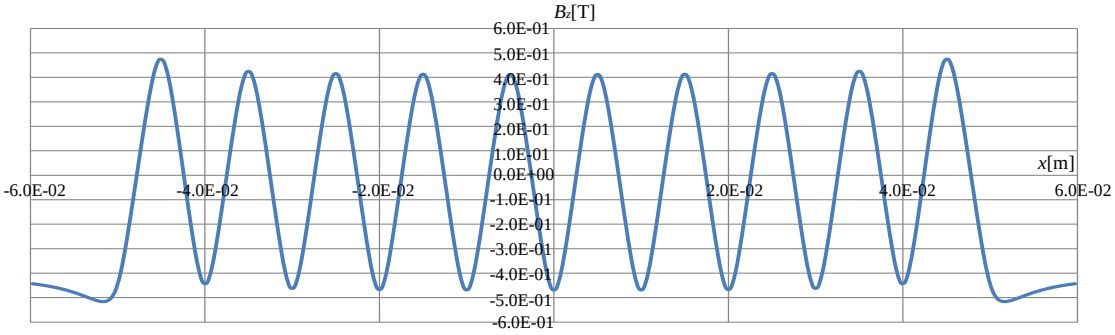

(b) pure-type HTS undulator (10 HTS magnets)

Fig. 6.4.10 Comparison of distribution of vertical magnetic field component.

Chapter 7

Conclusions

We have discussed the high-Tc superconductor undulator for free-electron lasers, presenting the numerical analysis of its magnetization process, based upon the T-method. In summary, we have accomplished the following things:

(1) We developed a numerical simulation code for the magnetization process of HTS magnets, based upon the T-method and power-law conductivity method. We confirmed that this method can effectively simulate the magnetization process by using the same shielding current value as the experimental measurement.

(2) We have developed an improved simulation scheme of the magnetization process in the pure-type HTS undulator for very large numerical models for the size of the real machine. To carefully evaluate the calculation of the interactions between HTSs, it was observed that the number of HTSs considered for the interactions could be truncated at a few HTSs within acceptable relative error. Additionally, we efficiently sped-up the simulation time by using the method of the multipole expansion of the Biot-Savart law. In essence, our developed numerical simulation code can sufficiently reduce the calculation time.

(3) We have also discussed how to reduce the calculation time when simulating the magnetization process of HTS magnets based on the power law conductivity method. The calculation time can be reduced 10% by decreasing the time step, and 50% by changing the parameters N and E_C. We confirmed that it is very difficult to reduce the calculation

time when simulating the magnetization process of HTS magnets based on power law conductivity method.

(4) Applications of this developed numerical simulation code,

We have designed the HTS magnets alignment for the Pure-type HTS undulator by using the T-method. Furthermore, we have confirmed the possibility of achieving a uniform sinusoidal distribution of the vertical magnetic field component (suppressed within 1%) along a longitudinal direction (*x*-direction) of the FEL undulator for maintaining laser operation by using this developed numerical simulation code.

We have estimated a stable single electron orbit with 2 GeV energy by changing the offset vertical magnetic field for laser radiation. This is calculated by the Runge-Kutta method based on the magnetic field distribution. We confirmed that even if the magnetic field is uniform, the electron may move in a curved direction.

Lastly, we have applied this numerical simulation code for assisting the design of the HTS magnets alignment in the SAU as a means to employ the HTS magnetization process based on the T-method with the Bean's critical state model. The developed numerical code provided the shielding current distribution and the corresponding magnetic field distribution. In addition, the single estimated electron motion was predicted by using the SAU's magnetic field. We also compared the strength of the magnetic fields between the pure-type HTS undulator and SAU. We confirmed that the magnetic field of the pure-type HTS undulator is about 10 times stronger than that of the SAU

Ultimately, it is evident that the sinusoidal vertical magnetic field component distribution can be improved by adjusting the size of HTS magnets at the design stage.

Chapter 8

Future Work

As the future work of this research, it is mainly divided into two parts:

(1) For further reducing the relative error (such as Fig. 5.2.20), it is necessary to try some other methods (A-method or A-φ method) and some other macro-model (Kim's model or exponential critical-state model) to sufficiently simulate the magnetization process with the experimental measurement.

(2) Even if the calculation-time of the magnetization process, based upon the power law method, has been reduced by about 50%, it is still five times longer than using the Bean's critical state model. In the future, it is necessary to shorten the calculation time by improving the solution of nonlinear equations, such as the Chebyshev method and so on.

References

[1] T. Kii and R. Kinjo, “Application of bulk high-temperature superconduc tor to insertion device for synchrotron radiation,” *Teion Kogaku*, vol. 46, pp. 118-124, 2011.

[2] T. Tanaka, R. Tsuru and H. Kitamura, “Pure-type superconductor permanent magnet undulator,” *J. Synchrotron Radiat.*, vol. 12, pp. 442-447, 2005.

[3] T. Tanaka, T. Hara, H. Kitamura, R. Tsuru, T. Bizen, X. Mare´chal, T. Seike, “Application of high-temperature superconducting permanent magnets to synchrotron radiation sources,” *Phys. Rev. ST Accel. Beams*, vol. 7, 2004, Art. ID 090704.

[4] SACLA(XFEL) homepage, http://xfel.riken.jp/index.html

[5] Y. Otake, “Overview of SACLA machine status,” in *Proc. LINAC, 2012*, pp. 427-431.

[6] T. Sugiura, H. Hashizume and K. Miya, “Numerical electromagnetic field analysis of type-II superconductors,” *Int. J. Appl. Electromagn. Mater.*, vol. 2, pp. 183-196, 1991.

[7] M. Tsuchimoto and H. Takashima: “Two-dimensional stress distributions in disk and ring high-Tc superconductors,” *Jpn. J. Appl. Phys.*, vol. 39, pp. 5816-5821, 2000.

[8] M. Tsuchimoto, K. Demachi, I. Itoh, “Numerical evaluation of uniform magnetic field within superconducting swiss roll,” *Phys. C, Supercond. Appl.*, vol. 412-414, pp. 719-722, 2004.

[9] M. Tsuchimoto, “Numerical evaluation of field profile in an undulator with bulk HTS,” *Phys. Procedia*, vol. 27, pp. 452-455, 2012.

[10] Yi Deri, F. Tanaka, H. Kawaguchi, M. Tsuchimoto, “Design of HTSC undulator magnet array based on simulation of magnetization process,” *J. Adv. Simul. Sci. Eng.*, vol. 2, pp. 34-43, 2015.

[11] A. Kamitani, T.Takayama, S. Ikuno, “Numerical Simulation of Inductive Method and Permanent-Magnet Method for Measuring Critical Current Density”, *IEEE Trans. Magn.*, vol. 44, no. 6, 2008.

[12] R. Fresa, G. Rubinacci, S. Ventre, F. Villone, W. Zamboni, “Fast Solution of a 3-D Integral Model for the Analysis of ITER Superconducting Coils”, *IEEE Trans. Magn.*, vol. 45, no. 3, 2009.

[13] G. P. Lousberg, J. F. Fagnard, M. Ausloos, P. Vanderbemden, B. Vanderheyden, “Numerical Study of the Shielding Properties of Macroscopic Hybrid Ferromagnetic/Superconductor Hollow Cylinders”, *IEEE Trans. Appl. Supercond.*, vol. 20, no. 1, 2010

[14] A. Kamitani, T.Takayama, S. Ikuno, “High-Speed Method for Analyzing Shielding Current Density in High-Temperature Superconductor”, *IEEE Trans. Magn.*, vol. 47, no. 5, 2011.

[15] Yi Deri, H. Kawaguchi, M. Tsuchimoto, T. Tanaka, “Simulation of magnetization process of pure-type superconductor magnet undulator based on T-method,” *Phys. C, Supercond. Appl.*, vol. 518, pp. 106-110, 2015.

[16] H. Kawaguchi, Yi Deri, “Numerical Analysis of Magnetization Process of High-Tc Superconductor Undulator of X-ray FEL Using Power Law Conductivity”, in *Porc. ISEM*, 2017, pp. P-TRA-14.

[17] Yi Deri, H. Kawaguchi, “Large Scale Simulation of Magnetization Process of HTS Undulator for X-ray FEL Based on T-method”, *IEEE Trans. Magn.*, vol. 54, no. 3, 2018, Art no: 7202104.

[18] Yi Deri, H. Kawaguchi, “Improvement for Speed-up of Numerical Analysis of HTS Magnetization Process of FEL Undulator”, *IEICE Technical Report*, EMT-17-149, pp. 253-258, 2017.

[19] F. R. Elder, A. M. Gurewitsch, R. V. Langmuir, and H. C. Pollock, “Radiation from Electrons in a Synchrotron”, *Phys. Rev.*, vol. 71, no 11, pp. 829-830, 1947.

[20] M. Watanabe, S. Sato, I. Munro, G. S. Lodha, A guide to synchrotron radiation science, Narosa, 2016.

[21] J.J.Thomson, “Cathode rays”, *Philos. Mag.*, vol. 44, no. 269, pp. 293-316, 1897.

[22] J. P. Blewett, “Radiation Losses in the Induction Electron Accelerator”, *Phys. Rev.*, vol. 69, no. 3-4, pp. 87-95, 1946.

[23] J. P. Blewett, “Synchrotron radiation – early history”, *J. Synchrotron Radiat.*, vol. 5, pp. 135-139, 1998.

[24] E. M. Rowe, R. A. Otte. C. H. Pruett, J. D. Steben, “Operation and Performance of the University of Wisconsin - Physical Sciences Laboratory Electron Storage Ring”, *IEEE Trans. Nucl. Sci.*, vol. 16, no. 3, pp. 159-164, 1969.

[25] T. Miyahara, *et al.* “SOR-RING: An Electron Storage Ring Dedicated to Spectroscopy”, *Particle accelerators*, vol. 7, pp. 163-175, 1976.

[26] T. Sasaki, “A Prospect and Retrospect at the 50th Anniversary of Synchrotron Radiatio”, *J. Jpn. Soc. Synchrotron Radiat. Res.*, vol. 11, no. 2, pp. 82-92, 1998.

[27] Y. Kimura, N. Toge, “Pursuit of Accelerator Projects at KEK in Japan”, *Rev. Accl. Sci. Tech.*, vol. 05, pp. 333-360, 2012.

[28] ALS homepage, https://science.energy.gov/bes/suf/user-facilities/x-ray-light-sources/als/

[29] ESRF homepage, http://www.esrf.eu/

[30] APS homepage, https://www1.aps.anl.gov/

[31] SPring-8 homepage, http://www.spring8.or.jp/ja/

[32] H. Motz, “Applications of the Radiation from Fast Electron Beams”, *J. Appl. Phys.*, vol. 22, no. 5, pp. 527-535, 1951.

[33] H. Motz, W. Thon, R. N. Whitehurst, “Experiments on Radiation by Fast Electron Beams”, *J. Appl. Phys.*, vol. 24, no. 7, pp. 826-833, 1953.

[34] R.M.Phillips, “History of the ubitron”, *Nucl. Instrum. Mrth. A*, vol. 272, pp. 1-9, 1988.

[35] D. A. G. Deacon, L. R. Elias, J. M. J. Madey, G. J. Ramian, H. A. Schwettman, and T. I. Smith, “First Operation of a Free-Electron Laser”, *Phys. Rev. Lett.*, vol. 38, pp. 892-894, 1977.

[36] T. Tomimasu, “Development of five compact storage rings, TERAS and NIJI-I–IV, at ETL”, *Nucl. Iustrum. Meth. A*, vol. 308, no. 1-2, pp. 6-12, 1991.

[37] Z. Huang, K. Kim, “Review of x-ray free-electron laser theory”, *Phys. Rev. ST Accel. Beams*, vol. 10, 2007, Art. ID 034801.

[38] J. Rubensson, “Synchrotron Radiation: An everyday application of special relativity”, IOP Concise Physics, Cap. 1, pp. 1-6, 2016.

[39] Electron Microanalysis Core Facility homepage, https://nau.edu/cefns/labs/electron-microprobe/glg-510-class-notes/instrumentation/

[40] S. Humphries, Jr., “Principles of Charged Particle Acceleration”. Wiley, 1986.

[41] H. Kamitsubo, T. Ota, *Synchrotron radiation*, Tokyo: Iwanami Shoten, 2005. (in Japanese)

[42] K. Minami et al., *Free Electron laser and its application*, Tokyo: Corona Publishing, 1990. (in Japanese)

[43] W. Meissner, R. Ochsenfeld, “Ein neuer Effekt bei Eintritt der Supraleitfähigkeit”, *Die Naturwissenschaften*, vol. 21, no. 44, pp. 787-788, 1933.

[44] F. London, H. London, “The electromagnetic equations of the supraconductor”, *Proc. Math. Phys. Eng. Sci.*, vol. 149, no. 866, pp. 71-88, 1935.

[45] J. Bardeen, L. N. Cooper, J. R. Schrieffer, “Microscopic Theory of

Superconductivity", *Phys. Rev.*, vol. 106, pp. 162-164, 1957.

[46] J. Bardeen, L. N. Cooper, J. R. Schrieffer, "Theory of Superconductivity", *Phys. Rev.*, vol. 108, pp. 1175-1205, 1957.

[47] B. D. Josephson, "Possible new effects in superconductive tunnelling", *Phys. Lett.*, vol. 1, no. 7, 1962.

[48] J. G. Bednorz, K. A. Müller, "Possible high T_c superconductivity in the Ba-La-Cu-O system", *Z. Phys. B*, vol. 64, no. 2, 1986.

[49] M. K. Wu, J. R. Ashburn, C. J. Torng, P. H. Hor, R. L. Meng, L. Gao, Z.J. Huang, Y. Q. Wang, and C. W. Chu, "Superconductivity at 93 K in a new mixed-phase Y-Ba-Cu-O compound system at ambient pressure", *Phys. Rev. Lett.*, vol. 58, no. 9, pp. 908-910, 1987.

[50] A. Schilling, M. Cantoni, J. D. Guo, H. R. Ott, "Superconductivity above 130K in the Hg-Ba-Ca-Cu-O system", *Nature*, vol. 363, pp. 56-58, 1993.

[51] P. Dai, B. C. Chakoumakos, G. F. Sun, K. W. Wong, Y. Xin, D. F. Lu, "Synthesis and neutron powder diffraction study of the superconductor $HgBa_2Ca_2Cu_3O_{8+delta}$ by Tl substitution", *Phys. C, Supercond. Appl.*, vol. 243, no. 3-4, pp. 201-206, 1995.

[52] A. P. Drozdov, M. I. Eremets, I. A. Troyan, V. Ksenofontov, S. I. Shylin, "Conventional superconductivity at 203 kelvin at high pressures in the sulfur hydride system", *Nature*, vol. 525, pp. 73-76, 2015.

[53] B. S. Deaver, Jr, W. M. Fairbank, "Experimental Evidence for Quantized Flux in Superconducting Cylinders", *Phys. Rev. Lett.*, vol. 7, no. 2, pp. 43-46, 1961.

[54] K. Osamura, Superconductivity materials, Yoneda publication, Chapter 2.9, pp. 50-86, 2000. (in Japanese)

[55] C. P. Bean, “Magnetization of Hard Superconductors”, *Phys. Rev. Lett.*, vol. 8, no. 6, pp. 250-253, 1962.

[56] C. P. Bean, “Magnetization of High-Field Superconductors”, *Rev. Mod. Phys.*, vol. 36, no. 1, pp. 31-39, 1964.

Acknowledgements

This paper summarizes the research results of the author, while studying in the Microwave Engineering Laboratory, Muroran Institute of Technology, during the master and doctoral courses from Apr. 2013 to Mar. 2018.

I would like to express my gratitude to all the people who helped me during the writing of my doctoral dissertation.

My deepest gratitude goes, first and foremost, to Professor Hideki Kawaguchi, my supervisor, for his constant encouragement and guidance. Thank you for giving me the opportunity to study in Muroran Institute of Technology and research these very interesting studies. He has walked me through all the stages of this thesis. Without his consistent and illuminating instruction, this thesis could not have reached its present form.

I also would like to express my heartfelt gratitude to the vice supervisors, Professor Kohki Satoh and Professor Kota Watanabe, who have provided me with important opinions with respect to revising and improving my dissertation.

Thanks to Professor Masanori Tsuchimoto for giving us special research ideas, and may he rest in peace.

In addition, I owe my sincere gratitude to the students in our laboratory, Mr. Shibata, Mr. Tanaka, Mr. Itasaka, Mr. Tomita, Mr. Takahashi, Mr. Nishimura, Mr. Moritani, and everyone who has helped me tremendously through my life and studies.

Special thanks go to Rotary Yoneyama Memorial Foundation and my dear Japanese friends, especially Mrs. Shiozaki, Mr. Ihara, Mrs. Mitsuya, and Mr. Hiei and everyone else for their help.

Finally, I would like to thank to my parents, who lead the way through life.

List of Publications

Peer-reviewed Papers

[1] Yi Deri, Hideki Kawaguchi, "Large Scale Simulation of Magnetization Process of HTS Undulator for X-ray FEL Based on T-method", *IEEE Transactions on Magnetics*, vol. 54, no. 3, 2018, Art no: 7202104.

[2] Yi Deri, Hideki Kawaguchi, Masanori Tsuchimoto, Takashi Tanaka, "Simulation of Magnetization Process of Pure-type Superconductor Magnet Undulator Based on T-method", *Physica C: Superconductivity and its Applications*, vol. 518, pp. 106-110, 2015.

[3] Yi Deri, Fumiya Tanaka, Hideki Kawaguchi, Masanori Tsuchimoto, "Design of HTSC Undulator Magnet Array Based on Simulation of Magnetization Process", *Journal of Advanced Simulation in Science and Engineering*, vol. 2, pp. 34-43, 2015.

International Conference Proceedings

[1] Hideki Kawaguchi, Yi Deri, "Numerical Analysis of Magnetization Process of High-Tc Superconductor Undulator of X-ray FEL Using Power Law Conductivity", 18th International Symposium on Applied Electromagnetics and Mechanics (ISEM2017), P-TRA-14 (2 pages), Chamonix – Mont-Blanc, France, Step. 2017.

[2] Yi Deri, Hideki Kawaguchi, "Large Scale Simulation of Magnetization Process of HTS Undulator for X-ray FEL Based on T-method", 21th International Conference on the Computation of Electromagnetic Fields (Compumag2017), PA-M1-7 (2 pages), Daejeon, Korea, Jun. 2017.

[3] Yi Deri, Hideki Kawaguchi, Masanori Tsuchimoto, "Magnet Alignment Design of

Pure-type Superconductor Undulator by Using Magnetization Simulation Based on T-method", 2015 International Symposium on Nonlinear Theory and its Applications (NOLTA2015), pp. 816-819, Hong Kong, Dec. 2015.

[4] Yi Deri, Hideki Kawaguchi, Masanori Tsuchimoto, Takashi Tanaka, "Simulation of Magnetization Process of Pure-type Superconductor Magnet Undulator Based on T-method", 27th International Symposium on Superconductivity (ISS2014), SA-26, Funabori, Tokyo, Nov. 2014.

Conference Proceedings

[1] Yi Deri, H. Kawaguchi, "Improvement for Speed-up of Numerical Analysis of HTS Magnetization Process of FEL Undulator", *IEICE Technical Report*, EMT-17-149, pp. 253-258, 2017.

[2] 依 徳日, 川口 秀樹, "べき乗則マクロモデルを用いた Pure-type HTS アンジュレータの着磁プロセスの数値解析", 平成 29 年度電気・情報関係学会北海道支部連合大会講演論文集, 函館, No.6, Oct. 2017.

[3] Yi Deri, D. Tomita, H. Kawaguchi, "Simulation of Magnetization Process of Pure-type Superconductor Magnet Undulator Based on Field Dependence of Critical Current", in *Proc. MAGDA2016*, pp. 289-292, Nov. 2016.

[4] 依 徳日, 川口 秀樹, "自由電子レーザの小型化に向けた高温超伝導体のシミュレーションと形状設計", 第 1 回室蘭工業大学大学院博士後期課程学生研究発表会(ドクコン 2016), 東京, Nov. 2016.

[5] 依 徳日, 川口 秀樹, "着磁プロセス数値シミュレーションを用いた Pure-type アンジュレータの磁石配置設計", 平成 28 年度電気・情報関係学会北海道支部連合大会講演論文集, 札幌, No.18, Nov. 2016.

[6] 依 徳日, 川口 秀樹, 槌本 昌則, “Pure-type”アンジュレータ超伝導磁石の着磁プロセス解析を用いた磁場設計”, 平成 27 年第 20 回超伝導・低温若手セミナー研究会, 札幌, Sep. 2015.

[7] 依 徳日, 川口 秀樹, 槌本 昌則, “小型 FEL のための”Pure-type”アンジュレータ超伝導磁石の着磁プロセスの数値解析”, 平成 26 年度電気・情報関係学会北海道支部連合大会講演論文集, 札幌, No.14, Oct. 2014.

[8] 依 徳日, 田中 郁也, 川口 秀樹, 槌本 昌則, “超伝導磁石間の相互作用を考慮した高温超伝導体 FEL アンジュレータの着磁解析”, 平成 25 年度電気・情報関係学会北海道支部連合大会講演論文集, 室蘭, No.21, Oct. 2013.

Rewards

Rotary Yoneyama Memorial Doctoral Course Scholarship (YD), Apr. 2017.